The Effective Vector Boson Approximation in High-Energy Muon Collisions

Richard Ruiz,[a] **Antonio Costantini,**[b] **Fabio Maltoni, and**[b,c] **Olivier Mattelaer**[b]

[c]*Institute of Nuclear Physics – Polish Academy of Sciences* (IFJ PAN),
ul. Radzikowskiego, Kraków 31-342, Poland

[b]*Centre for Cosmology, Particle Physics and Phenomenology* (CP3),
Université Catholique de Louvain, Chemin du Cyclotron, B-1348 Louvain la Neuve, Belgium

[c]*Dipartimento di Fisica e Astronomia, Università di Bologna e INFN,*
Sezione di Bologna, via Irnerio 46, I-40126 Bologna, Italy

E-mail: antonio.costantini@uclouvain.be, fabio.maltoni@uclouvain.be,
olivier.mattelaer@uclouvain.be, rruiz@ifj.edu.pl

ABSTRACT: Due to the inclination for forward gauge radiation, lepton colliders beyond a few TeV are effectively electroweak (EW) boson colliders, suggesting the treatment of EW bosons as constituents of high-energy leptons. In the context of a muon collider, we revisit the validity of W and Z parton distribution functions (PDFs) at leading order in $2 \to n$ process. We systematically investigate universal and quasi-universal power-law and logarithmic corrections that arise when deriving (polarized) weak boson PDFs in the collinear limit. We go on to survey a multitude of $2 \to n$ processes at $\sqrt{s} = 2 - 30$ TeV via polarized and unpolarized EW boson fusion/scattering. To conduct this study, we report a public implementation of the Effective W/Z and Weizsäcker-Williams Approximations, which we collectively call the Effective Vector Boson Approximation, into the Monte Carlo event generator `MadGraph5_aMC@NLO`. This implementation lays the groundwork for developing matrix-element matching prescriptions involving EW parton showers and renormalized EW PDFs. To further with this agenda, we give recommendations on using W/Z PDFs.

KEYWORDS: Effective W Approximation, Electroweak Boson PDFs, Muon Colliders, Helicity Polarization, Monte Carlo Tools

Contents

1 Introduction

Within the Standard Model (SM) of particle physics, the existence of gauge bosons with nonzero masses is one of the defining characteristics that distinguishes the electroweak (EW) sector from perturbative quantum chromodynamics (pQCD). However, at momentum transfers scales (Q) far above the EW breaking scale, $v = \sqrt{2}\langle\Phi\rangle \approx 246$ GeV, weak bosons are effectively massless, thereby softening this distinction. More precisely, at $Q^2 \gg M_V^2$, where $M_V = M_W$, M_Z are the W and Z boson masses, process-dependent, power-law terms that scale as $\delta\sigma \sim (M_V^{2k}/Q^{2k+2})$, with $k > 1$, become negligible in $2 \to n$ scattering processes and analogously $1 \to n'$ decay processes. Consequentially, at sufficiently energetic collider experiments, collinear, t-channel emissions of weak bosons from initial-state partons, as shown schematically in Fig. 1, can be factorized into a type of weak boson parton distribution function* (PDF), and be modeled as *almost massless*, on-shell, initial-state constituents of high-energy lepton and hadron beams [5–7].

Known as the Effective W/Z Approximation (EWA) [5, 6], the partitioning of collinear, initial-state W/Z boson emissions out of matrix elements (MEs) and into PDFs has several benefits. Like heavy quark factorization [8–15] and the factorization of inelastic photons, i.e., the Weizsäcker-Williams Approximation [16, 17], the EWA significantly simplifies ME computations and phase space integration, particularly in the infrared limits of phase space. Even in the absence of singularities, such factorization may be necessary to avoid numerical instabilities in real calculations when scale hierarchies are present, e.g., to avoid a large collinear logarithm when $Q^2 \gg M_V^2$. Since its inception, the approximation has been used to model numerous scenarios, including weak vector boson fusion/scattering (VBF) [18–21], heavy quark production from Wg-scattering [22, 23], and heavy lepton production [23].

The EWA, however, also comes at a cost. Like other instances of collinear factorization, invoking the EWA means losing knowledge about: (i) the recoil kinematics/transverse momentum (p_T) of partons associated with the emission of initial-state weak bosons, and which scale as $\mathcal{O}(M_V^2/Q^2)$ and as $\mathcal{O}(p_T^2/Q^2)$; (ii) the interference between initial-state weak boson polarizations, which scale as $\mathcal{O}(M_V^2/Q^2)$ [5]; and (iii) the interference between different EW mass eigenstates, i.e., γ_T/Z_T mixing, which can have large, $\mathcal{O}(1)$ effects [1, 4, 24, 25]. However, in principle, extending highly successful matching and merging techniques pioneered for QCD and QED [26–29] offer a starting path to resolve some of these drawbacks.

Notably, momentum transfers needed to neglect power corrections of the form $(p_T^2/Q^2)^k$ and $(M_V^2/Q^2)^k$, where $k > 0$, are already obtainable with VBF at the LHC [30–33]. Such scales will also be commonplace at energy-frontier colliders proposed to succeed the LHC [34–40]. This rings particularly true for multi-TeV $\mu^+\mu^-$ colliders. There, the VBF rate is so dominant the collider acts effectively as a "high-luminosity EW boson collider" [41] and shows promising sensitivity to SM and beyond the SM (BSM) physics [25, 41–55].

By virtue of the EW sector obeying a local $\mathrm{SU}(2)_L \otimes \mathrm{U}(1)_Y$ symmetry in the unbroken phase, some aspect of collinear factorization must survive at these colliders in the limit that $(p_T^2/Q^2)^k \to 0$ and $(M_V^2/Q^2)^k \to 0$. This is evident from the formulations of factorization

---

*Similarly, s-channel splittings of massive weak bosons from final-state partons can be factorized into a type of weak boson fragmentation function. For details, see Refs. [1–4] and references therein.
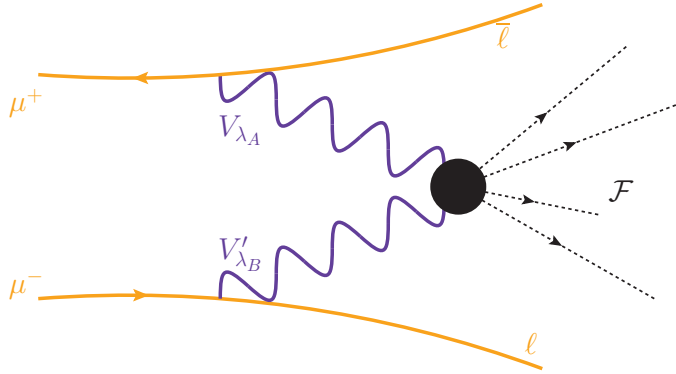
Figure 1. Diagrammatic representation of $\mu \to V_\lambda \ell$ splitting and VV' scattering in $\mu^+\mu^-$ collisions.

theorems and Sudakov exponentiation in QED and pQCD, which at times rely more on the presence of multiple, well-separated (hierarchical) mass scales than on being unbroken gauge theories [56–63]. Clearly, being an Abelian/non-Abelian or weakly/strongly coupled theory is less crucial for sufficiently inclusive processes. At the same time, differences between collinear factorization in pQCD and the EW theory must exist since lepton and hadron beams are not composed of weak isospin-averaged states [4, 64–66].

As a step to better understanding collinear factorization in the EW sector, we consider a framework that combines the EWA for helicity-polarized W and Z bosons with the Weizsäcker-Williams Approximation for helicity-polarized photons. We collectively label this the Effective Vector Boson Approximation (EVA).[†] In this framework and in the context of a multi-TeV $\mu^+\mu^-$ collider, we investigate the impact of and validity of (helicity-polarized) $\gamma/W/Z$ PDFs in $2 \to n$ process. Such processes that we consider include: associated and many-Higgs production, many-boson production, as well as associated and multi-top production. We extend recent studies [21, 25, 41, 67] by investigating universal and quasi-universal corrections to weak boson PDFs that appear naturally in their derivations. Specifically, we study universal power corrections of the form (p_T^2/Q^2), which spoil the accuracy of collinear factorization, and quasi-universal power corrections of the form (M_V^2/Q^2), which spoil the accuracy of the Goldstone Equivalence Theorem [68, 69]. Importantly, we also consider the role of universal and quasi-universal logarithmic corrections of the form $[\alpha_W \log(\mu_f^2/M_V^2)]$, by exploring scale variation and when the evolution variable in weak boson PDFs is defined in terms of transverse momentum (p_T) or virtuality (q). This is in addition to studying the role of helicity in both total and differential cross sections.

We find strong sensitivity to power corrections when hard-scattering scales Q are below $Q \sim 1$ TeV; for larger Q, we report agreement between full and approximated MEs when scale uncertainty bands, which can be large, are taken into account. More explicitly: we find that computations with the EWA can reproduce total and differential results within (large) scale uncertainties, so long as factorization-breaking power corrections are sufficiently suppressed. Even for asymptotically large energies, we find scale uncertainties remain large,

---

[†]Throughout this text, we use the term "EVA" when speaking generically about unpolarized or polarized EW boson PDFs, but use "EWA" when speaking exclusively about (un)polarized W/Z PDFs.

demonstrating a need for renormalization group (RG) evolution in our factorization theorem for high-energy muon collisions. To strengthen the parallels with pQCD, we give a proof-of-principle demonstration of matrix element matching with transverse weak boson PDFs and full MEs. Given these criteria, we go on to survey nearly two dozen $2 \to n$ VBF processes with the EVA in $\mu^+\mu^-$ collisions at $\sqrt{s} = 2 - 30$ TeV. Cross sections and their scale uncertainties are presented for both helicity-polarized and unpolarized initial states. To conduct this study, we report an implementation of the EVA into the general-purpose Monte Carlo event generator `MadGraph5_aMC@NLO` (`mg5amc`). Notably, this public implementation lays the groundwork for developing QCD-like matching prescriptions with initial/final state EW boson radiation as well as (polarized and unpolarized) PDFs that are RG evolved via the EW theory and pQCD. To further with this agenda, we also give some recommendations on using weak boson PDFs in high-energy lepton collisions.

The remainder of this work continues in the following order: In Sec. 2, we summarize the EVA formalism used throughout this work and present a factorization theorem for EW boson scattering in high-energy $\mu^+\mu^-$ collisions; for completeness, a derivation of helicity-polarized EW boson PDFs is given in App. A. In Sec. 3 we document our computational setup and numerical values for SM inputs. Sec. 4 is the first of two principle sections and where we revisit the validity of the EWA. Sec. 5 is the second of two principle sections and where we give a survey of $2 \to n$ VBF processes in the EVA. We conclude in Sec. 6. There, we give an extended discussion of our findings, reflecting particularly on the parallels we find with more subtle aspects of PDFs in QCD, e.g., the phenomenon of "precocious scaling." Finally, we provide some recommendations on using weak PDFs in high-energy lepton collisions in Sec. 6.1. App. B provides some instructions for reproducing our results and using (un)polarized EW boson PDFs in `mg5amc`.

2   The Effective Vector Boson Approximation for $\mu^+\mu^-$ collisions

In this section, we summarize the EVA, i.e., the framework in which we work, and its use in evaluating scattering cross sections in many-TeV $\mu^+\mu^-$ collisions. While we focus on muons, the EVA is, in principle, applicable to any lepton-lepton, lepton-hadron, and hadron-hadron collider configuration. Extension to other colliders, however, may require substitutions of gauge coupling charges and/or convolutions with additional PDFs [5]. In Sec. 2.1, we state a factorization theorem that will be the basis for all our numerical results and validation checks. In Sec. 2.2, we list the q^2 and p_T^2-evolved collinear PDFs that describe the density of EW bosons in muons at leading order (LO). Finally, we document for the completeness in Sec. 2.3 the PDFs for SM neutrinos from muons. The PDFs quoted below are derived in a technical appendix; see App. A for details.

2.1   A factorization theorem for $\mu^+\mu^-$ collisions

To described the fully differential production of an n-body, final state $\mathcal{F}$ with momenta $\{p_f\}$ via the high-energy VBF process $V_{\lambda_A} V'_{\lambda_B} \to \mathcal{F}$, where V_{λ_A} and V'_{λ_B} are helicity-polarized EW gauge bosons, in $\mu^+\mu^-$ collisions at a center-of-mass (c.m.) energy of $\sqrt{s}$, we invoke

the EVA. In practice, this means working from a factorization theorem given by

$$\sigma(\mu^+\mu^- \to \mathcal{F} + X) = \ f \otimes f \otimes \hat{\sigma} + \text{Power and Logarithmic Corrections} \tag{2.1}$$

$$= \sum_{V_{\lambda_A}, V'_{\lambda_B}} \int_{\tau_0}^1 d\xi_1 \int_{\tau_0/\xi_1}^1 d\xi_2 \int dPS_n$$

$$\times \ f_{V_{\lambda_A}/\mu^+}(\xi_1, \mu_f) f_{V'_{\lambda_B}/\mu^-}(\xi_2, \mu_f)$$

$$\times \ \frac{d\hat{\sigma}(V_{\lambda_A} V'_{\lambda_B} \to \mathcal{F})}{dPS_n}$$

$$+ \ \mathcal{O}\left(\frac{p_{T,l_k}^2}{M_{VV'}^4}\right) + \mathcal{O}\left(\frac{M_{V_k}^2}{M_{VV'}^4}\right) + \mathcal{O}\left(\frac{\alpha_W}{M_{VV'}^2}\log\frac{\mu_f^2}{M_{V_k}^2}\right). \tag{2.2}$$

Here, σ is the muon-level (beam-level) inclusive cross section for the production of $\mathcal{F}$ in association with an arbitrary state X. Explicitly, X consists of at least two leptons l, where $l = \mu^\pm, \nu_\mu$, or $\overline{\nu_\mu}$, in addition to particles originating from radiative corrections. The summation runs over all polarized EW boson $V_\lambda \in \{W_\lambda^\pm, Z_\lambda, \gamma_\lambda\}$, with $\lambda \in \{0, \pm 1\}$. Formally speaking, when the collection of states $\{V_\lambda\}$ is extended to left-handed (LH) and right-handed (RH) states $\nu_{\mu L}$ and $(\overline{\nu_\mu})_R$, the beam remnant X includes weak bosons.

For beams $k = 1,2$, the quantities $f_{V_\lambda/\mu^\pm}(\xi_k, \mu_f)$ are the PDFs that describe the likelihood that an unpolarized muon $\mu^\pm$ with energy $E_\mu = \sqrt{s}/2$ and momentum $p_\mu = E_\mu(1,0,0,\pm 1)$ contains a "parton" V with helicity λ, mass M_V, energy $E_V = \xi_k E_\mu$, and no transverse momentum p_{T,V_λ}. Generally, $E_V \neq E_{V'}$ in the frame of the (VV')-system since generally $M_V \neq M'_V$. In $f_{V_\lambda/\mu^\pm}$, the quantity μ_f is the collinear factorization scale and acts as the ultraviolet regulator of the PDF. Physically, μ_f is the phase space upper bound on the norm of the space-like momentum transfer $q = (p_\mu - p_l)$ carried by $V_\lambda(q)$; alternatively, μ_f can be interpreted as the upper bound on the p_T of lepton l in $\mu^\pm \to V_\lambda + l$ splitting. The (phase space) integrals over the momentum fractions ξ_k are bounded by the (dimensionless) kinematic threshold variable $\tau_0 = \min(M_{VV'}^2/s) = \min(M(\mathcal{F})/s)$. For $M_{VV'} < \sqrt{\tau_0 s}$, the (VV')-system has insufficient energy to produce the n-body state $\mathcal{F}$. The separately Lorentz-invariant phase space measure dPS_n is given by the usual expression

$$dPS_n(p_A + p_B; \{p_f\}) = (2\pi)^4 \delta^4\left(p_A + p_B - \sum_{p_j \in \{p_f\}}^n p_j\right) \prod_{p_j \in \{p_f\}}^n \frac{d^3 p_j}{(2\pi)^3 2E_j}. \tag{2.3}$$

In Eq. (2.2), $d\hat{\sigma}/dPS_n$ is the totally differential, "parton-level" cross section for the hard-scattering process $V_{\lambda_A}(p_A) V'_{\lambda_B}(p_B) \to \mathcal{F}(\{p_f\})$, which occurs at a hard scale

$$Q \equiv M_{VV'} = \sqrt{(p_A + p_B)^2} = \sqrt{\xi_1 \xi_2 s} \geq \sqrt{\tau_0 s} \gg M_V. \tag{2.4}$$

Due to this equality, we use the terms "hard-scattering system" and "(VV')-system" interchangeably. The helicity-polarized cross sections can be computed from the formula [70]

$$\frac{d\hat{\sigma}(V_{\lambda_A} V'_{\lambda_B} \to \mathcal{F})}{dPS_n} = \frac{1}{2\lambda^{1/2}(Q^2, M_V^2, M_{V'}^2)} \sum_{\text{dof}} |\mathcal{M}(V_{\lambda_A} V'_{\lambda_B} \to \mathcal{F})|^2. \tag{2.5}$$

Here, $\lambda(x, y, z) = (x - y - z)^2 - 4yz$, is the usual Källen kinematic function that accounts for the masses of initial-state particles. Unlike traditional leading-twist approximations that neglect masses of initial-state partons, the ME $\mathcal{M}(V_{\lambda_A} V'_{\lambda_B} \to \mathcal{F})$ is evaluated with nonzero $M_V, M_{V'}$. (In none of our results are weak boson masses set to zero.) Moreover, unlike the scattering of unpolarized partons in unpolarized beams, no spin-averaging factor for initial-states $V_{\lambda_A} V'_{\lambda_B}$ is needed for helicity-polarized cross sections that are paired with PDFs for helicity-polarized partons. The summation in Eq. (2.5) runs over all discrete degrees of freedom (dof) related to $\mathcal{F}$, e.g., electric charge and color helicity multiplicities. Importantly, if the summations $\sum_{V_{\lambda_A}, V'_{\lambda_B}}$ and $\sum_{\text{dof}}$ do not run over all helicity polarizations for VV' and $\mathcal{F}$, respectively, then the square of $\mathcal{M}$ is not Lorentz invariant. In such cases, an infrared-safe reference frame must be specified to define the helicities. For further details on evaluating helicity-polarized cross sections, particularly in relation to PDFs for polarized partons and polarized parton showers, see Ref. [70].

When deriving Eq. (2.2), a number of assumptions are made. Two important ones are both related to enforcing large separations of scales in $V_{\lambda_A} V'_{\lambda_B}$ scattering. The first is that weak bosons are massive but that the invariant mass of the $(V_{\lambda_A} V'_{\lambda_B})$-system is much larger, i.e., $M_V \ll M_{VV'}$. Nonzero M_V for $V = W, Z$ ensure that their longitudinal polarization vectors, which scale as $\varepsilon^\mu(p_V, \lambda = 0) \sim p_V^\mu/M_V + \mathcal{O}(M_V/E_V)$, remain nonvanishing when contracted with $\mu \to l$ currents. We reiterate that including initial-state parton masses here differs from typical treatments of QCD partons in hadron collisions, which are assumed massless in the absence of specialized schemes [12–15]. Outside this limit, Eq. (2.2) receives quasi-universal power corrections of the form $(M_V^{2k}/M_{VV'}^{2k+2})^k$ for $k > 1$, the size of which are quantified in Sec. 4.2. The qualifier "quasi-universal" refers to the fact that such corrections originate from the derivation of $f_{V_0^\pm}$ PDFs, and therefore appear for any $V_{\lambda_A} V'_{\lambda_V}$ scattering process with at least one longitudinally polarized $W_0^\pm$ or Z_0. It is worth noting that the Goldstone Equivalence Theorem requires that these terms be small [68, 69]; for further insights on relationship, see Refs. [4, 71–73].

The second important assumption is the stipulation that EW bosons are emitted at shallow angles in $\mu \to l + V_\lambda$ splittings, i.e., $p_{T,l} \sim p_{T,V_\lambda} \ll M_{VV'}$. This is a standard but necessary condition for collinear factorization in gauge theories [63, 74]. As in QCD computations, universal power corrections of the form $(p_{T,l}^{2k}/M_{VV'}^{2k+2})$ for $k > 1$ can be incorporated by higher-order perturbative computations, e.g., next-to-leading order (NLO) in α_W or α, parton showers, or ME matching to higher leg multiplicities. To be explicit, "universal" here refers to the fact that such corrections originate from the derivation of both $f_{V_0^\pm}$ and $f_{V_T^\pm}$ PDFs, meaning that they are present for any $V_{\lambda_A} V'_{\lambda_V}$ scattering process.

Notably, the absence of any EW Sudakov form factor in Eq. (2.2) implies that the factorization theorem is not scale invariant in an RG evolution sense. That is to say, the anomalous dimensions associated with PDFs $f_{V_{\lambda_A}/\mu^\pm}$ and $f_{V_{\lambda_B}/\mu^\mp}$ do not necessarily cancel those associated with the partonic cross section $\hat{\sigma}(V_{\lambda_A} V_{\lambda_B} \to \mathcal{F})$. (One can verify this by Mellin-transforming Eq. (2.2), and then taking the derivative with respect to $\log \mu_f^2$.) In its present form, Eq. (2.2) is subject to universal and quasi-universal logarithmic corrections of the form $\mathcal{O}[(\alpha_W/M_{VV'}^2) \log(\mu_f^2/M_{V_k}^2)]$, where $g_W = \sqrt{4\pi\alpha_W} \approx 0.65$ is the SM weak

coupling constant, due to working at only LO in the EW theory. Naïvely, one may argue that these corrections are sub-leading since they are coupling suppressed. However, g_W is not a small number and collinear logarithms can compensate for this. For instance: taking $\mu_f = 1 - 10$ TeV implies corrections from $(\alpha_W^2/4\pi) \log(\mu_f^2/M_W^2)$ that are $\mathcal{O}(20\% - 30\%)$. While we ultimately report in Sec. 4 a prescription for obtaining agreement between full and EWA-based calculations, the scale uncertainties reported there and in Sec. 5 undercut our findings. For precision computations, an RG-improved version EVA is necessary. However, incorporating these improvements, including the various subtleties related to γ_T/Z_T mixing [4, 25, 50, 75–78], which we neglect, is left to to future work.

Lastly, the expressions for EW boson PDFs $f_{V_{\lambda_A}/\mu^\pm}$ depend strongly on their precise formulation; compare for example Refs. [5–7, 20, 79–81]. As discussed in Sec. 4.4, seemingly innocuous conceptual differences can lead to substantial numerical differences in real computations. Therefore, we now summarize the PDFs used in this study.

2.2 q^2 and p_T^2-evolved collinear EW PDFs

In PDFs for $W_\lambda, Z_\lambda, \gamma_\lambda$ bosons from high-energy muons, one has the freedom to parameterize the momentum transfer in $\mu(p_\mu) \to l(p_l) + V_\lambda(q)$ splittings either by the squared virtuality $q^2 = (p_\mu - p_l)^2 < 0$ propagated by V_λ, or by the squared transverse momentum p_T^2 carried away by l. While the two quantities are related by $q^2(1 - \xi) = -p_T^2$, where $\xi = E_V/E_\mu$ is the fraction of μ's energy held by V_λ, the resulting PDF sets for transversely polarized V_λ differ analytically. Consequentially, for fixed z, λ, and μ_f, one can obtain large differences due a relative contribution that scale as $\delta f_{V_T/\mu^\pm} \sim \log(1 - \xi)$. This logarithm diverges in the large-ξ limit and corresponds to a nonzero q^2 but a vanishing p_T^2. Such differences have been sporadically discussed throughout the literature [18–20, 22, 23, 67, 80, 82] but not systematically compared. In light of this, we investigate both sets of PDFs.

For the couplings in Table 1, and assuming q^2 evolution, the LO PDFs for polarized $V_\lambda \in \{W_\lambda^\pm, Z_\lambda\}$ from LH (f_L) and RH (f_R) fermions in the hard scattering frame are

$$f_{V_+/f_L}(\xi, \mu_f^2) = \frac{g_V^2}{4\pi^2} \frac{g_L^2(1-\xi)^2}{2\xi} \log\left[\frac{\mu_f^2}{M_V^2}\right], \tag{2.6a}$$

$$f_{V_-/f_L}(\xi, \mu_f^2) = \frac{g_V^2}{4\pi^2} \frac{g_L^2}{2\xi} \log\left[\frac{\mu_f^2}{M_V^2}\right], \tag{2.6b}$$

$$f_{V_0/f_L}(\xi, \mu_f^2) = \frac{g_V^2}{4\pi^2} \frac{g_L^2(1-\xi)}{\xi}, \tag{2.6c}$$

$$f_{V_+/f_R}(\xi, \mu_f^2) = \left(\frac{g_R}{g_L}\right)^2 \times f_{V_-/f_L}(\xi, \mu_f^2), \tag{2.6d}$$

$$f_{V_-/f_R}(\xi, \mu_f^2) = \left(\frac{g_R}{g_L}\right)^2 \times f_{V_+/f_L}(\xi, \mu_f^2), \tag{2.6e}$$

$$f_{V_0/f_R}(\xi, \mu_f^2) = \left(\frac{g_R}{g_L}\right)^2 \times f_{V_0/f_L}(\xi, \mu_f^2). \tag{2.6f}$$

Vertex	Coupling strength	g_R^f	g_L^f	g_V^f	g_A^f
$V - f - f'$	$\tilde{g}$	$(g_V^f + g_A^f)$	$(g_V^f - g_A^f)$	$\frac{(g_R + g_L)}{2}$	$\frac{(g_R - g_L)}{2}$
$\gamma - f - f$	eQ^f	1	1	1	0
$Z - f - f$	$\frac{g}{\cos\theta_W}$	$-Q^f \sin^2\theta_W$	$(T_3^f)_L - Q^f \sin^2\theta_W$	$\frac{1}{2}(T_3^f)_L - Q^f \sin^2\theta_W$	$-\frac{1}{2}(T_3^f)_L$
$W - f - f'$	$\frac{g}{\sqrt{2}}$	0	1	$\frac{1}{2}$	$-\frac{1}{2}$

Table 1. EW chiral couplings and coupling strength normalizations used in the EVA for fermions f, f' with weak isospin charge $(T_3^f)_L = \pm 1/2$ and electric charge Q^f, with normalization $Q^\ell = -1$.

Choosing instead to integrate over p_T^2 leads analogously to the following PDFs for V_λ:

$$h_{V_+/f_L}(\xi, \mu_f^2) = \frac{g_V^2}{4\pi^2} \frac{g_L^2 (1-\xi)^2}{2\xi} \log\left[\frac{\mu_f^2}{(1-\xi)M_V^2}\right], \tag{2.7a}$$

$$h_{V_-/f_L}(\xi, \mu_f^2) = \frac{g_V^2}{4\pi^2} \frac{g_L^2}{2\xi} \log\left[\frac{\mu_f^2}{(1-\xi)M_V^2}\right], \tag{2.7b}$$

$$h_{V_0/f_L}(\xi, \mu_f^2) = \frac{g_V^2}{4\pi^2} \frac{g_L^2 (1-\xi)}{\xi}, \tag{2.7c}$$

$$h_{V_+/f_R}(\xi, \mu_f^2) = \left(\frac{g_R}{g_L}\right)^2 \times h_{V_-/f_L}(\xi, \mu_f^2), \tag{2.7d}$$

$$h_{V_-/f_R}(\xi, \mu_f^2) = \left(\frac{g_R}{g_L}\right)^2 \times h_{V_+/f_L}(\xi, \mu_f^2), \tag{2.7e}$$

$$h_{V_0/f_R}(\xi, \mu_f^2) = \left(\frac{g_R}{g_L}\right)^2 \times h_{V_0/f_L}(\xi, \mu_f^2). \tag{2.7f}$$

To obtain the LO PDF for γ_λ from polarized muons in either evolution scheme, one must make the replacement $M_V \to m_\mu$ in the f_{V_T} PDFs and neglect the f_{V_0} PDF. Given a scheme, we construct polarized EW boson PDFs for *unpolarized* muon beams, denoted by $f_{V_\lambda/\mu^\pm}$, from those PDFs for *polarized* muons, denote by $f_{V_\lambda/\mu^\pm_\lambda}$, through the relation

$$f_{V_\lambda/\mu^\pm}(\xi, \mu_f) = \frac{f_{V_\lambda/\mu^\pm_L}(\xi, \mu_f) + f_{V_\lambda/\mu^\pm_R}(\xi, \mu_f)}{2}. \tag{2.8}$$

As a technical note, both schemes are available in `mg5amc` (see App. B for details) but stress that RG evolution of EW boson PDFs from leptons is not yet supported.

Differences between the two sets of PDFs appear only in the collinear logarithms for transversely polarized V_λ. In this sense, the impact of $\log(1 - \xi)$ corrections is process dependent and thus is labeled "quasi-universal." The absence of scale evolution in PDFs for longitudinally polarized V_λ is well-known and implies that traditional means of estimating scale uncertainty in pQCD, e.g., three-point scale variation, are not applicable to longitudinally polarized weak boson PDFs. In principal, one can obtain $f_{V_T/f_{L/R}}$ from $h_{V_T/f_{L/R}}$, or vice versa, with appropriately chosen μ_f. To further highlight the parallels with pQCD,

we note that absorbing factors of $(1 - \xi)$ into factorization scales is common practice in Soft-Collinear Effective Field Theory (SCET) [83, 84]. We reiterate that the PDFs here are only accurate to $\mathcal{O}(\alpha_W^2)$, or $\mathcal{O}(\alpha_{\text{EM}}^2)$ for f_{γ_λ}. This means that charge-flipping splittings such as $\mu^- \to \gamma^* \to \mu^+$ and $\mu^- \to \gamma^* \to W^+$, which appear first at NLO, are neglected.

2.3 Collinear PDFs for SM neutrinos

We briefly note that the derivation of $W_\lambda^\pm$ PDFs in $\mu \to l + V_\lambda$ splitting also implies the existence of neutrino PDFs. As we are working in the SM, only massless, LH neutrinos (and RH antineutrinos) exist. Therefore, by probability conservation, the $\mu_L^- \to \nu_{\mu L}$ PDF at leading logarithmic accuracy when evolved by q^2 and p_T^2 are

$$f_{\nu_{\mu L}/\mu_L^-}(\xi, \mu_f^2) = f_{W_{\lambda=+}^-/\mu_L^-}\left((1-\xi), \mu_f^2\right) + f_{W_{\lambda=-}^-/\mu_L^-}\left((1-\xi), \mu_f^2\right) \tag{2.9}$$

$$= \frac{g^2}{16\pi^2}\left(\frac{1+\xi^2}{1-\xi}\right)\log\left[\frac{\mu_f^2}{M_V^2}\right], \tag{2.10}$$

$$h_{\nu_{\mu L}/\mu_L^-}(\xi, \mu_f^2) = h_{W_{\lambda=+}^-/\mu_L^-}\left((1-\xi), \mu_f^2\right) + h_{W_{\lambda=-}^-/\mu_L^-}\left((1-\xi), \mu_f^2\right) \tag{2.11}$$

$$= \frac{g^2}{16\pi^2}\left(\frac{1+\xi^2}{1-\xi}\right)\log\left[\frac{\mu_f^2}{\xi M_V^2}\right]. \tag{2.12}$$

As we are interested in VBF at $\mu^+\mu^-$ colliders, we do consider further the role of neutrino PDFs from muon beams; for recent discussion on these PDFs, see Ref. [25]. Moreover, while we have also implemented these PDFs into the public release of `mg5amc`, access to them is temporarily restricted due to the unregulated divergence at $\xi \to 1$. Likewise, throughout this study, we neglect the importance of $\mu \to \mu$ PDFs due to the complication of soft/collinear photon emissions, which necessitates resummation [85]; we refer readers to studies by Refs. [50, 85–87, 87, 88].

3 Computational Setup

In this section we summarize the computational framework used in this study. Here, we only document the Monte Carlo (MC) tool chain and its tuning. Details on the EVA itself and usage in `mg5amc` are documented in Sec. 2, App. A, and App. B.

To simulate high-p_T muon collisions, we employ an updated (released in the future as version 3.3.0) generator `MadGraph5_aMC@NLO` [89, 90]. In this software suite, fully differential events are obtained from tree-level ME that are constructed [91] and evaluated [92] using helicity amplitudes defined in the `HELAS` basis [93], with QCD color algebra decomposed according to color flow [94]. Helicity-polarized ME are obtained by truncating spin-averaging over initial-state states and/or spin-summing over final-state states [70]. Analysis of parton-level events is handled by `MadAnalysis5` [95, 96].

Standard Model Inputs

For all ME and PDFs, we take the following EW inputs and masses [97]

$$M_W = 80.419 \text{ GeV}, \quad M_Z = 91.188 \text{ GeV}, \quad G_F = 1.16639 \times 10^{-5} \text{ GeV}^2, \tag{3.1}$$

$$m_H = 125 \text{ GeV}, \quad m_t = 173 \text{ GeV}, \quad m_b = 4.7 \text{ GeV}. \tag{3.2}$$

This implies a QED coupling of $\alpha_{\text{QED}}^{-1}(\mu_r = M_Z) \approx 132.507$. While we consistently modify EW couplings EW inputs are varied but we do not RG-evolve them. Importantly, we have structured `mg5amc` such that EW couplings and masses present in EW boson PDFs are set to those values stipulated in the `param_card.dat` configuration file. Changes to EW inputs in this file are automatically propagated into EW boson PDFs. We reiterate that all ME and PDFs assume non-zero W and Z boson masses. We use the light lepton masses

$$m_e = 510.9989461 \times 10^{-6} \text{ GeV} \quad \text{and} \quad m_\mu = 105.6583745 \times 10^{-3} \text{ GeV} \tag{3.3}$$

for the collinear logarithms contained in the γ_λ PDFs. These masses are hard-coded into the γ_λ PDFs and are independent of `param_card.dat`. While it is technically possible use massless $e^\pm/\mu^\pm$ in MEs, in this paper we choose to use massive leptons.

4 EVA at high energies

A chief goal of factorization is to simplify in a systematic manner complicated, multi-scale MEs that describe many-body processes into a set of simpler, 1-to-2-scale MEs. In practice, this divide-and-conquer approach improves the efficiency and stability of numerical computations. Importantly, the formal perturbative accuracy of factorized calculations can also be improved through quasi-universal RGE methods, e.g., Sudakov resummation and DGLAP evolution. For the specific case of VBF in multi-TeV $\mu^+\mu^-$ collisions, factorizing collinear $\mu \to V_\lambda l$ splittings into weak boson PDFs enables one to reorganize computations of an inherent 3-scale, $2 \to (n+2)$ scattering process (the three scales being M_V, p_T^l and $M_{VV'}$) into the product of two 2-scale computations (M_V with $\mu_f \sim p_T^l$, and M_V with $M_{VV'}$) involving process-independent PDFs and process-dependent $2 \to n$ MEs.

As described in Sec. 2.1 and App. A, the EWA is accurate up to universal and quasi-universal power corrections of the order $\mathcal{O}(p_T^{l2}/M_{VV'}^2)$ and $\mathcal{O}(M_V^2/M_{VV'}^2)$, which originate from expanding the ME for transversely and longitudinally polarized weak bosons in $\mu \to V_\lambda l$ splittings, as well as universal and quasi-universal logarithmic corrections of the order $\mathcal{O}(\alpha_W \log(\mu_f^2/M_{VV'}^2))$, which stem from working at LO in the EW theory. In principle, both classes of corrections can be reduced via standard techniques, e.g., higher-order fixed order calculations and Sudakov resummation. In the absence of such improvements, however, there exist theoretical uncertainties in the formulation of weak PDFs that we now explore. In Sec. 4.1 we describe our common setup to study power-law and logarithmic corrections. We then study $\mathcal{O}(M_V^2/M_{VV'}^2)$ corrections in Sec. 4.2, and the dependence on collider energy in Sec. 4.3. A subclass of $\mathcal{O}(\alpha_W \log(\mu_f^2/M_{VV'}^2))$ corrections are then investigated in Sec. 4.4. Finally, in Sec. 4.5, we give a proof-of-principle demonstration of matrix element matching with transversely polarized weak boson PDFs and explore $\mathcal{O}(p_T^{l2}/M_{VV'}^2)$ corrections.

	$\sqrt{s} = 4$ TeV		$\sqrt{s} = 14$ TeV		$\sqrt{s} = 30$ TeV	
	σ_{EVA} [fb] (Polarization Fraction)					
$\sum_{\lambda_A,\lambda_B} W^+_{\lambda_A} W^-_{\lambda_B} \to HH$	$2.08\ ^{+4\%}_{-2\%}$	$(-)$	$6.01\ ^{+2\%}_{-1\%}$	$(-)$	$9.48\ ^{+2\%}_{-1\%}$	$(-)$
$W^+_0 W^-_0 \to HH$	2.03	(97%)	5.91	(98%)	9.16	(97%)
$W^\pm_0 W^\mp_T \to HH$	$560 \times 10^{-6}\ ^{+75\%}_{-73\%}$	$(< 0.5\%)$	$1.10 \times 10^{-3}\ ^{+72\%}_{-70\%}$	$(< 0.5\%)$	$1.44 \times 10^{-3}\ ^{+71\%}_{-70\%}$	$(< 0.5\%)$
$W^+_T W^-_T \to HH$	$51.5 \times 10^{-3}\ ^{+140\%}_{-75\%}$	(2%)	$113 \times 10^{-3}\ ^{+130\%}_{-72\%}$	(2%)	$156 \times 10^{-3}\ ^{+130\%}_{-769\%}$	(2%)
$\sum_{\lambda_A,\lambda_B} W^+_{\lambda_A} W^-_{\lambda_B} \to \gamma\gamma$	$146 \times 10^{-3}\ ^{+93\%}_{-60\%}$	$(-)$	$396 \times 10^{-3}\ ^{+76\%}_{-52\%}$	$(-)$	$519 \times 10^{-3}\ ^{+71\%}_{-50\%}$	$(-)$
$W^+_0 W^-_0 \to \gamma\gamma$	894×10^{-6}	(0.6%)	1.50×10^{-3}	$(< 0.5\%)$	1.70×10^{-3}	$(< 0.5\%)$
$W^\pm_0 W^\mp_T \to \gamma\gamma$	$3.56 \times 10^{-3}\ ^{+72\%}_{-63\%}$	(2%)	$5.88 \times 10^{-3}\ ^{+64\%}_{-58\%}$	(2%)	$6.55 \times 10^{-3}\ ^{+63\%}_{-57\%}$	(1%)
$W_T W_T \to \gamma\gamma$	$141 \times 10^{-3}\ ^{+94\%}_{-60\%}$	(97%)	$389 \times 10^{-3}\ ^{+76\%}_{-52\%}$	(98%)	$510 \times 10^{-3}\ ^{+71\%}_{-50\%}$	(98%)
	σ_{Full} [fb]					
$e^+\mu^- \to HH\ \bar\nu_e\nu_\mu$	1.26		4.43		9.60	
$e^+\mu^- \to \gamma\gamma\gamma\ \bar\nu_e\nu_\mu$	$248 \cdot 10^{-3}$		$558 \cdot 10^{-3}$		$4.04 \cdot 10^{-1}$	

Table 2. Upper: Unpolarized and polarized, EWA-level cross sections [fb] for the process $W^+_{\lambda_A} W^-_{\lambda_B} \to HH$, with scale uncertainties [%] and polarization fractions [%], in $e^+\mu^-$ collisions at $\sqrt{s} = 4$, 14, and 30 TeV. Middle: The same but for the process $W^+_{\lambda_A} W^-_{\lambda_B} \to \gamma\gamma$, assuming the phase space cuts of Eq. (4.4). Lower: The cross sections for the analogous processes using the full $2 \to 4$ or $2 \to 5$ ME. No restrictions are applied to the invariant masses $M(HH)$ and $M(\gamma\gamma)$.

4.1 Process choice and polarization decomposition

To quantify uncertainties that stem from factorizing polarized EW bosons from initial-state $\mu^\pm \to V_\lambda l$ emissions into PDFs, we chose the two benchmark processes

$$e^+\mu^- \to HH\ \bar\nu_e\nu_\mu \quad \text{and} \quad e^+\mu^- \to \gamma\gamma\gamma\ \bar\nu_e\nu_\mu\,. \tag{4.1}$$

Following Ref. [41], we work with $e^+\mu^-$ collisions in order to remove s-channel, $\mu^+\mu^-$ annihilation diagrams in a gauge-invariant manner. As such channels have sizable contributions to inclusive cross sections, their removal helps isolate the VBF sub-processes. Under the EWA, these beam-level processes correspond to the partonic processes

$$\sum_{\lambda_A,\lambda_B \in \{0,\pm 1\}} W^+_{\lambda_A} W^-_{\lambda_B} \to HH \quad \text{and} \quad \sum_{\lambda_A,\lambda_B \in \{0,\pm 1\}} W^+_{\lambda_A} W^-_{\lambda_B} \to \gamma\gamma\,. \tag{4.2}$$

In practice, we restrict ourselves throughout this section to the EWA helicity configurations

$$W^+_0 W^-_0 \to HH \quad \text{and} \quad \sum_{\lambda_A,\lambda_B \in \{\pm 1\}} W^+_{\lambda_A} W^-_{\lambda_B} \to \gamma\gamma\,. \tag{4.3}$$

We consider these specific processes and configurations due to the high purity of helicity polarizations that drive them. For polarizations λ_A and λ_B defined in the (W^+W^-) frame, we find by explicit calculation [70] that $97\% - 99\%$ of HH production in the EWA is dominated by longitudinally polarized W^+W^- scattering, i.e., $(\lambda_A, \lambda_B) = (0, 0)$, for $\sqrt{s} = 4 - 30$ TeV. In contrast, $\gamma\gamma\gamma$ production is driven at the $97\% - 99\%$ level, albeit with a large scale uncertainty, by transversely polarized W^+W^- scattering, i.e., $(\lambda_A, \lambda_B) = (T, T')$, where $T, T' = \pm 1$, when assuming the following fiducial phase space cuts on photons

$$p_T^\gamma > 50 \text{ GeV}, \quad |\eta^\gamma| < 3, \quad \text{and} \quad \Delta R(\gamma, \gamma) > 0.4. \tag{4.4}$$

In making this distinction between $(0,0)$ and (T,T') configurations, we can showcase possible differences of the EWA as applied to longitudinal and transverse polarizations. Many other processes, such as heavy Higgs production and top quark pair production, receive comparable contributions from multiple polarization configurations, which we believe can lead to ambiguities in interpreting the following comparisons.

For the $\gamma\gamma\gamma$ process, we focus on PDF evolution by virtuality (q^2) and set the baseline collinear factorization scale to be half the partonic c.m. energy, given by

$$\mu_f = \zeta \frac{\sqrt{\hat{s}}}{2} = \zeta \frac{M_{VV'}}{2}, \quad \text{with} \quad \zeta = 1. \tag{4.5}$$

Three-point scale uncertainties for $W_T^{\pm}$ PDFs are obtained by varying ζ discretely over the range $\zeta \in \{0.5, 1.0, 2.0\}$. For representative collider energies $\sqrt{s} = 4$, 14, and 30 TeV, the beam-level cross sections under the EWA (σ_{EVA}), scale uncertainties [%], and polarization fractions [%] for $W_{\lambda_A}^+ W_{\lambda_B}^- \to HH$ and $\gamma\gamma\gamma$ are summarized in the top two panels of Table 2. For comparison, we show in the lower panel of Table 2 the corresponding cross sections (σ_{Full}) using the full MEs, i.e., without the EWA. The sizable differences between σ_{EVA} and σ_{Full}, as well as the large scale uncertainties of the EWA result, will now be discussed.

4.2 Dependence on hard-scattering scale

We start our presentation on EWA uncertainties with what we find to be the most telling: that the accuracy of EWA cross sections for VBF depends crucially on the size of $(M_V^2/M_{VV'}^2)$ power corrections. To show this, we plot in Fig. 2(a) the invariant mass distributions at $\sqrt{s} = 4$ TeV of the (HH)-system using the full $2 \to 4$ ME (solid) and the EVA $2 \to 2$ ME (dashed). We assume two scenarios: one where the SM Higgs vev is its usual value $\sqrt{2}\langle\Phi\rangle = v_{\text{SM}} \approx 246$ GeV (dark, lower curves), and a hypothetical situation where the vev is reduced by a factor 10 (light, upper curves), i.e., where $\sqrt{2}\langle\Phi\rangle = v_{\text{SM}}/10 \approx 24.6$ GeV. In the small-vev scenario, we keep M_H and all EW gauge couplings to be their SM values in the Thomson limit. This implies $M_W \approx 8.04$ GeV and $M_Z \approx 9.14$ GeV.

Focusing first on the SM case, we clearly see that the EWA and the full ME computations are in agreement for $M(HH) \gtrsim 1$ TeV. Below this threshold, the EWA curve significantly overestimate the full ME. In the lowest bins, the differences between the curves reach approximately factors of $3 - 5$. This excess in the EVA prediction accounts for the differences in cross sections reported in Table 2. As seen in the ME of Eq. (A.56) in App. A, differences between the full ME and $f_{W_0^{\pm}}$ PDFs consist of corrections associated with expanding in powers of $(M_W^2/M^2(HH))$ and $(p_T^{\nu 2}/M^2(HH)) \sim (M_W^2/M^2(HH))$. Importantly, we can rule out a meaningful dependence on μ_f since $W_{\lambda_A}^+ W_{\lambda_B}^- \to HH$ is driven almost exclusively by $W_0^+ W_0^-$ scattering. To check that these power corrections are driving the disparity between the full and approximated MEs, we turn to the reduced-vev case. Remarkably, if we reduce M_W by a factor of 10, the disagreement between the EWA and the full ME disappears to within MC statistical uncertainties.

The same scenarios are presented for $\gamma\gamma\gamma$ production in Fig. 2 (b). There, we plot the invariant mass distribution of the $(\gamma\gamma\gamma)$-system for the full (solid) and EWA MEs. As $W_{\lambda_A}^+ W_{\lambda_B}^- \to \gamma\gamma\gamma$ is driven by $W_T^+ W_T^-$ scattering, there is an ambiguity associated with
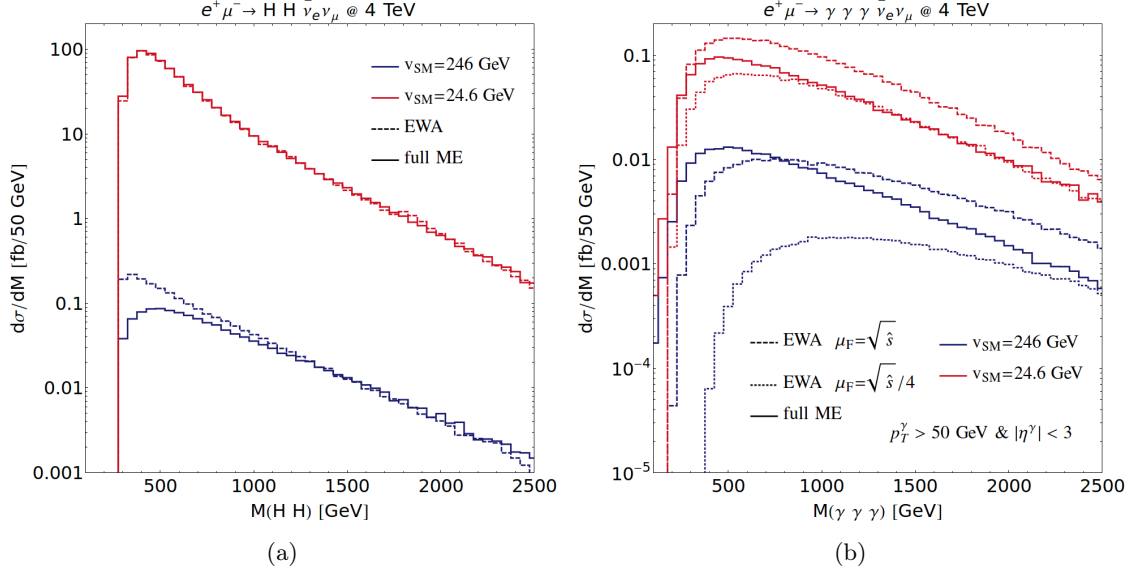
Figure 2. (a) The invariant mass distribution $M(HH)$ of the process $W^+W^- \to HH$, as predicted by the full $2 \to 4$ ME (solid) and the EWA $W_0^+W_0^- \to HH$ ME (dash) at $\sqrt{s} = 4$ TeV, assuming the SM vev $\sqrt{2}\langle\Phi\rangle = v_{SM} \approx 246$ GeV (darker, lower curves) and a scenario where $\sqrt{2}\langle\Phi\rangle = v_{SM}/10$ (lighter, upper curves). (b) Same but for the $M(\gamma\gamma\gamma)$ distribution of the process $W^+W^- \to \gamma\gamma\gamma$, assuming the fiducial cuts in Eq. (4.4), and for the $W_T^+W_T^- \to \gamma\gamma\gamma$ ME in the EWA with $\mu_f = M(\gamma\gamma\gamma)$ (dash) and $\mu_f = M(\gamma\gamma\gamma)/4$ (dots).

our choice for μ_f in the $W_T^\pm$ PDFs. Therefore, we consider the envelop spanned by setting $\mu_f = \sqrt{\hat{s}}$ (dash) and $\mu_f = \sqrt{\hat{s}}/4$ (dot). In the SM case (light curves), the scale uncertainty envelope spans a huge gap that sandwiches the full ME for $M(\gamma\gamma\gamma) \gtrsim 750$ GeV. This large scale variation can be understood by considering the logarithms in the $W_T^\pm$ PDFs themselves. For a fixed $M(\gamma\gamma\gamma)$, the ratio of the two EVA distributions is given by

$$
\left.\frac{\frac{d\sigma_{\mathrm{EVA}}}{dM(\gamma\gamma\gamma)}\big|_{\mu_f=\sqrt{\hat{s}}}}{\frac{d\sigma_{\mathrm{EVA}}}{dM(\gamma\gamma\gamma)}\big|_{\mu_f=\sqrt{\hat{s}}/4}}\right|_{\text{fixed } \mathrm{M}(\gamma\gamma\gamma)} = \left.\frac{\log^2\left(\frac{\hat{s}}{M_W^2}\right)}{\log^2\left(\frac{\hat{s}}{16M_W^2}\right)}\right|_{\hat{s}=M^2(\gamma\gamma\gamma)} \tag{4.6}
$$

$$
= \frac{\log^2 \frac{M^2(\gamma\gamma\gamma)}{M_W^2}}{\log^2 \frac{M^2(\gamma\gamma\gamma)}{M_W^2} + \log^2(16) - 2\log(16)\log\frac{M^2(\gamma\gamma\gamma)}{M_W^2}}. \tag{4.7}
$$

For the representative triphoton invariant masses $M(\gamma\gamma\gamma) \in \{0.5, 1, 2, 2.5\}$ TeV, we obtain roughly the respective ratios $\{17, 4.9, 3.1, 2.8\}$, in agreement with the distribution. For $M(\gamma\gamma\gamma) \lesssim 750$ GeV, the full ME curve sits just above the EWA envelope. This is in contrast to $W_0^+W_0^- \to HH$, where the full ME distribution sits below the EWA rate. We attribute this to $W_T^+W_{T'}^-$ scattering having a weaker dependence on power corrections than $W_0^+W_0^-$ scattering. As seen in the ME of Eq. (A.47) in App. A, differences between the full ME and $f_{W_T^\pm}$ PDFs are associated with expanding in powers of $(p_T^{\nu 2}/M^2(HH)) \sim (M_W^2/M^2(HH))$. However, there is no second expansion in powers of $(M_W^2/M^2(\gamma\gamma\gamma))$

	σ_{EVA} [fb] (Polarization Fraction)					
	$\sqrt{s} = 4$ TeV		$\sqrt{s} = 14$ TeV		$\sqrt{s} = 30$ TeV	
$\sum_{\lambda_A,\lambda_B} W^+_{\lambda_A} W^-_{\lambda_B} \to HH$	$364 \times 10^{-3} \, {}^{+2\%}_{-2\%}$	$(-)$	$2.44 \, {}^{+1\%}_{-1\%}$	$(-)$	$4.63 \, {}^{+1\%}_{-1\%}$	$(-)$
$W^+_0 W^-_0 \to HH$	353×10^{-3}	(97%)	2.41	(99%)	4.59	(99%)
$W^\pm_0 W^\mp_T \to HH$	$13.7 \times 10^{-6} \, {}^{+34\%}_{-34\%}$	$(< 0.5\%)$	$47.6 \times 10^{-6} \, {}^{+34\%}_{-34\%}$	$(< 0.5\%)$	$71.5 \times 10^{-6} \, {}^{+33\%}_{-33\%}$	$(< 0.5\%)$
$W^+_T W^-_T \to HH$	$10.8 \times 10^{-3} \, {}^{+75\%}_{-54\%}$	(3%)	$34.6 \times 10^{-3} \, {}^{+71\%}_{-52\%}$	(1%)	$53.1 \times 10^{-3} \, {}^{+69\%}_{-50\%}$	(1%)
$\sum_{\lambda_A,\lambda_B} W^+_{\lambda_A} W^-_{\lambda_B} \to \gamma\gamma\gamma$	$87.9 \times 10^{-3} \, {}^{+70\%}_{-51\%}$	$(-)$	$308 \times 10^{-3} \, {}^{+62\%}_{-46\%}$	$(-)$	$423 \times 10^{-3} \, {}^{+59\%}_{-45\%}$	$(-)$
$W^+_0 W^-_0 \to \gamma\gamma\gamma$	36.8×10^{-6}	$(< 0.5\%)$	166×10^{-6}	$(< 0.5\%)$	240×10^{-6}	$(< 0.5\%)$
$W^\pm_0 W^\mp_T \to \gamma\gamma\gamma$	$572 \times 10^{-6} \, {}^{+33\%}_{-33\%}$	(1%)	$1.53 \times 10^{-3} \, {}^{+31\%}_{-31\%}$	(0.5%)	$1.86 \times 10^{-3} \, {}^{+31\%}_{-31\%}$	$(< 0.5\%)$
$W_T W_T \to \gamma\gamma\gamma$	$87.3 \times 10^{-3} \, {}^{+71\%}_{-52\%}$	(99%)	$307 \times 10^{-3} \, {}^{+62\%}_{-47\%}$	(99%)	$421 \times 10^{-3} \, {}^{+59\%}_{-45\%}$	(99%)
	σ_{Full} [fb]					
$e^+ \mu^- \to HH \, \bar{\nu}_e \nu_\mu$	$325 \cdot 10^{-3}$		2.31		4.61	
$e^+ \mu^- \to \gamma\gamma\gamma \, \bar{\nu}_e \nu_\mu$	$84.8 \cdot 10^{-3}$		$309 \cdot 10^{-3}$		$412 \cdot 10^{-3}$	

Table 3. Same as Table 2 but requiring $M(HH) > 1$ TeV and $M(\gamma\gamma\gamma) > 1$ TeV.

as one has for the $f_{W^\pm_0}$ PDFs. For $M(\gamma\gamma\gamma) > 1.5$ TeV, the distribution of the full ME approaches the EWA curve for $\mu_f = \sqrt{\hat{s}}/4$, suggesting a preferred choice for setting μ_f.

In the reduced-vev scenario (dark curves), we observe several noteworthy features. First is an improved agreement between the full and EWA distributions for $M(\gamma\gamma\gamma) \gtrsim 250$ GeV. For even lower invariant masses, the full ME is again higher than the EWA band. Second, we find that the full ME converges to the EWA curve for $\mu_f = \sqrt{\hat{s}}/4$ when $M(\gamma\gamma\gamma) \gtrsim 750$ TeV. Third is the appearance of a smaller scale uncertainty envelope, in accordance with Eq. (4.7). Numerically, this follows from the fact that for small variations of the argument x, the quantity $\log(x)$ varies less when x is large than when x is near unity. Physically, this means that in the reduced-vev case, typical $M(\gamma\gamma\gamma)$ are further away from the W's mass threshold, and therefore is less sensitive to $\mathcal{O}(\log(M^2(\gamma\gamma\gamma)/M^2_W))$ variations. Despite being smaller in this scenario, we stress that the scale uncertainty band remains sizable. For instance: using Eq. (4.7) and our benchmark values for $M(\gamma\gamma\gamma)$, we obtain the ratios $\{2.3, 2.0, 1.8, 1.7\}$. This indicates that for realistic EW boson masses, one must go to asymptotically large $M(\gamma\gamma\gamma)$ in order to obtain $\mathcal{O}(10\% - 20\%)$ uncertainties. From an alternative perspective, the large μ_f dependence is indicative of the need to extend the factorization theorem of Eq. (2.2) by an EW Sudakov form factor and/or RG evolution for weak boson PDFs, as studied in Refs. [4, 25, 50, 75, 78, 98–100].

From these distributions, we can conclude that the EWA is acutely sensitive to power corrections of the form $(M^2_V/M^2_{VV'})$. This is particularly true when scattering longitudinally polarized weak bosons. Distributions also suggest a weaker dependence on power corrections when scattering transversely polarized weak bosons. We attribute this difference to the different expansions needed to derive longitudinal and transverse weak boson PDFs: W_T PDFs require a single power expansion whereas W_0 PDFs require a double expansion. Altogether, this points to evidence of the EWA's success for both transverse and longitudinal $V_{\lambda_A} V'_{\lambda_B}$ scattering when $M_{VV'} > \mathcal{O}(1 \text{ TeV})$, or $(M^2_V/M^2_{VV'}) \lesssim 0.01$. To further demonstrate this at the level of cross sections, we show in Table 3 the same quantities
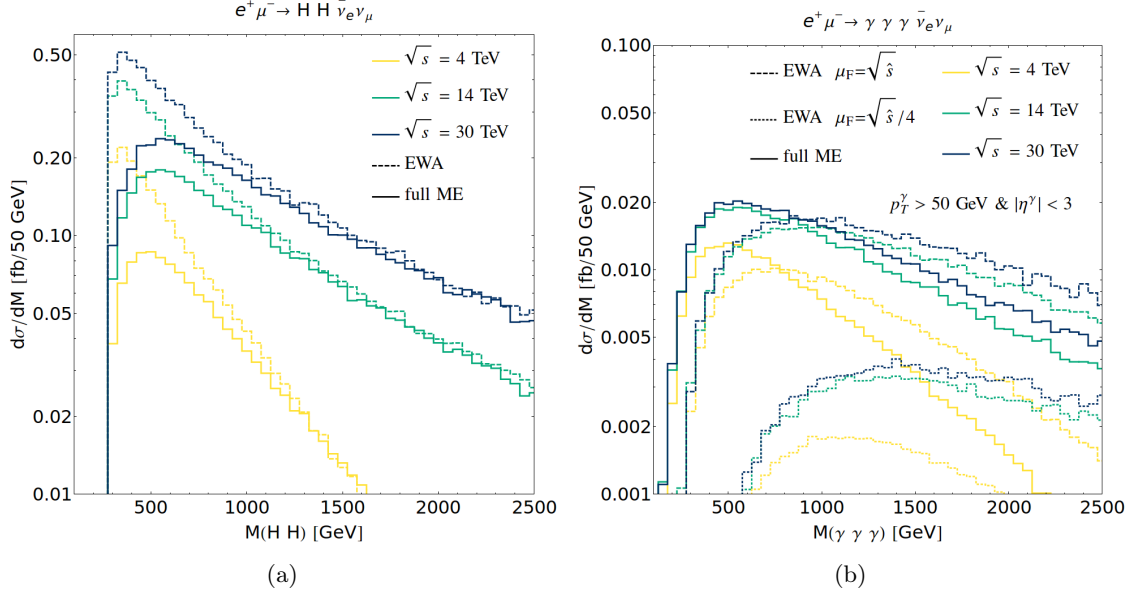
Figure 3. (a) The invariant mass distribution $M(HH)$ of the process $W^+W^- \to HH$, as predicted by the full $2 \to 4$ ME (solid) and the EVA $W_0^+W_0^- \to HH$ ME (dash) at $\sqrt{s} = 4$ TeV (lower light curves) and 14 TeV (upper dark curves). (b) Same but for the $M(\gamma\gamma\gamma)$ distribution of the process $W^+W^- \to \gamma\gamma\gamma$, assuming the fiducial cuts in Eq. (4.4), and for the $W_T^+W_T^- \to \gamma\gamma\gamma$ ME in the EWA with $\mu_f = M(\gamma\gamma\gamma)$ (dash) and $\mu_f = M(\gamma\gamma\gamma)/4$ (dots).

as in Table 2 but require also that $M(HH) > 1$ TeV and $M(\gamma\gamma\gamma) > 1$ TeV. The improved agreement between the full and EWA computations is due to the cuts on $M(WW)$.

4.3 Dependence on collider energy

In light of the above, we consider now the impact collider energy on the EWA's accuracy. Increasing $\sqrt{s}$ has two prominent effects on $V_{\lambda_A} V'_{\lambda_B}$ scattering: (i) For fixed momentum fractions ξ_1 and ξ_2, more energetic $\mu^+\mu^-$ collisions lead to more energetic (VV')-systems, with $M_{VV'}^2 = \xi_1\xi_2 s$. The corresponding enhancement of collinear logarithms indicates an enlargement of collinear regions of phase space. (ii) For a fixed hard-scattering scale $M_{VV'}$, increasing the collider energy leads to probing smaller ξ_1 and ξ_2. The corresponding enhancement of soft logarithms similarly indicates an enlargement of soft regions of phase space. (These soft logarithms appear after integration of ξ_i over the PDF $f_{V_\lambda}(\xi_i) \sim 1/\xi_i$.)

To explore these effects, we present in Fig. 3 the invariant mass distributions of (a) the (HH)-system and (b) the $(\gamma\gamma\gamma)$-system at $\sqrt{s} = 4$ TeV (light) and 14 TeV (dark), assuming the full MEs for the processes in Eq. (4.1) (solid), and the EWA MEs for the processes in Eq. (4.3) (dash). For the $W_T^+W_T^- \to \gamma\gamma\gamma$ process, we show the scale variation envelop obtained by setting $\mu_f = \sqrt{\hat{s}}$ (dash) and $\mu_f = \sqrt{\hat{s}}/4$ (dot).

Focusing on the $M(HH)$ distribution in Fig. 3(a), several observations can be made. We start with the anticipated jump in cross section for increasing $\sqrt{s}$. For both the EWA and the full MEs, we find that increasing the collider energy by a factor of 3.5 causes all total cross sections to increase by about a factor of 3 (see Table 2). Increases are much

more dramatic at the differential level for $M(HH) \gtrsim 1.5$ TeV due to the significant opening of phase space. In this regime, we also find good agreement with the normalization and shape between the EWA and full MEs. At lower invariant masses, particularly for $M(HH) \lesssim 500$ GeV, we find that the EWA overestimates the full ME in the same manner as observed in the previous section. In this regime, the EWA distributions increase more quickly with rising $\sqrt{s}$ than the full ME distributions: in the lowest $M(HH)$ bins, the EWA ME overestimates the full ME by about a factor of $3 - 5$ at $\sqrt{s} = 4$ TeV and by about $3.4 - 4.7$ at 30 TeV. As longitudinal weak boson PDFs do not contain collinear logarithms, the enhancements in Fig. 3(a) are driven exclusively by soft logarithms. This implies that the EWA favors the production of relatively softer $W_0^\pm$, and hence lower $M(HH)$, a phenomenon that is sometimes [4] described as "ultra collinear enhancements." Consequentially, increasing the collider energy reinforces the sensitivity to $(M_W^2/M^2(HH))$ power corrections, which must be negative. Despite this, the distributions show that regardless of $\sqrt{s}$ the EWA converges to the full ME computation for $M(HH) \gtrsim 1$ TeV.

Turning to the $M(\gamma\gamma\gamma)$ distribution in Fig. 3(b), we observe several of the same characteristics. Foremost we find that the full ME distribution consistently sits within the EVA scale uncertainty band for $M(\gamma\gamma\gamma) \gtrsim 750$ GeV $- 1$ TeV, for all $\sqrt{s} = 4 - 30$ TeV. Though, for increasing $\sqrt{s}$ we find that the full ME expectation migrates away from the $\mu_f = \sqrt{s}/4$ boundary and towards the envelope's center. For a fixed $M(\gamma\gamma\gamma)$, we find that the thicknesses of the μ_f uncertainty bands remain about the same for increasing $\sqrt{s}$, with changes just outside MC statistical uncertainties. This is consistent with the ratio expression of Eq. (4.7), which does not obviously suggest an additional dependence on collider energy once $M(\gamma\gamma\gamma)$ is fixed. An important difference with respect to the $M(HH)$ case is the preference for larger values of $M(\gamma\gamma\gamma)$ with increasing $\sqrt{s}$. (For $W_0^+ W_0^- \to HH$, smaller invariant masses are preferred at increasing collider energy.) As $W_T^+ W_T^- \to \gamma\gamma\gamma$ is devoid of possible ME-level enhancements from longitudinal polarizations, we attribute these behaviors to the collinear logarithm contained in the $f_{W_T^\pm}$ PDF, which favors producing larger invariant masses. Notably, the collinear logarithms reinforce the accuracy of the EVA by favoring phase space regions where $(M_W^2/M^2(\gamma\gamma\gamma))$ is small.

4.4 Dependence on evolution variable

As shown in Sec. 2 and App. A, EW boson PDFs can be constructed using either the virtuality q of V_λ or transverse momentum p_T of l as the evolution variable in collinear $\mu \to V_\lambda l$ splitting. Given that the expressions for the $f_{W_T^\pm}$ PDFs differ, we investigate whether these schemes give appreciably different results. To explore this, we focus on the process $W_T^+ W_{T'}^- \to \gamma\gamma\gamma$ since the $f_{W_0^\pm}$ PDFs are the same under both schemes.

In Fig. 4(a), we show the invariant mass distribution of the $(\gamma\gamma\gamma)$-system in $W_T^+ W_{T'}^- \to \gamma\gamma\gamma$ at $\sqrt{s} = 4$ TeV using the full ME for the $2 \to 5$ scattering process (solid) and the analogous process under the EWA. For the EWA curves, we consider the scale variation envelop spanned by setting $\mu_f = \sqrt{\hat{s}}$ (dash) and $\mu_f = \sqrt{\hat{s}}/4$ (dot) for evolution by q^2 (thick curves) and evolution by p_T^2 (thin curves). We also impose the fiducial cuts in Eq. (4.4). As found in previous subsections, the distribution for the full ME sits in the EWA envelope for $M(\gamma\gamma\gamma) \gtrsim 750$ GeV, when assuming evolution by q^2. In comparison, the evolution-by-p_T^2
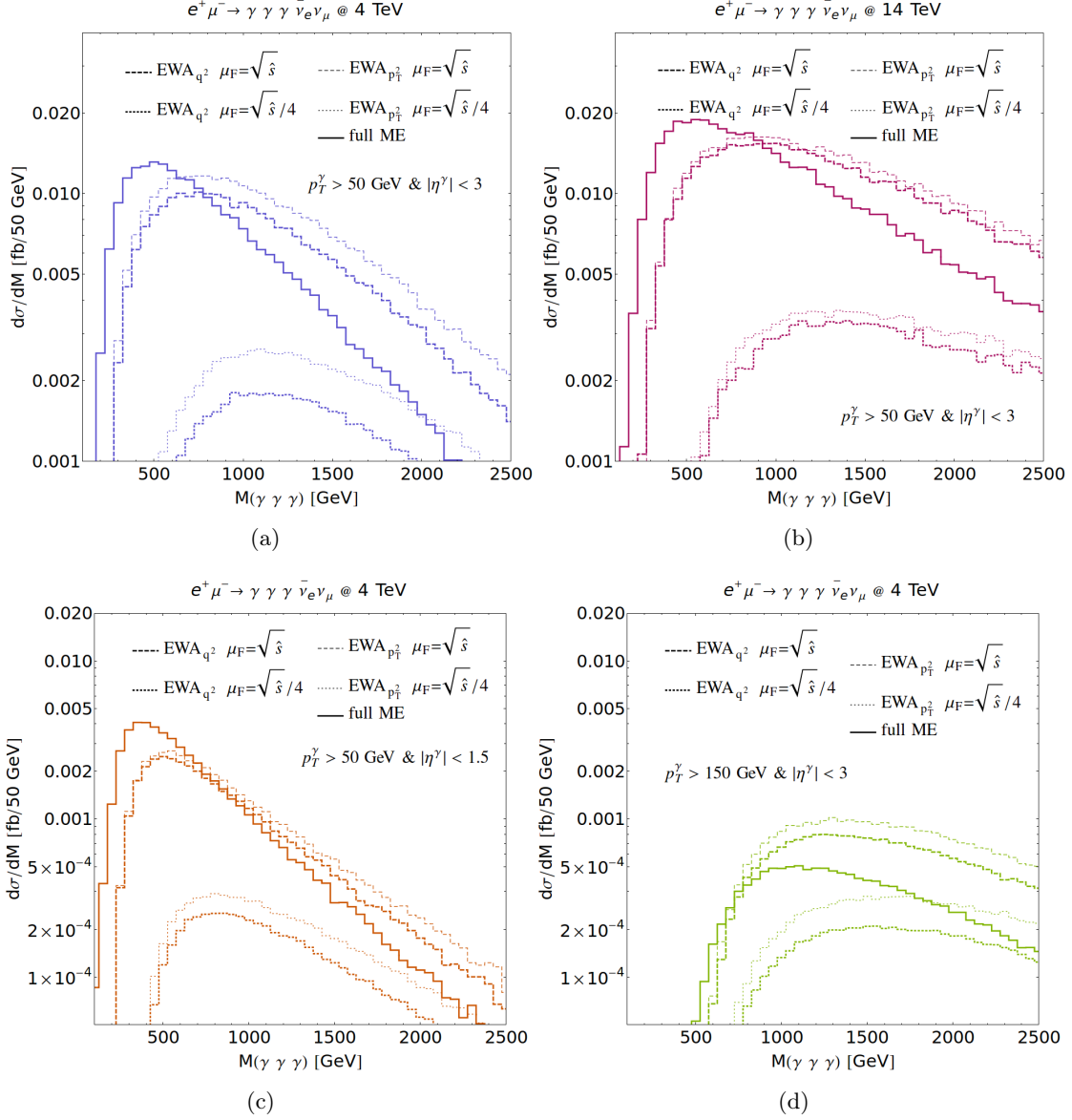
Figure 4. (a) The invariant $M(\gamma\gamma\gamma)$ distribution of the process $W^+W^- \to \gamma\gamma\gamma$, as predicted by the full $2 \to 5$ ME (solid) and the EVA $W_T^+ W_T^- \to \gamma\gamma\gamma$ ME at $\sqrt{s} = 4$ TeV, assuming f_{W_T} PDF evolution by virtuality q^2 (thick lines) and transverse momentum p_T^2 (thin lines), with $\mu_f = M(\gamma\gamma\gamma)$ (dash) and $\mu_f = M(\gamma\gamma\gamma)/4$ (dots). (b) The same as (a) but for $\sqrt{s} = 14$ TeV. (c) The same as (a) but for $|\eta^\gamma| < 1.5$. (c) The same as (a) but for $p_T^\gamma > 150$ GeV.

envelope is systematically shifted upward to a larger set of rates. Notably, this leads to the $\mu_f = \sqrt{\hat{s}}/4$ curve for evolution by p_T^2 to overestimate the full ME when $M(\gamma\gamma\gamma) \gtrsim 2$ TeV. This shift is entirely due to the different arguments in the PDFs' collinear logarithms.

More specifically, for evolution by q^2, one has $f_{W_T^\pm}(\xi, \mu_f) \propto \log(\mu_f^2/M_W^2)$, whereas for evolution by p_T^2, one has $h_{W_T^\pm}(\xi, \mu_f) \propto \log(\mu_f^2/(1-\xi)M_W^2)$. This difference implies that for a fixed factorization scale, the logarithm in the evolution-by-p_T^2 PDF is relatively enhanced

by a factor of $1/(1-\xi)$. This favors larger momentum fractions and therefore harder invariant mass distributions since $M^2(\gamma\gamma\gamma) = \xi_1\xi_2 s$. This enhancement and subsequent disagreement do not imply that evolution-by-p_T^2 scheme itself is incorrect. It only indicates that setting $\mu_f = \sqrt{\hat{s}}$ or $\mu_f = \sqrt{\hat{s}}/4$ are poor choices of factorization scale for this process and collider energy. Obviously, setting $\mu_f = \sqrt{(1-\xi)\hat{s}}$ or $\mu_f = \sqrt{(1-\xi)\hat{s}}/4$, which is a common practice SCET [83, 84], would recover the results for evolving by q^2.

In Fig. 4(b), we show the invariant mass distribution but for $\sqrt{s} = 14$ TeV. Remarkably, we find that two the envelopes converge, and differences between the two evolution schemes are within MC statistical uncertainties. Importantly, the full ME distribution remains inside both envelopes for $M(\gamma\gamma\gamma) \gtrsim 750$ GeV. To understand this improved agreement, recall that when the hard scattering scale $M(\gamma\gamma\gamma)$ is fixed, one probes smaller momentum fractions for increasing collider energies. This implies that as $\sqrt{s}$ increases, the $1/(1-\xi)$ enhancements cease and systematically approach unity, i.e., $1/(1-\xi) \to 1$.

In Fig. 4(c) and (d), we investigate the impact of tighter phase space cuts on the final-state system. In particular, we consider the cases when photons are (c) more central with $|\eta^\gamma| < 1.5$, and (d) harder with $p_T^\gamma > 150$ GeV. Aside from an obvious reduction in cross section, a few qualitative observations are worth reporting. In figure (c), we observe a shift in the distribution to smaller $M(\gamma\gamma\gamma)$, whereas in figure (d) the shift is to larger $M(\gamma\gamma\gamma)$. In both cases, the change is kinematical. Consider the invariant mass of the entire three-photon system in terms of two-photon systems, i.e.,

$$M^2(\gamma\gamma\gamma) = 2M(\gamma_1\gamma_2) + 2M(\gamma_2\gamma_3) + 2M(\gamma_1\gamma_3), \quad \text{where} \tag{4.8}$$

$$M^2(\gamma_i\gamma_j) \sim p_T^i p_T^j [(y_i - y_j)^2 + (\phi_i - \phi_j)^2]. \tag{4.9}$$

Here, η_i and ϕ_i are the pseudorapidity and azimuth of γ_i. Requiring a smaller $|\eta^\gamma|$ window leads to smaller diphoton masses, and hence smaller triphoton masses. Likewise, requiring larger p_T^γ leads to larger diphoton masses, and therefore larger triphoton masses. Despite these different shifts, we do not find clear improvement or worsening of the agreement between either evolution scheme and the full ME. In both (c) and (d), the full ME distribution sits inside both envelopes for $M(\gamma\gamma\gamma) \gtrsim 750$ GeV. However, as in the baseline case, the p_T^2-scheme again overestimates the full ME for $M(\gamma\gamma\gamma) \gtrsim 2$ TeV due to too large $\log(1-\xi)$ enhancements. This suggests that the specific dynamics of the hard scattering process may not have an appreciable impact the validity of the EWA, as one would hope.

4.5 Matrix Element Matching with Collinear W_T PDFs

As a final check of our implementation of EW boson PDFs into `mg5amc` and as a proof-of-concept demonstration of the potential capabilities, we briefly explore matrix element matching (MEM) with transverse weak boson PDFs. The idea behind MEM is that one can divide computations for complicated, many-leg final states that are susceptible to numerical instabilities, e.g., $\mu^+\mu^- \to \overline{\nu_\mu}\nu_\mu\gamma\gamma\gamma$, into two easier, more stable parts: (i) a ME with a smaller final-state multiplicity that represents a particular region of phase space of the original process, e.g., the process $\mu^+W^- \to \overline{\nu_\mu}\gamma\gamma\gamma$ with a f_{W^-/μ^-} PDF, which describes the collinear $\mu^- \to W^-\nu_\mu$ splitting; and (ii) the ME for the original process but where

the phase space for (i) is excluded, e.g., $\mu^+\mu^- \to \overline{\nu_\mu}\nu_\mu\gamma\gamma$ process with only wide-angle $\mu^- \to W^-\nu_\mu$ splittings. In principle, summing the two components should recover the full phase space for the original ME, up to power corrections that are formally small. The aim of this procedure is to efficiently describe regions of phase space that are otherwise difficult to model simultaneously due to instabilities associated with soft and/or collinear radiation. If MEM is successfully implemented, then the sum of (i) and (ii) should not only reproduce the original cross section, up to uncertainties, but also display an insensitivity to the (artificial) cutoff scale that divides the original process into regions (i) or (ii).

To sketch MEM conceptually for the case of matching collinear W_T (or Z_T) PDFs with full ME, we focus on the scattering process $e^+\mu^- \to \overline{\nu_e}\nu_\mu\gamma\gamma\gamma$. One can schematically divide the cross section of the process ($\sigma^{\text{Tot.}}$) into three disjoint pieces that describe different modes of $\mu^- \to W^-\nu_\mu$ splitting: (i) a collinear piece (σ^{C}), (ii) a quasi-collinear piece (σ^{QC}), and (iii) a hard piece (σ^{H}). Taking $p_T^{\nu_\mu}$ as the evolution variable, one can write:

$$\sigma^{\text{Tot.}} = \underbrace{\int_0^{\mu_f} dp_T^{\nu_\mu} \frac{d\sigma}{dp_T^{\nu_\mu}}}_{\sigma^{\text{C}}} + \underbrace{\int_{\mu_f}^{\Lambda} dp_T^{\nu_\mu} \frac{d\sigma}{dp_T^{\nu_\mu}}}_{\sigma^{\text{QC}}} + \underbrace{\int_{\Lambda}^{p_T^{\text{max}}} dp_T^{\nu_\mu} \frac{d\sigma}{dp_T^{\nu_\mu}}}_{\sigma^{\text{H}}}. \tag{4.10}$$

Here, $\mu_f \gg M_W$ is a factorization scale separating collinear and wide-angle $\mu^- \to W^-\nu_\mu$ splittings. The second cutoff Λ, which satisfies $\mu_f \lesssim \Lambda \ll p_T^{\text{max}}$, is some arbitrary scale such that collinear factorization remains a good approximation. (The introduction of Λ is simply for bookkeeping: it ensures σ^{QC} can be written in a convenient manner.) Finally, p_T^{max} is upper bound on p_T^ν allowed by momentum conservation and phase space cuts.

After integration over p_T^ν, both σ^{C} and σ^{QC} will scale like a collinear logarithm and power corrections, which we neglect (retain) in the (quasi-)collinear expression:

$$\sigma^{\text{C}} = \int_0^{\mu_f} dp_T^{\nu_\mu} \frac{d\sigma}{dp_T^{\nu_\mu}} \sim \log\frac{\mu_f^2}{M_W^2} + \underbrace{\mathcal{O}\left(\frac{\mu_f^2}{M_{WW}^2}\right)}_{\text{neglect}}, \tag{4.11}$$

$$\sigma^{\text{QC}} = \int_{\mu_f}^{\Lambda} dp_T^{\nu_\mu} \frac{d\sigma}{dp_T^{\nu_\mu}} \sim \log\frac{\Lambda^2}{\mu_f^2} + \underbrace{\mathcal{O}\left(\frac{\Lambda^2}{M_{WW}^2}\right)}_{\text{retain}}. \tag{4.12}$$

Combining the quasi-collinear and hard terms, one obtains the cross section ($\sigma^{\text{W}} \equiv \sigma^{\text{QC}} + \sigma^{\text{H}}$) for wide-angle $\mu^- \to W^-\nu_\mu$ splitting that is independent of Λ (since all Λ-dependent terms are kept). Moreover, were one to combine the leading logarithmic term of σ^{C} with σ^{W}, then the logarithmic dependence on μ_f would vanish identically. One would also recover the total cross section, up to the neglected power corrections. Explicitly, one finds

$$\sigma^{\text{Sum}} = \sigma^{\text{C}} + \sigma^{\text{W}} \sim \log\frac{\mu_f^2}{M_W^2} + \log\frac{\Lambda^2}{\mu_f^2} + \underbrace{\mathcal{O}\left(\frac{\Lambda^2}{M_{WW}^2}\right)}_{\text{retained}} + \sigma^{\text{H}} + \underbrace{\mathcal{O}\left(\frac{\mu_f^2}{M_{WW}^2}\right)}_{\text{neglected}}. \tag{4.13}$$

This indicates that μ_f can be interpreted in MEM also as the "matching scale" that matching collinear and wide-angle regions of phase space in an inclusive calculation.

To demonstrate that MEM is possible with transverse weak boson PDFs, we focus on $W^+W_T^- \to \gamma\gamma\gamma$ in $e^+\mu^-$ collisions and define the following disjoint regions of phase space:

Collinear Region : $e^+W_T^- \to \overline{\nu_e}\gamma\gamma\gamma$, for $p_T^{\nu_\mu} \leq \mu_f$ or $\sqrt{|q_{\mu\nu_\mu}^2|} \leq \mu_f$, (4.14)

Wide-Angle Region : $e^+\mu^- \to \overline{\nu_e}\nu_\mu\gamma\gamma\gamma$, for $p_T^{\nu_\mu} > \mu_f$ or $\sqrt{|q_{\mu\nu_\mu}^2|} > \mu_f$. (4.15)

When mediated by the EWA, we can identify $e^+W_T^-$ scattering in Eq. (4.14) as the collinear component of the inclusive $e^+\mu^- \to \overline{\nu_e}\nu_\mu\gamma\gamma\gamma$ process. Analogously, we can identify Eq. (4.15) as the wide-angle component of the inclusive $e^+\mu^- \to \overline{\nu_e}\nu_\mu\gamma\gamma\gamma$ process, when the appropriate phase space cut is applied to $p_T^{\nu_\mu}$ or the $\mu^- \to \nu_\mu$ momentum transfer $q_{\mu\nu_\mu}$.

To regulate poles associated with final-state photons, to avoid instabilities associated with collinear $e^+ \to W^+\overline{\nu_e}$ splittings, and to minimize the power corrections described in Sec. 4.2, we impose the following phase space restrictions on both Eqs. (4.14) and (4.15):

$$p_T^{\overline{\nu_e}} > 50 \text{ GeV}, \quad |\eta^{\overline{\nu_e}}| < 5, \quad p_T^{\gamma} > 50 \text{ GeV}, \quad |\eta^{\gamma}| < 3, \quad M(\gamma\gamma\gamma) > 1 \text{ or } 3 \text{ TeV}. \quad (4.16)$$

We treat the initial-state W_T^- using the appropriate PDF and consider when the PDF is defined in terms of (i) q^2 as given in Eq. (2.6), and (ii) p_T^2 as given in Eq. (2.7). Assuming that $f_{W_T^-}$ has been evaluated at a factorization scale μ_f, then for the case of evolution by q^2, we remove collinear and shallow-angle splittings in Eq. (4.15) by requiring that the norm of the $\mu^- \to \nu_\mu$ momentum transfer is larger than μ_f. Symbolically, this is given by

$$|q_{\mu\nu_\mu}^2| > \mu_f^2, \quad \text{where} \quad q_{\mu\nu_\mu}^2 \equiv (p_\mu - p_{\nu_\mu})^2. \quad (4.17)$$

This cut is implemented into `mg5amc` through the `dummy_cuts` function (file `dummy_fct.f`). For the case of evolution by p_T^2, we require that ν_μ satisfies the following restriction

$$p_T^{\nu_\mu} > \mu_f. \quad (4.18)$$

In Fig. 5, we show as a function of the factorization scale at $\sqrt{s} = 10$ TeV: (i) the total fiducial cross section for $e^+\mu^- \to \overline{\nu_e}\nu_\mu\gamma\gamma\gamma$ without restrictions on the $\mu^- \to W^-$ splitting (flat black curve labeled "Total"); (ii) the same but with restrictions on the $\mu^- \to W^-$ splitting (light purple curve labeled "Full ME + q cut" or "Full ME + p_T cut"); (iii) the fiducial cross section with its scale uncertainty band for $e^+W_T^- \to \overline{\nu_e}\gamma\gamma\gamma$ (light green band labeled "EWA"); and (iv) the sum of the restricted cross section and EWA with scale uncertainty (dark blue or red bands labeled "Sum"). More specifically, we show the dependence when $\mu_f = \sqrt{|q_{\mu\nu_\mu}^2|}$ in Fig. 5(a) and when $\mu_f = p_T^{\nu_\mu}$ in Fig. 5(b), at $M(\gamma\gamma\gamma) > 1$ TeV (solid lines) and $M(\gamma\gamma\gamma) > 3$ TeV (dashed lines). For both $M(\gamma\gamma\gamma)$ cuts we also show in the lower panel of each plot the ratio of the summed result, with its uncertainty band, to the total fiducial cross section without collinear restrictions. The f_{W_T} PDF and the restriction on $\mu^- \to W^-$ splittings are evaluated at the same value of μ_f. Uncertainty bands are obtained from three-point variation of μ_f in the EWA computations.

To establish a baseline, we start with Fig. 5(a) for evolution by $q_{\mu\nu_\mu}$ at $M(\gamma\gamma\gamma) > 1$ TeV. As one can anticipate, the fiducial cross sections with and without restrictions on
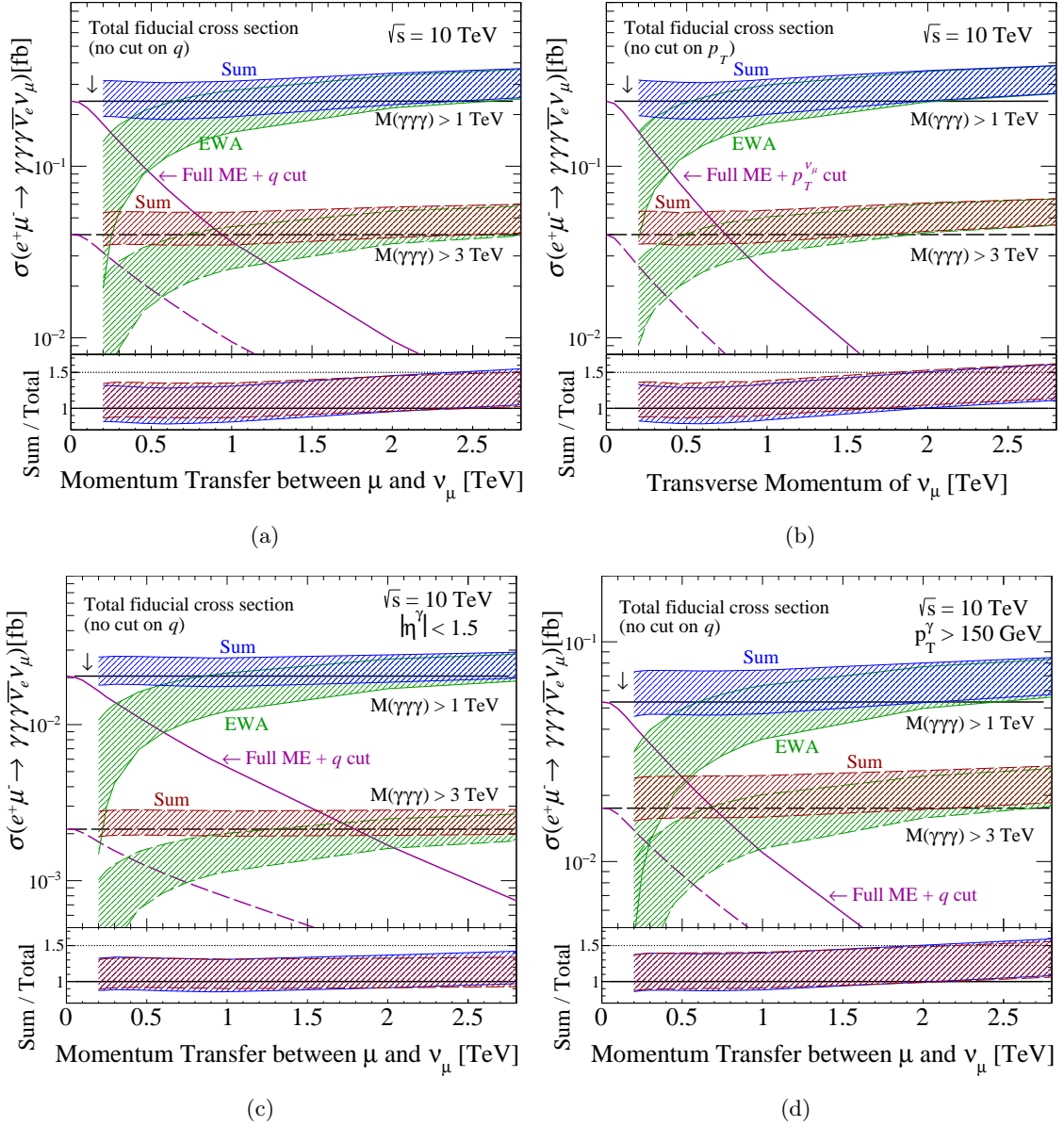
Figure 5. Matrix element matching in EVA for $e^+\mu^- \to \gamma\gamma\gamma\overline{\nu_e}\nu_\mu$ using the (a) q-scheme and (b) p_T-scheme, at $\sqrt{s} = 10$ TeV and assuming cuts of Eq. (4.16). (c,d) Same as (a) but for $|\eta^\gamma| < 1.5$ and $p_T^\gamma > 160$ GeV, respectively.

$\mu^- \to W^-$ splittings converge to the same rate, about $\sigma \sim 0.3$ fb, when effectively no cut is placed on the momentum transfer variable $|q^2_{\mu\nu_\mu}|$, i.e., when $\mu_f \to 0$ TeV. For increasing μ_f, we observe a logarithmic-like dependence for both the full ME with a $|q^2_{\mu\nu_\mu}|$ cut as well as the EWA result. In the former (latter), the rate decreases (increases) with increasing μ_f. We observe that the restricted rate and the EWA rate are comparable over the approximate range $\mu_f \in (200 \text{ GeV}, 500 \text{ GeV})$. For $\mu_f \gtrsim 1.5 \text{ TeV} - 2 \text{ TeV}$, we find that the full ME with a $|q^2_{\mu\nu_\mu}|$ cut becomes negligible, whereas the EWA result remains comparable to the total
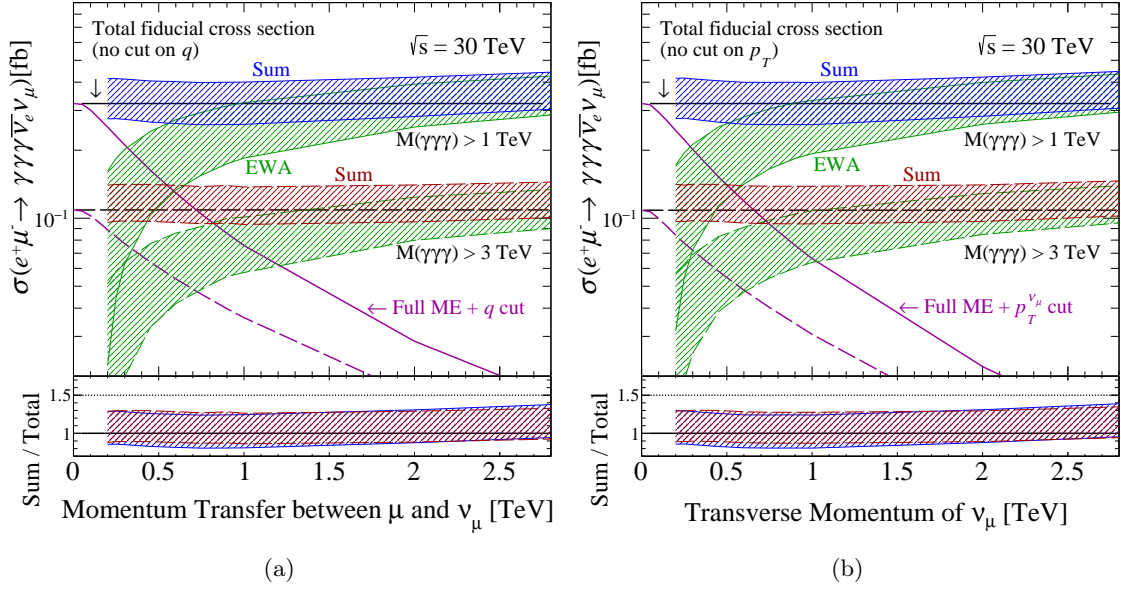
Figure 6. Same as Fig. 5 (a) and (b) but for $\sqrt{s} = 30$ TeV.

cross section. Over the range of μ_f investigated, we find that the EWA uncertainty band spans from about $\pm 75\%$ at $\mu_f \sim 200$ GeV to about $\pm 20\%$ at $\mu_f \gtrsim 2.5$ TeV; we caution, however, that the large change to the uncertainty band reflects the extreme range of μ_f we investigate. (Varying μ_f downward to $\mu_f = M_W$, for instance, would induce a -100% change since $f_{W_T} \sim \log \mu_f^2 / M_W^2$.) Importantly, when adding the restricted and EWA cross sections, we find that the sum reproduces the total fiducial cross section to within uncertainties and shows a strong insensitivity to the matching scale for $\mu_f < 2$ TeV. This indicates that MEM was achieved. While not shown, we report that the central value for the summed result consistently overestimates the total result by about $3\% - 7\%$ for $\mu_f = 200$ GeV $- 1$ TeV, and up to $20\% - 30\%$ for $\mu_f = 2$ TeV $- 3$ TeV. For the case of $M(\gamma\gamma) > 3$ TeV, we observe much of the same qualitative and quantitative behavior. The two notable differences are: (i) the obvious reduction in cross sections due to a more restrictive phase space cut, and (ii) a more stable summed result that features a central value (curve not shown) sitting nearly uniformly at about 10% above the total result for μ_f up to $\mu_f = 1$ TeV.

Much can be learned from this exercise. First is that the power corrections ($\Delta\sigma^{\mathrm{PC}}$) that distinguish the total fiducial cross section without t-channel cuts (σ^{Total}) from the summed result (σ^{Sum}), and which scale as $\Delta\sigma^{\mathrm{PC}} = \sigma^{\mathrm{Total}} - \sigma^{\mathrm{Sum}} \sim \mathcal{O}(\mu_f^2 / M_{WW}^2)$, are negative. (This is clear from the fact that the summed rate exceeds the total rate.) Second is that the W_T PDFs, and by extension the Z_T PDFs, work best when μ_f is set to lower values, e.g., $\mu_f \lesssim 1$ TeV when $\sqrt{s} = 10$ TeV. Naïvely, requiring relatively small μ_f may appear at odds with standard practices in pQCD, where μ_f are typically very high. However, in pQCD, one nearly always uses QCD PDFs that have been DGLAP-evolved; this has the effect of reducing the size of PDFs due to the RG running of $\alpha_s(\mu_r)$, thereby compensating for large collinear logarithms. The EW PDFs throughout this work are not evolved with EW-

DGLAP equations and necessitates smaller μ_f. The third observation is that for sufficiently large values of μ_f, the EWA rate begins to overestimate the total cross section. With little doubt, this can be attributed to a breakdown of the collinear approximation, which requires *collinear* initial-state splittings, i.e., $|q^2_{\mu\nu_\mu}| \sim p^{\nu 2}_T \ll M^2_{WW}$. Fourth is that the relative independence of the summed result on a matching scale indicates that the logarithmic dependence on μ_f in each component effectively cancel, in accordance with expectations. This serves as a highly non-trivial check of MEM with W_T/Z_T PDFs but also demonstrates the potential to support it in MC event generators. Finally, we note that the very similar and consistent size of the scale uncertainty bands across all channels can be attributed to the fact that we are working with fixed μ_f. For example: in (a), the scale variations are given by the ratio $\sigma(\mu_f = \zeta\mu_0)/\sigma(\mu_f = \mu_0) = \log(\zeta^2\mu_0^2/M_W^2)/\log(\mu_0^2/M_W^2)$ with $\zeta \in \{0.5, 1, 2\}$.

Focusing now on Fig. 5(b), we show the same quantities as in Fig. 5(a) but for evolution by $p^{\nu_\mu}_T$. Qualitatively, we see many similarities to the previous case, including that the summed result reproduces the total fiducial cross section to within uncertainties for $\mu \lesssim 1.5$ TeV. For larger μ_f, the difference between the summed and total results exceeds the uncertainty band of the summed result. We attribute this breakdown of MEM to a breakdown of the collinear approximation. The breakdown is more explicit in this case since one is varying $p^{\nu_\mu}_T$ and is influenced by the large-ξ enhancement discussed in Sec. 4.4.

To further explore the dependence on the kinematics of the hard $W^+W^-_T \to \gamma\gamma\gamma$ scattering process, we show in Figs. 5(c) and 5(d) the same quantities as in Figs. 5(a), but consider the more restrictive phase space cuts (c) $|\eta| < 1.5$ and (d) $p^\gamma_T > 150$ GeV. We again observe many of the same qualitative features, indicating some degree of independence from the hard scattering process. (Fewer changes would suggest more universal-like behavior.) One notable difference is that the tighter η^γ restriction helps extend the agreement between the summed and total results out to about $\mu_f \sim 3$ TeV. Slightly better agreement is also observed for the tighter p^γ_T requirement, but only until $\mu_f \sim 2.25$ TeV.

Finally in Fig. 6(a) and (b), we show the same quantities as in Fig. 5(a) and (b) but for $\sqrt{s} = 30$ TeV. As the qualitative and quantitative findings are highly comparable, little needs to be said. One noteworthy difference, however, is that higher collider energy further alleviates differences between the total and summed results, and extends the agreement to $\mu_f \gtrsim 3$ TeV. For all cases, the "summed" rate remains bigger than the "total" rate.

5   Polarized Vector Boson Scattering at Muon Colliders

A scenario in which the EVA promises to be highly relevant is that of a multi-TeV $\mu^+\mu^-$ collider. It is worth reiterating that when considering a generic multi-particle state $\mathcal{F}$, the VBF mechanism becomes an increasingly important, if not dominant, production vehicle in lepton collisions as the energy increases [41]. Given this, it is natural to consider muon colliders as effective weak boson colliders and take full advantage of the EVA in order to systematically organize and simplify the precision of scattering computations.

In this section, we explore the production of SM states generically parameterized by

$$\sum_{V_\lambda \in \{\gamma_\lambda, Z_\lambda, W^\pm_\lambda\}} V_{\lambda_A} V'_{\lambda_B} \to \mathcal{F}, \tag{5.1}$$

where $\mathcal{F}$ contains up to $n_\mathcal{F} = 4$ unpolarized states from the collection $\{H, t, \bar{t}, W^+, W^-, Z, \gamma\}$. All helicity polarizations are defined in the hard-scattering frame, i.e., the rest frame of $\mathcal{F}$. We consider collider configurations over the range $\sqrt{s} = 2 - 30$ TeV, and require final-state particles to obey the following kinematic and fiducial cuts:

$$M(\mathcal{F}) > 1 \text{ TeV}, \quad p_T^I > 50 \text{ GeV}, \quad |y^I| < 3, \quad \text{for} \quad I \in \{\mathcal{F}\}. \tag{5.2}$$

The invariant mass cut of 1 TeV on the system $\mathcal{F}$ is needed to ensure that power corrections of the form $(M_V^2/M^2(\mathcal{F}))$ are negligible, in accordance with findings of Sec. 4. We require moderate rapidities y to avoid t- and u-channel singularities and instabilities associated with final-state particles, as advocated by Ref. [25]; in the massless limit, the pseudorapidity value of $y \to \eta = 3$ corresponds to a polar angle of $\theta \approx 5.7°$. For all calculations involving $V_T V_T'$ or $V_T V_0'$ scattering, we set the central collinear factorization scale according to Eq. (4.5) and display three-point scale uncertainties. Scale uncertainties are unavailable for $V_0 V_0'$ scattering as the f_{V_0} PDFs do not depend on μ_f.

Our survey is organized in the following manner: We start in Sec. 5.1 with associated and multi-Higgs production. In Sec. 5.2, top quark and associated top quark production are discussed, followed by diboson and triboson production in Secs. 5.3 and 5.4, respectively.

5.1 Higgs production

We first consider Higgs production in $\mu^+\mu^-$ collisions and focus on the channels

$$V_{\lambda_A} V_{\lambda_B}' \quad \to \quad ZH, \quad W^+H, \quad \gamma H, \quad HH, \quad HHH, \quad \text{and} \quad HHHH. \tag{5.3}$$

In Fig. 7, we show as a function of collider energy [TeV] the fiducial cross section [fb], along with the associated three-point scale uncertainty band (from left to right in Eq. (5.3) corresponds the darkest to lightest color band), as mediated by (a) all initial-state EW boson polarizations, (b) longitudinal-longitudinal scattering, (c) transverse-longitudinal scattering, and (d) transverse-transverse scattering.

At the unpolarized level in Fig. 7(a), we observe a strong hierarchy between associated and multi-Higgs production, with VH production rates being more than an order of magnitude larger than HH production. More specifically, the ZH and W^+H rates span roughly $\sigma \sim 5 - 25$ fb for $\sqrt{s} \sim 5 - 30$ TeV, while HH production reaches about $\sigma \sim 0.5 - 1$ fb over the same range. By C-symmetry, the W^-H production rate is the same as W^+H, and therefore is not shown. The production of γH is universally smaller than ZH and WH by about a factor of $2 - 3$. Since ZH and γH are both mediated by W^+W^- scattering, the difference can be attributed to the difference in WWZ and $WW\gamma$ gauge couplings, where $\sigma_{ZH}/\sigma_{\gamma H} \sim (g_{ZWW}^2/g_{\gamma WW}^2) = (g \cos\theta_W/g \sin\theta_W)^2 \sim 3$. As the HH channel is also driven by W^+W^- fusion (recall that the $Z\mu\mu$ coupling is smaller than the $W\mu\nu_\mu$ coupling), it is tempting to also attribute the relative size of the VH and HH production rates to the coupling ratio $(g/\lambda)^2 \sim 27$. However, as shown in Fig. 7(b) and discussed in the next paragraph, this is not actually the case. All VH and HH channels are about 2-to-3 orders of magnitude larger than HHH production, which is yet another 2-to-3 orders of magnitude larger than $HHHH$ production. The (relatively) tiny triple and quadruple Higgs cross
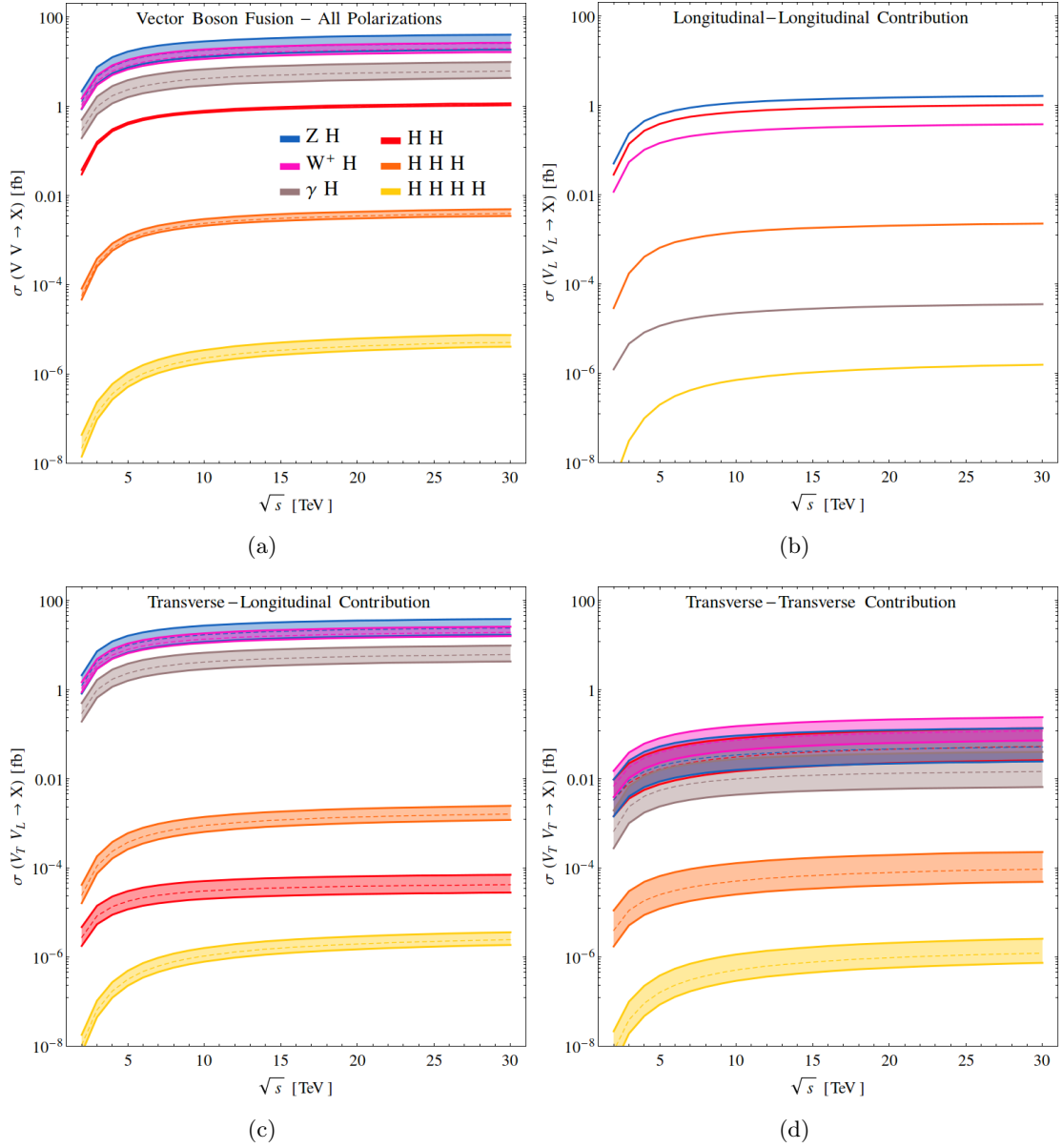
Figure 7. As a function of collider energy, the fiducial cross section and scale uncertainties under the EVA for associated Higgs and multi-Higgs production in $\mu^+\mu^-$ collisions from (a) all initial-state EW boson polarizations, (b) longitudinal-longitudinal scattering, (c) transverse-longitudinal scattering, and (d) transverse-transverse scattering.

sections follow from the compound effect of a small Higgs self-coupling and phase space suppression. For $\sqrt{s} \lesssim 5$ TeV, all rates are sensitive to small changes in collider energy due to threshold effects; above this scale, the energy dependence becomes milder.

As a function of polarization, one sees from Figs. 7(b-d) several notable characteristics. For instance: The VH channels are driven almost exclusively by $V_0 V_T'$ scattering, with a sub-leading component of $V_0 V_0'$ scattering. HH is dominated by $V_0 V_0'$ scattering, which accounts

	mg5amc syntax	$\sqrt{s} = 3$ TeV	σ [fb] $\sqrt{s} = 14$ TeV	$\sqrt{s} = 30$ TeV
$\sum V_{\lambda_A} V'_{\lambda_B} \to Z H$	vp vm > z h	$4.5 \cdot 10^0 \; {}^{+63\%}_{-31\%}$	$2.1 \cdot 10^1 \; {}^{+57\%}_{-28\%}$	$2.5 \cdot 10^1 \; {}^{+56\%}_{-28\%}$
$V_T V'_T \to Z H$	vp{T} vm{T} > z h	$9.0 \cdot 10^{-3} \; {}^{+181\%}_{-56\%}$	$4.0 \cdot 10^{-2} \; {}^{+169\%}_{-53\%}$	$5.1 \cdot 10^{-2} \; {}^{+165\%}_{-52\%}$
$V_0 V'_T \to Z H$	vp{0} vm{T} > z h	$4.3 \cdot 10^0 \; {}^{+66\%}_{-33\%}$	$1.9 \cdot 10^1 \; {}^{+61\%}_{-30\%}$	$2.4 \cdot 10^1 \; {}^{+59\%}_{-30\%}$
$V_0 V'_0 \to Z H$	vp{0} vm{0} > z h	$2.3 \cdot 10^{-1}$	$1.3 \cdot 10^0$	$1.6 \cdot 10^0$
$\sum V_{\lambda_A} V'_{\lambda_B} \to W^+ H$	vp vm > w+ h	$3.6 \cdot 10^0 \; {}^{+36\%}_{-18\%}$	$1.6 \cdot 10^1 \; {}^{+34\%}_{-17\%}$	$1.9 \cdot 10^1 \; {}^{+34\%}_{-17\%}$
$V_T V'_T \to W^+ H$	vp{T} vm{T} > w+ h	$1.8 \cdot 10^{-2} \; {}^{+113\%}_{-43\%}$	$8.8 \cdot 10^{-2} \; {}^{+105\%}_{-40\%}$	$1.2 \cdot 10^{-1} \; {}^{+102\%}_{-39\%}$
$V_0 V'_T \to W^+ H$	vp{0} vm{T} > w+ h	$3.5 \cdot 10^0 \; {}^{+36\%}_{-18\%}$	$1.5 \cdot 10^1 \; {}^{+35\%}_{-17\%}$	$1.9 \cdot 10^1 \; {}^{+34\%}_{-17\%}$
$V_0 V'_0 \to W^+ H$	vp{0} vm{0} > w+ h	$5.3 \cdot 10^{-2}$	$3.0 \cdot 10^{-1}$	$3.7 \cdot 10^{-1}$
$\sum V_{\lambda_A} V'_{\lambda_B} \to \gamma H$	vp vm > a h	$9.8 \cdot 10^{-1} \; {}^{+67\%}_{-33\%}$	$4.8 \cdot 10^0 \; {}^{+61\%}_{-30\%}$	$6.0 \cdot 10^0 \; {}^{+60\%}_{-30\%}$
$V_T V'_T \to \gamma H$	vp{T} vm{T} > a h	$2.3 \cdot 10^{-3} \; {}^{+188\%}_{-57\%}$	$1.1 \cdot 10^{-2} \; {}^{+178\%}_{-55\%}$	$1.4 \cdot 10^{-2} \; {}^{+176\%}_{-55\%}$
$V_0 V'_T \to \gamma H$	vp{0} vm{T} > a h	$9.8 \cdot 10^{-1} \; {}^{+67\%}_{-33\%}$	$4.8 \cdot 10^0 \; {}^{+61\%}_{-30\%}$	$6.0 \cdot 10^0 \; {}^{+59\%}_{-30\%}$
$V_0 V'_0 \to \gamma H$	vp{0} vm{0} > a h	$4.5 \cdot 10^{-6}$	$2.7 \cdot 10^{-5}$	$3.5 \cdot 10^{-5}$
$\sum V_{\lambda_A} V'_{\lambda_B} \to HH$	vp vm >h h	$1.4 \cdot 10^{-1} \; {}^{+10\%}_{-3\%}$	$8.5 \cdot 10^{-1} \; {}^{+7\%}_{-2\%}$	$1.1 \cdot 10^0 \; {}^{+8\%}_{-2\%}$
$V_T V'_T \to HH$	vp{T} vm{T} > h h	$7.9 \cdot 10^{-3} \; {}^{+177\%}_{-55\%}$	$3.8 \cdot 10^{-2} \; {}^{+162\%}_{-52\%}$	$5.2 \cdot 10^{-2} \; {}^{+157\%}_{-51\%}$
$V_0 V'_T \to HH$	vp{0} vm{T} > h h	$8.2 \cdot 10^{-6} \; {}^{+69\%}_{-35\%}$	$3.4 \cdot 10^{-5} \; {}^{+67\%}_{-38\%}$	$4.1 \cdot 10^{-5} \; {}^{+67\%}_{-33\%}$
$V_0 V'_0 \to HH$	vp{0} vm{0} > h h	$1.3 \cdot 10^{-1}$	$8.2 \cdot 10^{-1}$	$1.0 \cdot 10^0$
$\sum V_{\lambda_A} V'_{\lambda_B} \to HHH$	vp vm > h h h	$2.9 \cdot 10^{-4} \; {}^{+30\%}_{-14\%}$	$2.9 \cdot 10^{-3} \; {}^{+24\%}_{-12\%}$	$3.9 \cdot 10^{-3} \; {}^{+25\%}_{-12\%}$
$V_T V'_T \to HHH$	vp{T} vm{T} > h h h	$1.1 \cdot 10^{-5} \; {}^{+170\%}_{-54\%}$	$6.4 \cdot 10^{-5} \; {}^{+150\%}_{-49\%}$	$9.2 \cdot 10^{-5} \; {}^{+144\%}_{-48\%}$
$V_0 V'_T \to HHH$	vp{0} vm{T} > h h h	$1.1 \cdot 10^{-4} \; {}^{+65\%}_{-32\%}$	$1.1 \cdot 10^{-3} \; {}^{+55\%}_{-27\%}$	$1.6 \cdot 10^{-3} \; {}^{+53\%}_{-26\%}$
$V_0 V'_0 \to HHH$	vp{0} vm{0} > h h h	$1.7 \cdot 10^{-4}$	$1.7 \cdot 10^{-3}$	$2.3 \cdot 10^{-3}$
$\sum V_{\lambda_A} V'_{\lambda_B} \to HHHH$	vp vm > h h h h	$1.3 \cdot 10^{-7} \; {}^{+75\%}_{-30\%}$	$3.2 \cdot 10^{-6} \; {}^{+49\%}_{-21\%}$	$5.0 \cdot 10^{-6} \; {}^{+46\%}_{-20\%}$
$V_T V'_T \to HHHH$	vp{T} vm{T} > h h h h	$3.8 \cdot 10^{-8} \; {}^{+156\%}_{-51\%}$	$7.1 \cdot 10^{-7} \; {}^{+118\%}_{-42\%}$	$1.2 \cdot 10^{-6} \; {}^{+110\%}_{-39\%}$
$V_0 V'_T \to HHHH$	vp{0} vm{T} > h h h h	$6.4 \cdot 10^{-8} \; {}^{+62\%}_{-31\%}$	$1.5 \cdot 10^{-6} \; {}^{+49\%}_{-25\%}$	$2.4 \cdot 10^{-6} \; {}^{+47\%}_{-24\%}$
$V_0 V'_0 \to HHHH$	vp{0} vm{0} > h h h h	$3.0 \cdot 10^{-8}$	$9.8 \cdot 10^{-7}$	$1.5 \cdot 10^{-6}$

Table 4. Fiducial cross sections with scale uncertainties for associated Higgs and multi-Higgs production in $\mu^+\mu^-$ collisions through $V_{\lambda_A} V'_{\lambda_B}$ scattering, where $V_\lambda \in \{\gamma_\lambda, Z_\lambda, W^\pm_\lambda\}$, under the EVA for polarization-summed and polarized initial states, at $\sqrt{s} = 3$, 14, and 30 TeV. All helicity polarizations are defined in the hard-scattering frame. Phase space cuts are summarized in Eq. (5.2). Also shown is the mg5amc syntax for modeling the process assuming the multi-particle definitions "vp=z,w+,a" and "vm=z,w-,a." The configuration $(0, T)$ implies a sum over both $(0, T)$ and $(T, 0)$, and uses the syntax generate vp{0} vm{T} > ...; add process vp{T} vm{0} > ...

for the smaller dependence on factorization scales when summing over all polarizations, but also contains a sub-leading $V_T V'_T$ contribution. Notably, ZH, W^+H, and HH all have comparable $V_0 V'_0$ scattering rates, which is in line with the Goldstone Equivalence Theorem. This indicates that the σ_{VH}-σ_{HH} hierarchy observed in Figs. 7(a) is actually due to the compound effect of logarithmic enhancements in f_{V_T} PDFs and helicity configurations allowed by angular momentum conservation, e.g., $V_T V'_0 \to HH$ is helicity suppressed. We report that HHH production has significant and comparable contributions from $V_0 V'_0$ and $V_T V'_0$ scattering, but only a marginal contribution from $V_T V'_T$. Interestingly, $HHHH$ receives comparable contributions from all polarization configurations. As one can expect, production from $V_T V_T$ scattering exhibits larger scale uncertainties than in $V_T V_0$ scattering. For each unpolarized and polarized scattering configuration, we document in Table 4 the
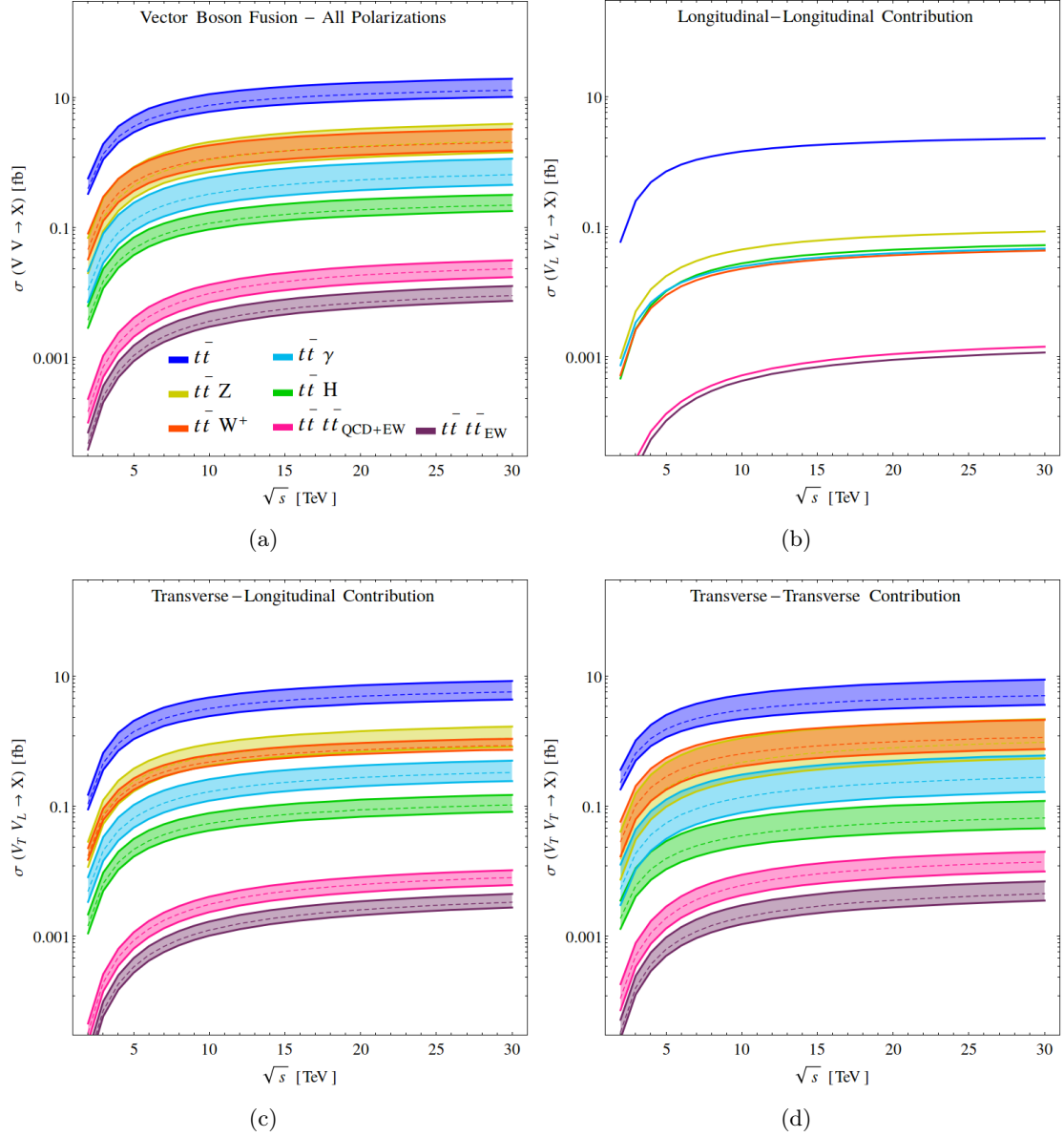
Figure 8. Same as Fig. 7 but for $t\bar{t}$ pair production and $t\bar{t} + X$ associated production.

relevant `mg5amc` process syntax that enables our computation and the fiducial cross section [fb] with its scale uncertainty [%], for representative collider energies.

5.2 Top and associated top production

Next, we address $t\bar{t}$ pair and associated $t\bar{t}$ production, focusing on the channels

$$V_{\lambda_A} V'_{\lambda_B} \quad \rightarrow \quad t\bar{t}, \quad t\bar{t}Z, \quad t\bar{t}W^+, \quad t\bar{t}\gamma, \quad t\bar{t}H, \quad \text{and} \quad t\bar{t}t\bar{t}. \tag{5.4}$$

For the $t\bar{t}t\bar{t}$ process, we consider both the production though QCD and EW couplings $(t\bar{t}t\bar{t}_{\text{QCD+EW}})$ as well as purely through EW couplings $(t\bar{t}t\bar{t}_{\text{EW}})$. In Fig. 8 we present

	mg5amc syntax	σ [fb]		
		$\sqrt{s} = 3$ TeV	$\sqrt{s} = 14$ TeV	$\sqrt{s} = 30$ TeV
$\sum V_{\lambda_A} V'_{\lambda_B} \to t\bar{t}$	vp vm > t t~	$1.3 \cdot 10^0 \; ^{+42\%}_{-18\%}$	$9.4 \cdot 10^0 \; ^{+49\%}_{-21\%}$	$1.3 \cdot 10^1 \; ^{+50\%}_{-21\%}$
$V_T V'_T \to t\bar{t}$	vp{T} vm{T} > t t~	$6.4 \cdot 10^{-1} \; ^{+58\%}_{-23\%}$	$3.7 \cdot 10^0 \; ^{+73\%}_{-27\%}$	$5.0 \cdot 10^0 \; ^{+76\%}_{-28\%}$
$V_0 V'_T \to t\bar{t}$	vp{0} vm{T} > t t~	$4.6 \cdot 10^{-1} \; ^{+43\%}_{-22\%}$	$4.0 \cdot 10^0 \; ^{+48\%}_{-24\%}$	$5.7 \cdot 10^0 \; ^{+47\%}_{-24\%}$
$V_0 V'_0 \to t\bar{t}$	vp{0} vm{0} > t t~	$2.5 \cdot 10^{-1}$	$1.7 \cdot 10^0$	$2.3 \cdot 10^0$
$\sum V_{\lambda_A} V'_{\lambda_B} \to t\bar{t} Z$	vp vm > t t~ z	$1.4 \cdot 10^{-1} \; ^{+99\%}_{-38\%}$	$1.4 \cdot 10^0 \; ^{+86\%}_{-34\%}$	$2.1 \cdot 10^0 \; ^{+84\%}_{-33\%}$
$V_T V'_T \to t\bar{t} Z$	vp{T} vm{T} > t t~ z	$6.0 \cdot 10^{-2} \; ^{+155\%}_{-50\%}$	$6.2 \cdot 10^{-1} \; ^{+134\%}_{-45\%}$	$9.5 \cdot 10^{-1} \; ^{+127\%}_{-43\%}$
$V_0 V'_T \to t\bar{t} Z$	vp{0} vm{T} > t t~ z	$7.6 \cdot 10^{-2} \; ^{+62\%}_{-31\%}$	$7.5 \cdot 10^{-1} \; ^{+54\%}_{-27\%}$	$1.1 \cdot 10^0 \; ^{+52\%}_{-26\%}$
$V_0 V'_0 \to t\bar{t} Z$	vp{0} vm{0} > t t~ z	$4.9 \cdot 10^{-3}$	$5.8 \cdot 10^{-2}$	$8.3 \cdot 10^{-2}$
$\sum V_{\lambda_A} V'_{\lambda_B} \to t\bar{t} W^+$	vp vm > t t~ w+	$1.7 \cdot 10^{-1} \; ^{+68\%}_{-28\%}$	$1.4 \cdot 10^0 \; ^{+61\%}_{-25\%}$	$2.0 \cdot 10^0 \; ^{+59\%}_{-24\%}$
$V_T V'_T \to t\bar{t} W^+$	vp{T} vm{T} > t t~ w+	$1.0 \cdot 10^{-1} \; ^{+99\%}_{-39\%}$	$8.0 \cdot 10^{-1} \; ^{+88\%}_{-35\%}$	$1.1 \cdot 10^0 \; ^{+85\%}_{-34\%}$
$V_0 V'_T \to t\bar{t} W^+$	vp{0} vm{T} > t t~ w+	$7.0 \cdot 10^{-2} \; ^{+29\%}_{-14\%}$	$6.0 \cdot 10^{-1} \; ^{+28\%}_{-14\%}$	$8.4 \cdot 10^{-1} \; ^{+27\%}_{-14\%}$
$V_0 V'_0 \to t\bar{t} W^+$	vp{0} vm{0} > t t~ w+	$2.6 \cdot 10^{-3}$	$2.9 \cdot 10^{-2}$	$4.2 \cdot 10^{-2}$
$\sum V_{\lambda_A} V'_{\lambda_B} \to \to t\bar{t} \gamma$	vp vm > t t~ a	$4.2 \cdot 10^{-2} \; ^{+88\%}_{-34\%}$	$4.3 \cdot 10^{-1} \; ^{+78\%}_{-31\%}$	$6.4 \cdot 10^{-1} \; ^{+76\%}_{-30\%}$
$V_T V'_T \to t\bar{t} \gamma$	vp{T} vm{T} > t t~ a	$1.9 \cdot 10^{-2} \; ^{+133\%}_{-43\%}$	$1.8 \cdot 10^{-1} \; ^{+122\%}_{-42\%}$	$2.7 \cdot 10^{-1} \; ^{+117\%}_{-40\%}$
$V_0 V'_T \to t\bar{t} \gamma$	vp{0} vm{T} > t t~ a	$2.0 \cdot 10^{-2} \; ^{+61\%}_{-31\%}$	$2.2 \cdot 10^{-1} \; ^{+54\%}_{-27\%}$	$3.2 \cdot 10^{-1} \; ^{+52\%}_{-26\%}$
$V_0 V'_0 \to t\bar{t} \gamma$	vp{0} vm{0} > t t~ a	$3.3 \cdot 10^{-3}$	$3.1 \cdot 10^{-2}$	$4.5 \cdot 10^{-2}$
$\sum V_{\lambda_A} V'_{\lambda_B} \to t\bar{t} H$	vp vm > t t~ h	$1.5 \cdot 10^{-2} \; ^{+55\%}_{-23\%}$	$1.5 \cdot 10^{-1} \; ^{+45\%}_{-19\%}$	$2.2 \cdot 10^{-1} \; ^{+44\%}_{-19\%}$
$V_T V'_T \to t\bar{t} H$	vp{T} vm{T} > t t~ h	$5.9 \cdot 10^{-3} \; ^{+86\%}_{-31\%}$	$4.5 \cdot 10^{-2} \; ^{+85\%}_{-31\%}$	$6.5 \cdot 10^{-2} \; ^{+83\%}_{-31\%}$
$V_0 V'_T \to t\bar{t} H$	vp{0} vm{T} > t t~ h	$6.4 \cdot 10^{-3} \; ^{+47\%}_{-23\%}$	$7.0 \cdot 10^{-2} \; ^{+44\%}_{-22\%}$	$1.0 \cdot 10^{-1} \; ^{+43\%}_{-21\%}$
$V_0 V'_0 \to t\bar{t} H$	vp{0} vm{0} > t t~ h	$2.6 \cdot 10^{-3}$	$3.5 \cdot 10^{-2}$	$5.1 \cdot 10^{-2}$
$\sum V_{\lambda_A} V'_{\lambda_B} \to t\bar{t} t\bar{t}\,_{\text{QCD+EW}}$	vp{T} vm{T} > t t~ t t~	$7.1 \cdot 10^{-4} \; ^{+47\%}_{-31\%}$	$1.4 \cdot 10^{-2} \; ^{+36\%}_{-26\%}$	$2.3 \cdot 10^{-2} \; ^{+35\%}_{-26\%}$
$V_T V'_T \to t\bar{t} t\bar{t}\,_{\text{QCD+EW}}$	vp{T} vm{T} > t t~ t t~	$4.9 \cdot 10^{-4} \; ^{+57\%}_{-33\%}$	$8.4 \cdot 10^{-3} \; ^{+45\%}_{-29\%}$	$1.4 \cdot 10^{-2} \; ^{+43\%}_{-29\%}$
$V_0 V'_T \to t\bar{t} t\bar{t}\,_{\text{QCD+EW}}$	vp{0} vm{T} > t t~ t t~	$1.9 \cdot 10^{-4} \; ^{+35\%}_{-27\%}$	$4.5 \cdot 10^{-3} \; ^{+30\%}_{-24\%}$	$7.9 \cdot 10^{-3} \; ^{+30\%}_{-23\%}$
$V_0 V'_0 \to t\bar{t} t\bar{t}\,_{\text{QCD+EW}}$	vp{0} vm{0} > t t~ t t~	$2.6 \cdot 10^{-5}$	$7.7 \cdot 10^{-4}$	$1.4 \cdot 10^{-3}$
$\sum V_{\lambda_A} V'_{\lambda_B} \to t\bar{t} t\bar{t}\,_{\text{EW}}$	vp{T} vm{T} > t t~ t t~ QCD=0	$2.5 \cdot 10^{-4} \; ^{+45\%}_{-19\%}$	$5.1 \cdot 10^{-3} \; ^{+41\%}_{-18\%}$	$8.8 \cdot 10^{-3} \; ^{+40\%}_{-17\%}$
$V_T V'_T \to t\bar{t} t\bar{t}\,_{\text{EW}}$	vp{T} vm{T} > t t~ t t~ QCD=0	$1.6 \cdot 10^{-4} \; ^{+53\%}_{-21\%}$	$2.7 \cdot 10^{-3} \; ^{+53\%}_{-21\%}$	$4.4 \cdot 10^{-3} \; ^{+54\%}_{-22\%}$
$V_0 V'_T \to t\bar{t} t\bar{t}\,_{\text{EW}}$	vp{0} vm{T} > t t~ t t~ QCD=0	$7.1 \cdot 10^{-5} \; ^{+38\%}_{-19\%}$	$1.8 \cdot 10^{-3} \; ^{+35\%}_{-18\%}$	$3.3 \cdot 10^{-3} \; ^{+34\%}_{-17\%}$
$V_0 V'_0 \to t\bar{t} t\bar{t}\,_{\text{EW}}$	vp{0} vm{0} > t t~ t t~ QCD=0	$1.8 \cdot 10^{-5}$	$6.4 \cdot 10^{-4}$	$1.1 \cdot 10^{-3}$

Table 5. Same as Table 4 but for $t\bar{t}$ pair production and $t\bar{t}$ associated production.

the unpolarized and helicity-polarized cross sections as a function of collider energy in the same manner as in Fig. 7. An immediate observation is that for all processes each of the polarization combinations of initial-state EW bosons $V_{\lambda_A} V'_{\lambda_B}$ give a comparable contribution to the unpolarized process. This is in contrast to associated and multi-Higgs production in Sec. 5.1, where typically one particular $V_{\lambda_A} V'_{\lambda_B}$ configuration drives the total process. For all polarized and unpolarized cases, $t\bar{t}$ production exhibits the largest cross sections, whereas pure EW production of $t\bar{t}t\bar{t}$ exhibits the lowest rates. The difference between the channels is about three orders of magnitude. Mixed QCD+EW production of $t\bar{t}t\bar{t}$ sits just above the pure EW rate; notably, the difference between the two $t\bar{t}t\bar{t}$ processes is larger than their uncertainty bands. All $t\bar{t}V$ and $t\bar{t}H$ cross sections are sandwiched between the two processes and exhibit a rate hierarchy that is in line with naïve EW coupling enhancement/suppression. While the hierarchy is independent of collider energy, some reordering can be observed when individual helicity configurations are considered.

Focusing first on $V_0 V'_0$ scattering in Fig. 8(b), we find that the $t\bar{t}V$ and $t\bar{t}H$ channels all have highly comparable rates. This is essentially due to all these channels being driven by

either $W_0^+ W_0^-$ or $W_0^+ Z_0$ scattering. Hence, appreciable differences in rate are due to differences in coupling constants. As there is no γ_0 PDF, there is no $\log(\mu_f^2/m_\mu^2)$ enhancement like there is in other polarization configurations.

More explicitly, for $V_T V_0'$ scattering in Fig. 8(c) and $V_T V_T'$ scattering in Fig. 8(d), we find appreciably larger cross sections than for pure $V_0 V_0'$ scattering. Again, we attribute this to the opening of $\gamma_T V_\lambda$ scattering and logarithmic enhancements in transverse PDFs. Interestingly, we find that the hierarchy of $t\bar{t}\gamma/Z/W^+/H$ depends on the precise polarization configuration of initial-state EW bosons. For example: $t\bar{t}Z$ has a larger rate than $t\bar{t}W^+$ in $V_T V_0'$ scattering, but the opposite is true in $V_T V_T'$ scattering. Both configurations lead to larger rates than for $t\bar{t}\gamma$, which is not the case for $V_0 V_0'$ scattering.

We summarize these results for representative $\sqrt{s}$ in Table 5.

5.3 Diboson production

We now turn to diboson production in EVA. In Fig. 9, we plot again the (a) polarization-summed and (b-d) polarized production cross section with their respective factorization scale uncertainties, as a function of collider energy for the following six processes

$$V_{\lambda_A} V_{\lambda_B}' \quad \to \quad W^+ W^-, \quad ZZ, \quad ZW^+, \quad \gamma Z, \quad \gamma W^+, \quad \text{and} \quad \gamma\gamma. \tag{5.5}$$

As in previous cases, there are several global features that one can infer. Foremost is that unlike Higgs (Fig. 7) and top quark (Fig. 8) processes, we find a clear hierarchy among initial-state EW boson polarizations. More specifically, we find that $V_T V_T'$ scattering is categorically the dominant production vehicle of EW boson pairs. The role of $V_T V_0'$ scattering is about one-to-two orders of magnitude smaller than $V_T V_T'$ scattering, and rate of $V_0 V_0'$ scattering is yet another decade smaller. As of $V_0 V_0'$ scattering is negligible, unpolarized diboson cross sections in the EVA exhibit a relatively larger scale uncertainty than Higgs and top quark production, which feature a larger dependence on $V_0 V_0'$ scattering.

Another consequence of the strong polarization dependence is that the hierarchy of fiducial cross sections shown in the unpolarized case largely mirrors the hierarchy in $V_T V_T'$ scattering. That said, we find that this same hierarchy is mostly preserved with other helicity configurations. This suggests a larger dependence on available partonic channels and gauge couplings than logarithmic enhancements from soft and collinear regions of phase space. For example: the $W^+ W^-$ production cross section dominates for all helicity configurations but also can be produced via the most number of partonic configurations, i.e., $W_{\lambda_A}^+ W_{\lambda_B}^-, Z_{\lambda_A} Z_{\lambda_B}, Z_{\lambda_A} \gamma_{\lambda_B}$, and $\gamma_{\lambda_A} \gamma_{\lambda_B}$ fusion. The reverse can be said for $\gamma\gamma$ and γW^+ production. These processes exhibit the lowest diboson cross sections but can only proceed through one or two partonic channels, namely $W_{\lambda_A}^+ W_{\lambda_B}^-$ and $W_{\lambda_A}^+ \gamma_{\lambda_B}$. We also note that helicity suppression stemming from angular momentum conservation also plays a role in this hierarchy. For example: while $W_0^+ Z_0 \to W_0^+ \gamma_T$ exhibits a larger longitudinal polarization enhancement than $W_0^+ Z_0 \to W_T^+ \gamma_T$, the former (later) is disfavored (favored) since it must proceed through a high-wave (low-wave) angular momentum configuration.

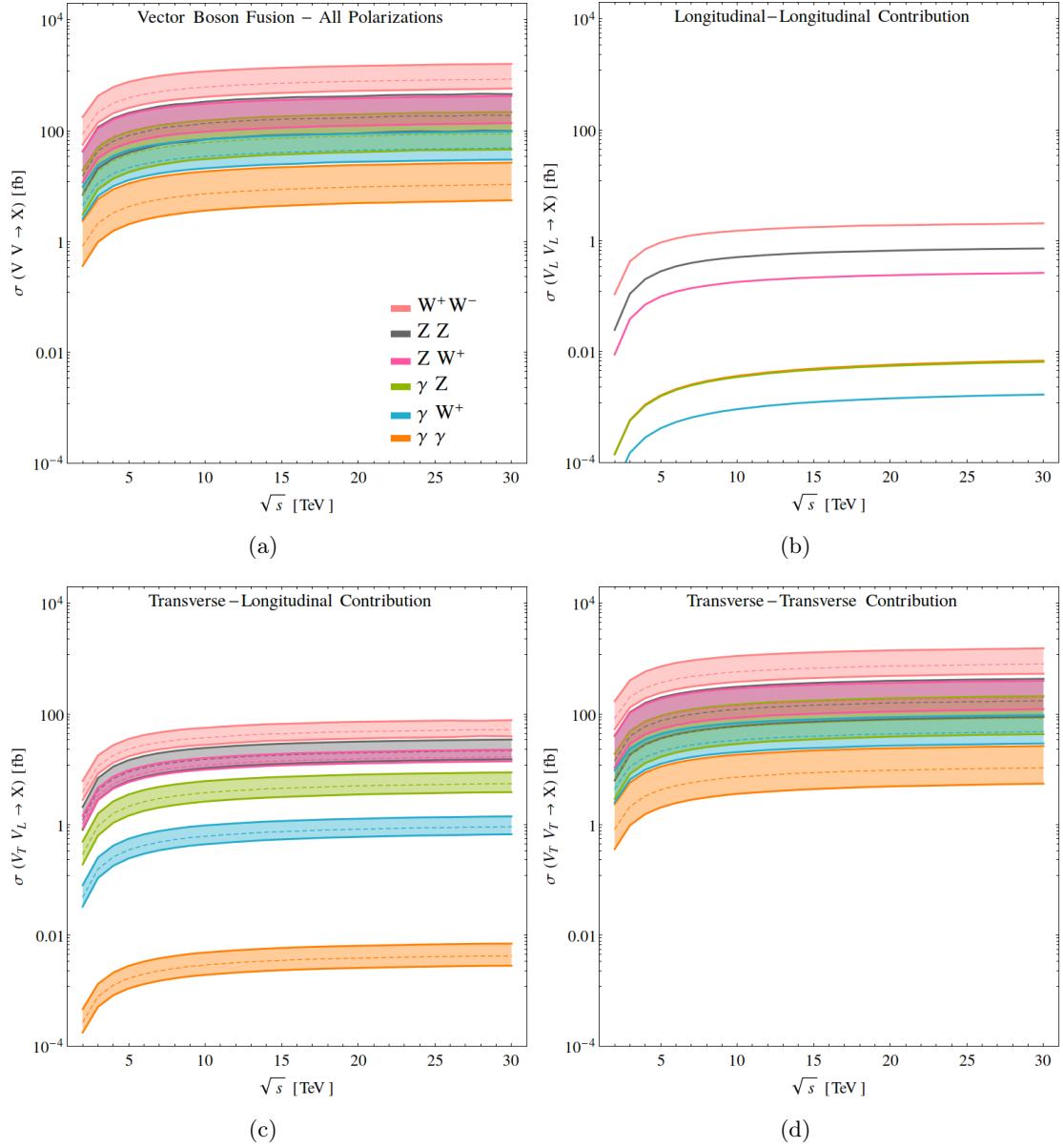We summarize these results for representative $\sqrt{s}$ in Table 6.

Figure 9. Same as Fig. 7 but for VV production.

5.4 Triboson production

In the final part of our survey, we show in Fig. 10 the fiducial cross sections for triboson production (a) after summing over all initial-state helicity polarizations and (b-d) for individual (λ_A, λ_B) configurations. For conciseness, we focus on the representative channels

$$V_{\lambda_A} V'_{\lambda_B} \to ZW^+W^-, \quad \gamma W^+W^-, \quad ZZZ, \quad ZZW^+, \quad \gamma ZW^+, \quad \text{and} \quad \gamma\gamma W^+. \quad (5.6)$$

An immediate observation we can make is the qualitative similarities between triboson and diboson production in Fig. 9. In particular, we find that triboson production is driven by

	mg5amc syntax	$\sqrt{s} = 3$ TeV	$\sqrt{s} = 14$ TeV	$\sqrt{s} = 30$ TeV
			σ [fb]	
$\sum V_{\lambda_A} V'_{\lambda_B} \to W^+ W^-$	vp vm > w+ w-	$2.2 \cdot 10^2 \; ^{+98\%}_{-35\%}$	$7.0 \cdot 10^2 \; ^{+91\%}_{-33\%}$	$8.6 \cdot 10^2 \; ^{+88\%}_{-32\%}$
$V_T V'_T \to W^+ W^-$	vp{T} vm{T} > w+ w-	$2.0 \cdot 10^2 \; ^{+99\%}_{-35\%}$	$6.6 \cdot 10^2 \; ^{+93\%}_{-34\%}$	$8.0 \cdot 10^2 \; ^{+92\%}_{-33\%}$
$V_0 V'_T \to W^+ W^-$	vp{0} vm{T} > w+ w-	$1.2 \cdot 10^1 \; ^{+54\%}_{-27\%}$	$4.4 \cdot 10^1 \; ^{+50\%}_{-25\%}$	$5.2 \cdot 10^1 \; ^{+49\%}_{-24\%}$
$V_0 V'_0 \to W^+ W^-$	vp{0} vm{0} > w+ w-	$4.2 \cdot 10^{-1}$	$1.7 \cdot 10^0$	$2.0 \cdot 10^0$
$\sum V_{\lambda_A} V'_{\lambda_B} \to W^+ Z$	vp vm > w+ z	$5.3 \cdot 10^1 \; ^{+105\%}_{-40\%}$	$1.8 \cdot 10^2 \; ^{+97\%}_{-37\%}$	$2.2 \cdot 10^2 \; ^{+95\%}_{-37\%}$
$V_T V'_T \to W^+ Z$	vp{T} vm{T} > w+ z	$5.0 \cdot 10^1 \; ^{+111\%}_{-42\%}$	$1.6 \cdot 10^2 \; ^{+103\%}_{-39\%}$	$2.0 \cdot 10^2 \; ^{+100\%}_{-38\%}$
$V_0 V'_T \to W^+ Z$	vp{0} vm{T} > w+ z	$3.4 \cdot 10^0 \; ^{+36\%}_{-18\%}$	$1.4 \cdot 10^1 \; ^{+34\%}_{-17\%}$	$1.7 \cdot 10^1 \; ^{+34\%}_{-17\%}$
$V_0 V'_0 \to W^+ Z$	vp{0} vm{0} > w+ z	$3.9 \cdot 10^{-2}$	$2.1 \cdot 10^{-1}$	$2.6 \cdot 10^{-1}$
$\sum V_{\lambda_A} V'_{\lambda_B} \to ZZ$	vp vm > z z	$4.4 \cdot 10^1 \; ^{+164\%}_{-52\%}$	$1.6 \cdot 10^2 \; ^{+144\%}_{-48\%}$	$1.9 \cdot 10^2 \; ^{+143\%}_{-48\%}$
$V_T V'_T \to ZZ$	vp{T} vm{T} > z z	$4.0 \cdot 10^1 \; ^{+171\%}_{-54\%}$	$1.4 \cdot 10^2 \; ^{+153\%}_{-50\%}$	$1.7 \cdot 10^2 \; ^{+150\%}_{-49\%}$
$V_0 V'_T \to ZZ$	vp{0} vm{T} > z z	$4.2 \cdot 10^0 \; ^{+66\%}_{-33\%}$	$1.8 \cdot 10^1 \; ^{+61\%}_{-30\%}$	$2.2 \cdot 10^1 \; ^{+60\%}_{-30\%}$
$V_0 V'_0 \to ZZ$	vp{0} vm{0} > z z	$1.1 \cdot 10^{-1}$	$6.0 \cdot 10^{-1}$	$7.2 \cdot 10^{-1}$
$\sum V_{\lambda_A} V'_{\lambda_B} \to \gamma Z$	vp vm > a z	$1.9 \cdot 10^1 \; ^{+169\%}_{-53\%}$	$7.1 \cdot 10^1 \; ^{+149\%}_{-49\%}$	$8.8 \cdot 10^1 \; ^{+145\%}_{-48\%}$
$V_T V'_T \to \gamma Z$	vp{T} vm{T} > a z	$1.8 \cdot 10^1 \; ^{+172\%}_{-54\%}$	$6.8 \cdot 10^1 \; ^{+153\%}_{-50\%}$	$8.4 \cdot 10^1 \; ^{+149\%}_{-49\%}$
$V_0 V'_T \to \gamma Z$	vp{0} vm{T} > a z	$9.5 \cdot 10^{-1} \; ^{+67\%}_{-33\%}$	$4.4 \cdot 10^0 \; ^{+61\%}_{-30\%}$	$5.5 \cdot 10^0 \; ^{+60\%}_{-30\%}$
$V_0 V'_0 \to \gamma Z$	vp{0} vm{0} > a z	$5.6 \cdot 10^{-4}$	$4.5 \cdot 10^{-3}$	$6.5 \cdot 10^{-3}$
$\sum V_{\lambda_A} V'_{\lambda_B} \to \gamma W^+$	vp vm > a w+	$1.1 \cdot 10^1 \; ^{+111\%}_{-42\%}$	$4.0 \cdot 10^1 \; ^{+101\%}_{-39\%}$	$4.9 \cdot 10^1 \; ^{+99\%}_{-38\%}$
$V_T V'_T \to \gamma W^+$	vp{T} vm{T} > a w+	$1.1 \cdot 10^1 \; ^{+111\%}_{-42\%}$	$3.9 \cdot 10^1 \; ^{+102\%}_{-39\%}$	$4.8 \cdot 10^1 \; ^{+100\%}_{-38\%}$
$V_0 V'_T \to \gamma W^+$	vp{0} vm{T} > a w+	$1.6 \cdot 10^{-2} \; ^{+62\%}_{-31\%}$	$7.3 \cdot 10^{-1} \; ^{+56\%}_{-28\%}$	$9.2 \cdot 10^{-1} \; ^{+54\%}_{-27\%}$
$V_0 V'_0 \to \gamma W^+$	vp{0} vm{0} > a w+	$1.5 \cdot 10^{-4}$	$1.2 \cdot 10^{-3}$	$1.7 \cdot 10^{-3}$
$\sum V_{\lambda_A} V'_{\lambda_B} \to \gamma\gamma$	vp vm > a a	$2.1 \cdot 10^0 \; ^{+172\%}_{-54\%}$	$8.5 \cdot 10^0 \; ^{+152\%}_{-50\%}$	$1.1 \cdot 10^1 \; ^{+147\%}_{-48\%}$
$V_T V'_T \to \gamma\gamma$	vp{T} vm{T} > a a	$2.1 \cdot 10^0 \; ^{+172\%}_{-54\%}$	$8.5 \cdot 10^0 \; ^{+152\%}_{-50\%}$	$1.1 \cdot 10^1 \; ^{+147\%}_{-48\%}$
$V_0 V'_T \to \gamma\gamma$	vp{0} vm{T} > a a	$7.8 \cdot 10^{-4} \; ^{+70\%}_{-35\%}$	$3.4 \cdot 10^{-3} \; ^{+67\%}_{-34\%}$	$4.2 \cdot 10^{-3} \; ^{+67\%}_{-33\%}$
$V_0 V'_0 \to \gamma\gamma$	vp{0} vm{0} > a a	$5.8 \cdot 10^{-4}$	$4.7 \cdot 10^{-3}$	$6.8 \cdot 10^{-3}$

Table 6. Same as Table 4 but for VV production.

largely $V_T V'_T$ scattering. The $V_0 V'_T$ rate is an order of magnitude or two smaller, and the $V_0 V'_0$ rate is smaller by about one or two additional decades.

The precise polarization composition has a slight dependence on the underlying process: The production of ZW^+W^- categorically exhibits the largest cross section, with $\sigma(ZW^+W^-) \sim \mathcal{O}(10 - 100 \text{ fb})$ for $\sqrt{s} \sim 5 - 30$ TeV. Over this same range, the $V_0 V'_T$ component is about $\mathcal{O}(1 - 10 \text{ fb})$, and the $V_0 V'_0$ component is about $\mathcal{O}(0.01 \text{ fb})$. On the other hand, for $\gamma\gamma W^+$ production, which categorically exhibits the second smallest cross section with $\sigma(\gamma\gamma W^-) \sim \mathcal{O}(1 \text{ fb})$, the $V_0 V'_T$ component is about $\mathcal{O}(10^{-2} \text{ fb})$, and the $V_0 V'_0$ component is about $\mathcal{O}(10^{-5} - 10^{-4} \text{ fb})$. In other words, ZW^+W^- production is very roughly $\mathcal{O}(90\%)$ $V_T V'_T$ scattering while $\gamma\gamma W^+$ production is roughly $\mathcal{O}(99\%)$ $V_T V'_T$ scattering.

Other similarities between triboson and diboson production include the cross section hierarchy that one observes in $V_T V'_T$ scattering largely appears also in $V_0 V'_T$ scattering and $V_0 V'_0$ scattering. One exception is $\gamma\gamma W^+$ and $\gamma\gamma$ production in $V_0 V'_0$ scattering, where the ordering inverts. We attribute this to the opening of orbital angular momentum configurations in $2 \to 3$ scattering, which can spoil the cancellations described in Sec. 5.3. While it
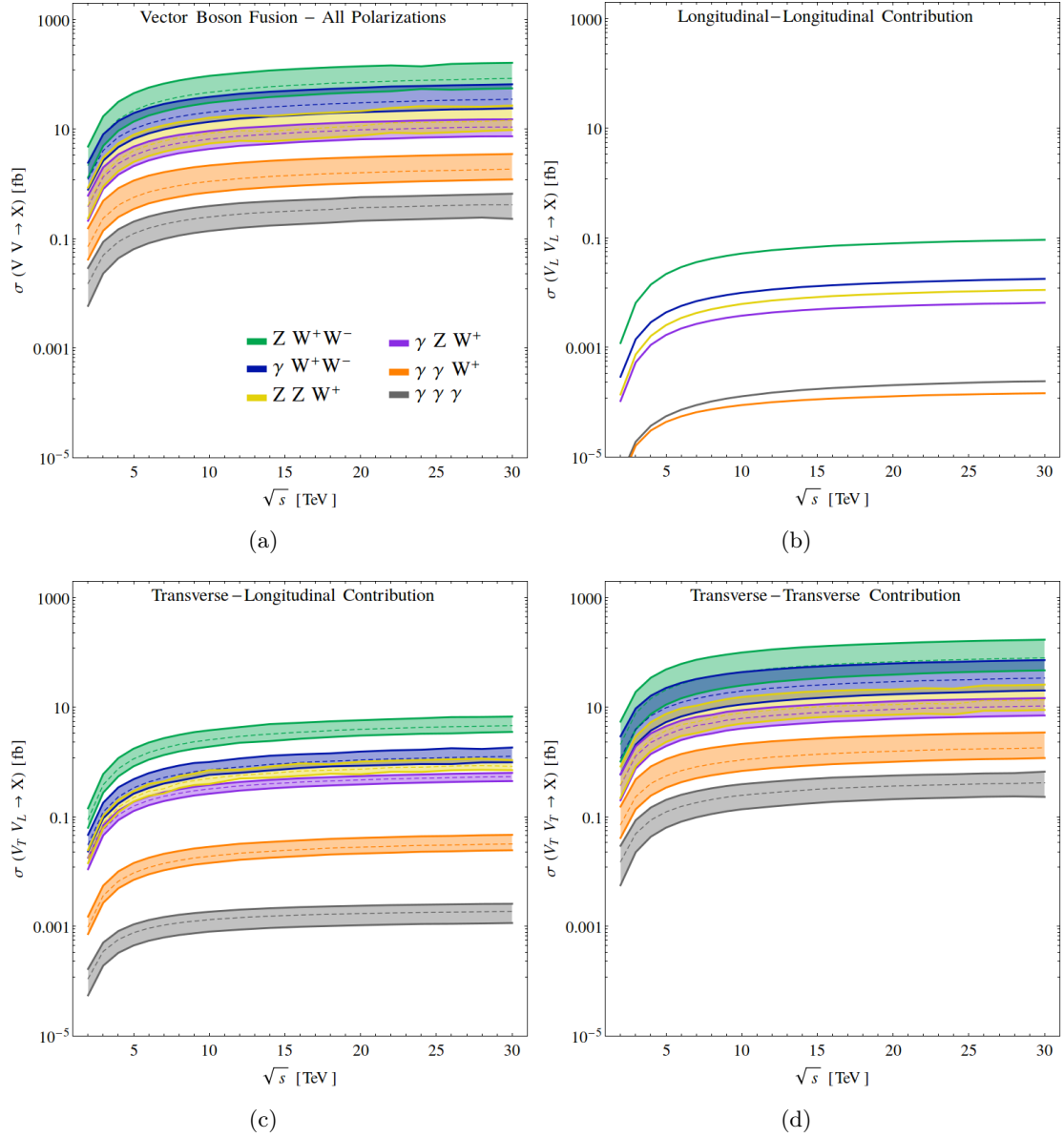
Figure 10. Same as Fig. 7 but for VVV production.

is beyond our immediate scope, one can, in principle, investigate the hierarchy of triboson processes by considering the relative important of specific partonic and helicity channels, e.g., $\gamma_- \gamma_+$ scattering or $Z_+ Z_0$ scattering. One can also further decompose the final-state triboson system into its helicity components, thereby allowing one to investigate the relative importance of high- and low-wave angular momentum configurations. Finally, due to the similarities between diboson and triboson production, we conjecture that comparable behavior will be observed for the production for four or more EW vector bosons.

We summarize these results for representative $\sqrt{s}$ in Table 7.

	`mg5amc` syntax	σ [fb]		
		$\sqrt{s} = 3$ TeV	$\sqrt{s} = 14$ TeV	$\sqrt{s} = 30$ TeV
$\sum V_{\lambda_A} V'_{\lambda_B} \to ZW^+W^-$	`vp vm > z w+ w-`	$2.1 \cdot 10^1\,^{+48\%}_{-38\%}$	$1.0 \cdot 10^2\,^{+41\%}_{-33\%}$	$1.4 \cdot 10^2\,^{+39\%}_{-32\%}$
$V_T V'_T \to ZW^+W^-$	`vp{T} vm{T} > z w+ w-`	$2.0 \cdot 10^1\,^{+49\%}_{-38\%}$	$9.9 \cdot 10^1\,^{+42\%}_{-34\%}$	$1.3 \cdot 10^2\,^{+40\%}_{-33\%}$
$V_0 V'_T \to ZW^+W^-$	`vp{0} vm{T} > z w+ w-`	$9.4 \cdot 10^{-1}\,^{+25\%}_{-25\%}$	$5.1 \cdot 10^0\,^{+21\%}_{-21\%}$	$6.8 \cdot 10^0\,^{+21\%}_{-21\%}$
$V_0 V'_0 \to ZW^+W^-$	`vp{0} vm{0} > z w+ w-`	$1.6 \cdot 10^{-2}$	$9.2 \cdot 10^{-2}$	$1.2 \cdot 10^{-1}$
$\sum V_{\lambda_A} V'_{\lambda_B} \to \gamma W^+W^-$	`vp vm > a w+ w-`	$1.2 \cdot 10^1\,^{+44\%}_{-35\%}$	$4.8 \cdot 10^1\,^{+40\%}_{-32\%}$	$6.3 \cdot 10^1\,^{+38\%}_{-31\%}$
$V_T V'_T \to \gamma W^+W^-$	`vp{T} vm{T} > a w+ w-`	$1.2 \cdot 10^1\,^{+45\%}_{-36\%}$	$4.6 \cdot 10^1\,^{+40\%}_{-33\%}$	$6.1 \cdot 10^1\,^{+40\%}_{-32\%}$
$V_0 V'_T \to \gamma W^+W^-$	`vp{0} vm{T} > a w+ w-`	$4.0 \cdot 10^{-1}\,^{+24\%}_{-24\%}$	$1.6 \cdot 10^0\,^{+21\%}_{-21\%}$	$2.1 \cdot 10^0\,^{+17\%}_{-17\%}$
$V_0 V'_0 \to \gamma W^+W^-$	`vp{0} vm{0} > a w+ w-`	$8.4 \cdot 10^{-3}$	$2.9 \cdot 10^{-2}$	$3.6 \cdot 10^{-2}$
$\sum V_{\lambda_A} V'_{\lambda_B} \to ZZZ$	`vp vm > z z z`	$3.5 \cdot 10^0\,^{+59\%}_{-45\%}$	$1.9 \cdot 10^1\,^{+49\%}_{-39\%}$	$2.5 \cdot 10^1\,^{+46\%}_{-37\%}$
$V_T V'_T \to ZZZ$	`vp{T} vm{T} > z z z`	$3.3 \cdot 10^0\,^{+61\%}_{-46\%}$	$1.7 \cdot 10^1\,^{+50\%}_{-40\%}$	$2.3 \cdot 10^1\,^{+48\%}_{-38\%}$
$V_0 V'_T \to ZZZ$	`vp{0} vm{T} > z z z`	$2.2 \cdot 10^{-1}\,^{+28\%}_{-28\%}$	$1.3 \cdot 10^0\,^{+23\%}_{-23\%}$	$1.7 \cdot 10^0\,^{+22\%}_{-22\%}$
$V_0 V'_0 \to ZZZ$	`vp{0} vm{0} > z z z`	$4.2 \cdot 10^{-3}$	$2.6 \cdot 10^{-2}$	$3.5 \cdot 10^{-2}$
$\sum V_{\lambda_A} V'_{\lambda_B} \to ZZW^+$	`vp vm > z z w+`	$3.5 \cdot 10^0\,^{+45\%}_{-37\%}$	$1.8 \cdot 10^1\,^{+38\%}_{-32\%}$	$2.3 \cdot 10^1\,^{+37\%}_{-31\%}$
$V_T V'_T \to ZZW^+$	`vp{T} vm{T} > z z w+`	$3.3 \cdot 10^0\,^{+46\%}_{-38\%}$	$1.7 \cdot 10^1\,^{+39\%}_{-33\%}$	$2.2 \cdot 10^1\,^{+38\%}_{-32\%}$
$V_0 V'_T \to ZZW^+$	`vp{0} vm{T} > z z w+`	$1.7 \cdot 10^{-1}\,^{+19\%}_{-19\%}$	$9.3 \cdot 10^{-1}\,^{+17\%}_{-17\%}$	$1.2 \cdot 10^1\,^{+16\%}_{-16\%}$
$V_0 V'_0 \to ZZW^+$	`vp{0} vm{0} > z z w+`	$1.9 \cdot 10^{-3}$	$1.1 \cdot 10^{-2}$	$1.5 \cdot 10^{-2}$
$\sum V_{\lambda_A} V'_{\lambda_B} \to \gamma ZW^+$	`vp vm > a z w+`	$3.5 \cdot 10^0\,^{+46\%}_{-38\%}$	$1.5 \cdot 10^1\,^{+39\%}_{-33\%}$	$1.9 \cdot 10^1\,^{+38\%}_{-32\%}$
$V_T V'_T \to \gamma ZW^+$	`vp{T} vm{T} > a z w+`	$3.4 \cdot 10^0\,^{+47\%}_{-38\%}$	$1.4 \cdot 10^1\,^{+40\%}_{-34\%}$	$1.8 \cdot 10^1\,^{+39\%}_{-33\%}$
$V_0 V'_T \to \gamma ZW^+$	`vp{0} vm{T} > a z w+`	$1.6 \cdot 10^{-1}\,^{+20\%}_{-20\%}$	$6.7 \cdot 10^{-1}\,^{+17\%}_{-17\%}$	$8.5 \cdot 10^{-1}\,^{+17\%}_{-17\%}$
$V_0 V'_0 \to \gamma ZW^+$	`vp{0} vm{0} > a z w+`	$2.0 \cdot 10^{-3}$	$8.3 \cdot 10^{-3}$	$1.0 \cdot 10^{-2}$
$\sum V_{\lambda_A} V'_{\lambda_B} \to \gamma\gamma W^+$	`vp vm > a a w+`	$6.9 \cdot 10^{-1}\,^{+48\%}_{-39\%}$	$2.6 \cdot 10^0\,^{+41\%}_{-34\%}$	$3.3 \cdot 10^0\,^{+40\%}_{-33\%}$
$V_T V'_T \to \gamma\gamma W^+$	`vp{T} vm{T} > a a w+`	$6.8 \cdot 10^{-1}\,^{+48\%}_{-40\%}$	$2.5 \cdot 10^0\,^{+41\%}_{-34\%}$	$3.2 \cdot 10^0\,^{+40\%}_{-34\%}$
$V_0 V'_T \to \gamma\gamma W^+$	`vp{0} vm{T} > a a w+`	$1.5 \cdot 10^{-2}\,^{+23\%}_{-23\%}$	$5.0 \cdot 10^{-2}\,^{+21\%}_{-21\%}$	$6.2 \cdot 10^{-2}\,^{+21\%}_{-21\%}$
$V_0 V'_0 \to \gamma\gamma W^+$	`vp{0} vm{0} > a a w+`	$1.8 \cdot 10^{-4}$	$4.6 \cdot 10^{-3}$	$5.3 \cdot 10^{-3}$

Table 7. Same as Table 4 but for VVV production.

6 Discussion, Outlook, and Conclusions

As a weakly coupled, non-Abelian gauge theory, the weak sector of the SM naturally exhibits similarities to the electromagnetic and strong sectors, e.g., coupling universality. However, as the weak sector is also spontaneously broken, scattering and decay rates involving weak bosons feature a power-law dependence on the scale ratio $(M_V^2/Q^2)^k$ or $(v^2/Q^2)^k$, with $k > 0$. In the absence of such contributions, i.e., when momentum-transfer scales are much larger than the EW scale, meaning that $\mathcal{O}(M_V^2/Q^2)$ terms are negligible, scattering and decay rates involving weak gauge bosons resemble the analogous expressions for massless gauge bosons in QED and pQCD. Importantly, this resemblance also holds for the factorization of weak-boson emission in the collinear and soft limits.

Precisely how factorization (and resummation) operates in the weak sector, and in particular how it differs from QED and pQCD, is no longer an academic intrigue as multi-TeV $\mu^+\mu^-$ colliders and 100 TeV pp colliders are being seriously discussed as eventual successors of the HL-LHC program [39, 40]. At these colliders, typical parton collisions readily satisfy known criteria for collinear factorization of weak bosons. Even at the $\sqrt{s} =$

13 TeV LHC, such hard-scattering scales have already been observed in measurements of VBF/S. Therefore, establishing a fuller picture of the colliders' physics potential requires a better understanding of how collinear and soft weak bosons behave in multi-TeV collisions.

Motivated by the fact that multi-TeV $\mu^+\mu^-$ colliders are effectively "high-luminosity weak boson colliders" [41], we have revisited the treatment of weak bosons as perturbative constituents of high-energy leptons, the so-called Effective W/Z Approximation [5, 6]. To conduct this investigation, we have implemented PDFs at LO for helicity-polarized γ, $W^\pm$, and Z bosons from $e^\pm$ and $\mu^\pm$ into the MC event generator `MadGraph5_aMC@NLO`.[‡] This allows for the fully differential simulation of scattering processes that are initiated by one or two initial-state EW bosons. Starting from a factorization theorem given in Eq. (2.2) (derived in App. A), we systematically explored the limitations of the EWA in Sec. 4. Novelties of our comparative investigation are the focus on: (i) universal and quasi-universal power-law corrections, (ii) universal and quasi-universal logarithmic corrections, (iii) phase space dependence, (iv) helicity polarization, and (v) many-body processes with VBF. Past studies were mostly restricted to $2 \to 1$ and $2 \to 2$ scattering processes, which possess special kinematics, at a single choice of factorization scale. We stress that some important issues, such as Z_T/γ_T mixing, were not investigated and are left to future work.

As documented in Sec. 4.2, a key conclusion is that the EWA is acutely sensitivity to power corrections of the form $(p_T^2/M_{VV'}^2)^k \sim (M_V^2/M_{VV'}^2)^k$ and $(M_V^2/M_{VV'}^2)^k$ for $k > 0$. These corrections originate in the derivation of weak boson PDFs and are related to the accuracy of collinear factorization and the Goldstone Equivalent Theorem. Our results suggest that using the EWA to describe VBF requires $M_{VV'} > \mathcal{O}(1 \text{ TeV})$, or $(M_V^2/M_{VV'}^2) \lesssim 0.01$. This is in addition to the typical assumptions needed to justify collinear factorization. When VBF systems carry larger invariant masses, we find that the difference between the full computation and the EWA are within factorization scale uncertainties. As documented in and around Eq. (4.7), these uncertainties can be very large and demonstrate a need for RG evolution in order to achieve precise results with weak boson PDFs. We caution that we restricted our attention to dynamic factorization scales that are proportional to $M_{VV'}$ for consistency across the *many* processes that we surveyed. As in pQCD, more "optimal" choices probably exist but are also (probably) process dependent and should be investigated thoroughly. Our implementation of EW boson PDFs in `mg5amc` can facilitate such studies.

Importantly, we show that the size of non-universal power corrections and the size of factorization scale ambiguities in multi-TeV $\mu^+\mu^-$ collisions are due to the largeness of the W and Z masses. At first, this may seem at odds with collinear factorization in pQCD, where above even a few GeV, PDFs can describe full matrix elements involving light quarks. However, using the operator product expansion, one can show that the phenomenon of "precocious scaling," i.e., the emergence of asymptotic freedom at moderate energies, is due to the smallness of *parton* masses [101–103]. Power corrections associated with quark masses m_q are of the form $(m_q^2/Q^2)^k$. For a scattering scale of $Q \sim 2 - 3$ GeV, these reach at most $\mathcal{O}(m_q^2/Q^2) \lesssim 10^{-5} - 10^{-2}$. Likewise, heavy quark PDFs become adequate and reliable tools for $\mathcal{O}(m_q^2/Q^2) \lesssim 0.01$ [8–11, 13]. Both are consistent with requiring that

---

[‡]These features will be released publicly in version 3.3.0, and available now from the `mg5amc` repository.

$(M_V^2/M_{VV'}^2) \lesssim 0.01$ for the EWA to adequately describe full matrix elements.

For $M_{VV'} \lesssim \mathcal{O}(1 \text{ TeV})$, we find contrasting behaviors between longitudinal and transverse weak boson PDFs: whereas longitudinal PDFs overestimate full scattering amplitudes, transverse PDFs underestimate them. As documented in Sec. 4.3, increasing the collider energy does not necessarily improve the accuracy of the EWA for $M_{VV'} \lesssim \mathcal{O}(1 \text{ TeV})$. Whereas the presence of soft logarithms slightly improve the accuracy of transverse PDFs when $\sqrt{s}$ is increased, these same logarithms worsen the accuracy for longitudinal PDFs. It is clear that a matching, subtraction, or re-weighting scheme akin to those already available for pQCD and QED is needed to correct EWA matrix elements in this region. To facilitate such developments, we also report the availability in `mg5amc` of both q^2- and p_T^2-dependent PDFs for transversely polarized EW bosons. As shown in Sec. 4.4, p_T^2-dependent PDFs consistently lead to larger cross sections in EWA, but converge to the q^2-dependent results when $\sqrt{s}$ increases. To further strengthen the parallels with pQCD, we give a proof-of-principle demonstration in Sec. 4.5 of matrix-element matching of W_T PDFs with the full matrix elements. Despite its formally large scale uncertainty band, the matched result shows significant independence on the matching scale. Broadly speaking, these capabilities provide a starting point for matching EWA matrix elements to EW parton showers and more sophisticated EW boson PDFs that involve RG evolution.

Given these considerations, we cataloged in Sec. 5 a litany of processes of the form

$$\sum_{V_\lambda \in \{\gamma_\lambda, Z_\lambda, W_\lambda^\pm\}} V_{\lambda_A} V'_{\lambda_B} \to \mathcal{F}, \tag{6.1}$$

where $\mathcal{F}$ contains up to $n_\mathcal{F} = 4$ states from the collection $\{H, t, \bar{t}, W^+, W^-, Z, \gamma\}$. In comparing polarized and polarization-summed cross sections, we find an intriguing interplay between helicity polarizations and hard scattering processes. For example: whereas multiboson and many-boson production is driven by the scattering of initial-states in the $(\lambda_A, \lambda_B) = (T, T)$ configuration, top quark and associated top quark production features a large $(0, T)$ and $(T, 0)$ component. In further contrast, multi-Higgs processes are dominated by (T, T) and $(0, 0)$ helicity configurations but receive only a marginal contribution from mixed configurations. It is worth noting that scale uncertainties at $\sqrt{s} = 3 - 30$ TeV reach about $\delta\sigma/\sigma \sim 20\% - 50\%$ for many processes, which is beyond expectations based on coupling order. As we remained inclusive with respect to the helicities of final-state particles, the processes we surveyed and their differential behavior can all be further investigated.

6.1 Recommendations for using W/Z PDFs in high-energy lepton collisions

Finally, while much about PDFs for polarized and unpolarized weak bosons remains to be investigated, we believe this work helps clarify quantitatively when the W and Z bosons can be treated as partonic constituents of high-energy leptons. To further this prerogative, we provide a set of recommendations on using weak boson PDFs in many-TeV scattering calculations. These guidelines draw heavily from the findings in Sec. 4, are supported by analytic derivations of weak boson PDFs in App. A, and are applied to our survey in Sec. 5. For details on the usage of EW boson PDFs in `mg5amc`, see App. B.1.

- To minimize power corrections of the form $\left(M_V^2 / M_{VV'}^2 \right)^k$, for $k > 0$, and which spoil the accuracy of the Goldstone Equivalence Theorem, require that $M_{VV'} > \mathcal{O}(1)$ TeV.

- To minimize power corrections of the form $\left(p_T^{l\,2} / M_{VV'}^2 \right)^k$, for $k > 0$, and which spoil the accuracy of collinear factorization, require that $\mu_f < \mathcal{O}(1)$ TeV.

- To minimize corrections associated with gauge bosons at $x \to 1$, restrict the use of p_T^2-evolved PDFs to $\sqrt{s} \gtrsim \mathcal{O}(10 \text{ TeV})$, or choose small μ_f for $\sqrt{s} \lesssim \mathcal{O}(10 \text{ TeV})$.

- While not discussed in detail, we find notably improved numerical stability for computations throughout Sec. 5 when evaluating matrix elements in the Feynman gauge.

Acknowledgments

A   Effective W, Z, γ Approximation

For completeness, we derive (polarized) W/Z PDFs as implemented in the MC event generator `mg5amc`. In making this work explicit, we avoid ambiguities in definitions of PDF that sometimes appear in the literature. Such differences are due to equally reasonable choices of, e.g., evolution variables, but can lead to sizable numerical differences at LO.

The construction proceeds in the following manner: after establishing notation and conventions in App. A.1, MEs for polarized collinear splitting functions are derived in App. A.2, with the corresponding phase space decomposition/factorization given in App. A.3. Transverse momentum dependent distribution functions are then derived in App. A.4, and finally the collinear PDFs are given in App. A.5. While the construction follow closely that of Ref. [74], the identification of a factorization scale μ_f as an ultraviolet regulator is more closely aligned with Ref. [7]. This make more manifest that the procedure for MEM (see Sec. 4.5 and (potential) RG evolution is similar to those procedures in pQCD.

A.1 Helicity Amplitude Notation and Conventions

To derive polarized, weak boson splitting functions and PDFs, we work at the helicity amplitude level, in the so-called `HELAS` basis [93]. We assume the spacetime metric signature $g_{\mu\nu} = \mathrm{diag}(+, -, -, -)$, and work in the unitary gauge at dimension $d = 4$.

Spin-$1/2$ Particles

For a fermion with mass $m = \sqrt{E^2 - |\vec{p}|^2}$, and a spin axis aligned with its momentum, its 4-momentum (p^μ) and transverse momentum (p_T) can be generically parameterized by

$$p^\mu = (E, p_x, p_y, p_z) = (E, |\vec{p}| \sin\theta \cos\phi, |\vec{p}| \sin\theta \sin\phi, |\vec{p}| \cos\theta), \tag{A.1}$$

$$p_T^2 = p_x^2 + p_y^2 = |\vec{p}|^2 \sin^2\theta. \tag{A.2}$$

The two-component helicity eigenstates with respect to the 3-momentum direction $\hat{p}$ are

$$\chi(\hat{p}, \lambda = +1) = \frac{1}{\sqrt{2|\vec{p}|(|\vec{p}| + p_z)}} \begin{pmatrix} |\vec{p}| + p_z \\ p_x + i p_y \end{pmatrix} = \begin{pmatrix} \cos\frac{\theta}{2} \\ e^{i\phi} \sin\frac{\theta}{2} \end{pmatrix}, \tag{A.3}$$

$$\chi(\hat{p}, \lambda = -1) = \frac{1}{\sqrt{2|\vec{p}|(|\vec{p}| + p_z)}} \begin{pmatrix} -p_x + i p_y \\ |\vec{p}| + p_z \end{pmatrix} = \begin{pmatrix} -e^{-i\phi} \sin\frac{\theta}{2} \\ \cos\frac{\theta}{2} \end{pmatrix}, \tag{A.4}$$

RH/LH helicities are normalized such that $\lambda = +1/-1$. Given this, the four-component helicity spinors for fermions (u) and antifermions (v) are:

$$u(p, \lambda) = \begin{pmatrix} \sqrt{E - \lambda|\vec{p}|}\, \chi(\hat{p}, \lambda) \\ \sqrt{E + \lambda|\vec{p}|}\, \chi(\hat{p}, \lambda) \end{pmatrix} \quad \text{and} \quad v(p, \lambda) = \begin{pmatrix} -\lambda\sqrt{E + \lambda|\vec{p}|}\chi(\hat{p}, -\lambda) \\ \lambda\sqrt{E - \lambda|\vec{p}|}\, \chi(\hat{p}, -\lambda) \end{pmatrix}. \tag{A.5}$$

In the high energy limit, where $(m/E) \ll 1$, the Dirac spinors simplify to

$$u(p, \lambda = +1) \approx \sqrt{2E} \begin{pmatrix} 0 \\ 0 \\ \cos\frac{\theta}{2} \\ e^{i\phi} \sin\frac{\theta}{2} \end{pmatrix}, \quad u(p, \lambda = -1) \approx \sqrt{2E} \begin{pmatrix} -e^{-i\phi} \sin\frac{\theta}{2} \\ \cos\frac{\theta}{2} \\ 0 \\ 0 \end{pmatrix}, \tag{A.6}$$

$$v(p, \lambda = +1) \approx \sqrt{2E} \begin{pmatrix} e^{-i\phi} \sin\frac{\theta}{2} \\ -\cos\frac{\theta}{2} \\ 0 \\ 0 \end{pmatrix}, \quad v(p, \lambda = -1) \approx -\sqrt{2E} \begin{pmatrix} 0 \\ 0 \\ \cos\frac{\theta}{2} \\ e^{i\phi} \sin\frac{\theta}{2} \end{pmatrix}. \tag{A.7}$$

As such, the RH/LH chiral projection operators $P_{R/L}$ are respectively,

$$P_R = \frac{1}{2}(1 + \gamma^5) = \begin{pmatrix} 0 & 0 & 0 & 0 \\ 0 & 0 & 0 & 0 \\ 0 & 0 & 1 & 0 \\ 0 & 0 & 0 & 1 \end{pmatrix} \quad \text{and} \quad P_L = \frac{1}{2}(1 - \gamma^5) = \begin{pmatrix} 1 & 0 & 0 & 0 \\ 0 & 1 & 0 & 0 \\ 0 & 0 & 0 & 0 \\ 0 & 0 & 0 & 0 \end{pmatrix}. \tag{A.8}$$

Immediately one sees that the projection operators satisfy the identities

$$1 = P_R + P_L \quad \text{and} \quad \gamma^5 = P_R - P_L. \tag{A.9}$$

Massive Spin-1 Particles

For a vector boson with mass $M_V = \sqrt{E_V^2 - |\vec{q}|^2}$ and a spin axis aligned with its momentum, its 4-momentum (q^μ) and transverse momentum (q_T) can be parameterized by

$$q^\mu = (E_V, q_x, q_y, q_z) = (E_V, |\vec{q}| \sin \bar\theta \cos \bar\phi, |\vec{q}| \sin \bar\theta \sin \bar\phi, |\vec{q}| \cos \bar\theta), \tag{A.10}$$

$$q_T^2 = q_x^2 + q_y^2 = |\vec{q}|^2 \sin^2 \bar\theta. \tag{A.11}$$

In the Cartesian representation, its polarization vectors are given by

$$\varepsilon^\mu(q, x) = \frac{1}{|\vec{q}| q_T}(0, q_x q_z, q_y q_z, -q_T^2) = (0, \cos \bar\theta \cos \bar\phi, \; \cos \bar\theta \sin \bar\phi, \; -\sin \bar\theta), \tag{A.12}$$

$$\varepsilon^\mu(q, y) = \frac{1}{q_T}(0, -q_y, q_x, 0) = (0, -\sin \bar\phi, \; \cos \bar\phi, 0), \tag{A.13}$$

$$\varepsilon^\mu(q, z) = \frac{E_V}{M_V |\vec{q}|}\left(\frac{|\vec{q}|^2}{E}, q_x, q_y, q_z\right) = \gamma(\beta, \; \sin \bar\theta \cos \bar\phi, \; \sin \bar\theta \sin \bar\phi, \; \cos \bar\theta). \tag{A.14}$$

In the last line we used the Lorentz factor $\gamma = E_V/M_V$ and the relationship $|\vec{q}| = \beta E_V$. In this representation, the above polarization vectors satisfy the orthogonality relationships:

$$q_\mu \varepsilon^\mu(q, \lambda) = 0 \quad \text{and} \quad \varepsilon^\mu(q, \lambda)\varepsilon_\mu(q, \lambda') = -\delta_{\lambda, \lambda'} \quad \text{for} \quad \lambda = x, y, z. \tag{A.15}$$

Using the above, we can build the polarization vectors in the polar representation. For the RH ($\lambda = +1$), LH ($\lambda = -1$), and longitudinal ($\lambda = 0$) polarizations, these are given by

$$\varepsilon^\mu(q, \lambda = \pm 1) = \frac{1}{\sqrt{2}}\left(-\lambda \varepsilon^\mu(q, x) - i\varepsilon^\mu(q, y)\right) \tag{A.16}$$

$$= \frac{1}{\sqrt{2}}\left(0, -\lambda \cos \bar\theta \cos \bar\phi + i \sin \bar\phi, -\lambda \cos \bar\theta \sin \bar\phi - i \cos \bar\phi, \lambda \sin \bar\theta\right), \tag{A.17}$$

$$\varepsilon^\mu(q, \lambda = 0) = \varepsilon^\mu(q, z). \tag{A.18}$$

For $\lambda = \pm 1$, the orthogonality relationships are modified such that

$$q_\mu \varepsilon^\mu(q, \lambda) = 0, \quad \varepsilon^\mu(q, \lambda)\varepsilon_\mu(q, \lambda') = \delta_{\lambda, -\lambda'} \quad \text{and} \quad \varepsilon^\mu(q, \lambda)\varepsilon_\mu^*(q, \lambda') = -\delta_{\lambda, \lambda'}. \tag{A.19}$$

In the EVA it is useful [5] to rewrite the $\lambda = 0$ vector in the following exact form:

$$\varepsilon^\mu(q, \lambda = 0) = \frac{q^\mu}{M_V} + \tilde\varepsilon^\mu(q), \quad \text{where} \tag{A.20}$$

$$\tilde\varepsilon^\mu(q) \equiv \frac{M_V}{E_V + |\vec{q}|}\left(-1, \frac{q_x}{|\vec{q}|}, \frac{q_y}{|\vec{q}|}, \frac{q_z}{|\vec{q}|}\right) \tag{A.21}$$

$$= \frac{M_V}{E_V + |\vec{q}|}\left(-1, \sin \bar\theta \cos \bar\phi, \sin \bar\theta \sin \bar\phi, \cos \bar\theta\right). \tag{A.22}$$

Explicit computation shows that the auxiliary vector $\tilde\varepsilon$ obeys the following inner products:

$$q_\mu \tilde\varepsilon^\mu(q) = -M_V, \quad \tilde\varepsilon^\mu(q)\tilde\varepsilon_\mu(q) = 0, \quad \tilde\varepsilon^\mu(q)\tilde\varepsilon_\mu^*(q) = 0, \tag{A.23}$$

$$\tilde\varepsilon^\mu(q)\varepsilon_\mu(q, \lambda = \pm 1) = 0, \quad \tilde\varepsilon^\mu(q)\varepsilon_\mu^*(q, \lambda = \pm 1) = 0. \tag{A.24}$$
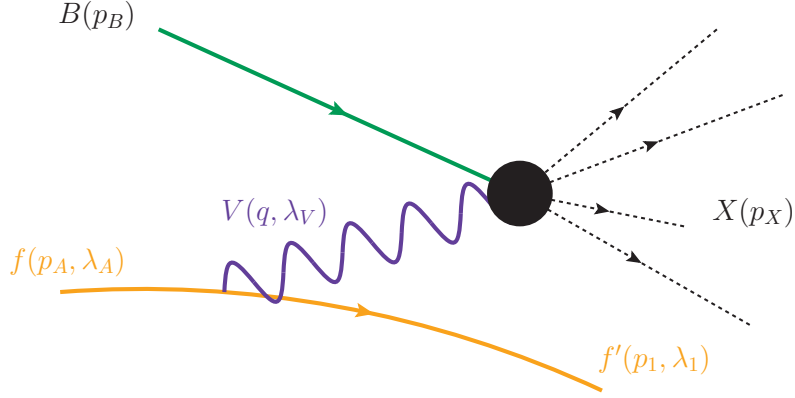
Figure 11. Diagrammatic representation of $f(p_A, \lambda_A) \to V(q, \lambda_V) f'(p_1, \lambda_1)$ splitting.

The purpose of this decomposition is two-fold: The first is to make manifest that the Goldstone contribution, i.e., the term that scales as $\varepsilon^\mu(\lambda = 0) \sim q^\mu/M_V$, vanishes when contracted with external parton currents via the Dirac equation. Ultimately, this is due to $\text{SU}(2)_L$ current conservation of massless leptons, meaning that massless leptons do not participate in helicity-inverting couplings of longitudinally weak boson. The second purpose is to make manifest that the non-vanishing part of $\varepsilon^\mu(\lambda = 0)$ is formally a quasi-universal, beyond-twist-two term that scales as $\varepsilon^0 \sim M_V/E$. Massless vector bosons have identical transverse polarization vectors but do not possess a longitudinal polarization vector.

A.2 Polarized Collinear Splitting Functions for Massive Vector Bosons

Setup and On-shell Decomposition

To build collinear splitting functions for weak bosons from high-energy leptons, we consider the deeply inelastic scattering (DIS) process shown in Fig, 11, given by

$$f(p_A, \lambda_A) + B(p_B) \xrightarrow{V(q,\lambda_V) + B(p_B) \to X(p_X)} f'(p_1, \lambda_1) + X(p_X). \qquad (A.25)$$

The process above describes $f(p_A) \to f'(p_1) + V(q)$ splitting with external fermions f, f', and an internal weak boson V with mass M_V. Throughout this section, we remain agnostic to the composition of B. In App. A.5, we will extend our result and present a factorization theorem involving a PDF for each beam. As we are only working at LO in the EW theory, we automatically work in the Single Boson Exchange Approximation. However, throughout this analysis, we neglect the contribution from interfering, Compton-like diagrams. Such contributions are sub-leading [7] in a Libby-Sterman sense [104, 105].

For the process in Eq. (A.25), the associated ME is given by

$$\mathcal{M}_{\text{EW−DIS}} = J^\mu(f_{\lambda_A} \to f'_{\lambda_1}) \; \cdot \; \Delta^V_{\mu\nu}(q = p_A - p_1) \; \cdot \; \mathcal{M}^\nu(V^*_{\lambda_V} B \to X). \qquad (A.26)$$

Here $\mathcal{M}^\nu(V^*_{\lambda_V} B \to X)$ describes the $V^*_{\lambda_V} B \to X$ hard scattering process that occurs at the scale $Q = \sqrt{(q + p_B)^2} \sim E_V \gg M_V \sim \sqrt{|q^2|}$. The propagator for V in the unitary gauge is denoted by $\Delta^V_{\mu\nu}$. Particle helicities are denoted by λ. For a $V - f - f'$ chiral interaction

with LH (RH) coupling g_L^f (g_R^f) and a universal strength $\tilde{g}$, the $f_{\lambda_A} \to f'_{\lambda_1} V^*_{\lambda_V}$ fermion current can be written generically as (see Table 1 in Sec. 2.2 for explicit expressions)

$$J^\mu(f_{\lambda_A} \to f'_{\lambda_1}) = \left[\overline{u}(p_1, \lambda_1)(-i\tilde{g})\gamma^\mu \left(g_L^f P_L + g_R^f P_R \right) u(p_A, \lambda_A) \right]. \quad (A.27)$$

An important caveat to this expression is that it assumes we are working solely within the confines of the SM's $\mathrm{SU}(2)_L$ gauge group (or some similarly broken gauge theory). It does not account for the fact that quarks and leptons in the SM both reside in the $\mathrm{SU}(3)_c \otimes \mathrm{SU}(2)_L$ product group. While working in this larger structure has trivial implications for EW splitting functions themselves, it does impact d.o.f. counting and cancellations at the level of cross sections. More precisely, for the $f_{\lambda_A} \to f'_{\lambda_1} V^*_{\lambda_V}$ color-singlet splitting process, the $V - f - f'$ vertex is modified by a Kronecker δ-function that ensures color conservation. In equation (A.27), this causes the modification

$$\mathrm{SU}(2)_L \to \mathrm{SU}(3)_c \otimes \mathrm{SU}(2)_L \quad : \quad (-i\tilde{g}) \to (-i\tilde{g})\delta_{JI}, \quad (A.28)$$

where the indices I and J denote the colors of f and f', respectively, and run over $I, J = 1, \ldots, N_c = 3$. For quarks, $\delta_{II} = N_c$, whereas $I, J = 1$ and $\delta_{II} = 1$ for leptons.

Working in the limit were $V^*_{\lambda_V}$ is nearly on-shell, the propagator's numerator can be decomposed into a sum over the outer product of polarization states with helicity λ_V,

$$\Delta^V_{\mu\nu}(q) = \frac{(-i)\left(g_{\mu\nu} - q_\mu q_\nu / M_V^2\right)}{(q^2 - M_V^2)} \approx \frac{i \sum_{\lambda_V \in \{0, \pm\}} \varepsilon^*_\mu(q, \lambda_V)\varepsilon_\nu(q, \lambda_V)}{(q^2 - M_V^2)}. \quad (A.29)$$

The idea here is that if V, which possesses an invariant lifetime $\tau_V = \hbar/\Gamma_V$, is on-shell and if the hard scattering scale is sufficiently large such that $Q \gg \Gamma_V$, then V is so long-lived that it can be well approximated as an asymptotic state. V's helicity λ_V remains unchanged during propagation: one would expect that helicity-inverting contributions scale as some positive power of $(M_V^2/Q^2) \ll 1$ [5]. Moreover, only physical polarizations of V contribute as unphysical / auxiliary polarizations contribute proportionally to $(q^2 - M_V^2)$ and therefore vanish under the on-shell condition. As a result, the Lorentz structure of the propagator $\Delta^V_{\mu\nu}(q)$ reduces to a *coherent* sum over physical polarizations λ_V. This to say, a summation over λ_V at the squared ME level.

In terms of current algebra, this decomposition is equivalent to writing the ME as

$$-i\mathcal{M}_{\mathrm{EW-DIS}} = \langle Xf'|fB \rangle = \langle X|\langle f'| \left(\frac{i}{q^2 - M_V^2} \sum_\lambda |V_\lambda\rangle\langle V_\lambda| \right) |f\rangle|B\rangle \quad (A.30)$$

$$\approx \frac{i}{q^2 - M_V^2} \sum_\lambda \langle X|V_\lambda B\rangle \, \langle V_\lambda f'|f\rangle, \quad (A.31)$$

which translates to a squared ME of

$$|\mathcal{M}_{\mathrm{EW-DIS}}|^2 \approx \frac{1}{(q^2 - M_V^2)^2} \sum_{\lambda, \lambda'} \langle f|V_{\lambda'}f'\rangle\langle V_\lambda f'|f\rangle \, \langle V_{\lambda'}B|X\rangle\langle X|V_\lambda B\rangle. \quad (A.32)$$

Naïvely, this suggests a double summation over the helicities of V. However, when one is totally inclusive over the final-state X, then by unitarity $\mathbb{1} = \sum_X |X\rangle\langle X|$. This implies

that the squared ME is only non-vanishing when the polarization of V in $f \to f'V_\lambda$ is the same as the polarization for V in $V_{\lambda'}B \to X$. Other $\langle V_\lambda | V_{\lambda'} \rangle$ combinations are orthogonal:

$$\sum_X \langle V_{\lambda'} B | X \rangle \langle X | V_\lambda B \rangle = \langle V_{\lambda'} B | V_\lambda B \rangle = 0, \quad \text{for } \lambda \neq \lambda'. \tag{A.33}$$

The unitarity of final-state X acts as an effective Kronecker δ-function $\delta_{\lambda\lambda'}$. This reduce the double summation over helicities into a single summation over helicities, resulting in

$$\sum_X |\mathcal{M}_{\text{EW--DIS}}|^2 \approx \frac{1}{(q^2 - M_V^2)^2} \sum_{X,\lambda} \langle f | V_\lambda f' \rangle \langle V_\lambda f' | f \rangle \langle V_\lambda B | X \rangle \langle X | V_\lambda B \rangle. \tag{A.34}$$

Returning to our derivation, after enjoining the outgoing (ε_μ^*) and incoming (ε_ν) polarizations vectors with the $f_{\lambda_A} \to f'_{\lambda_1} V_{\lambda_V}$ splitting amplitude and $V_{\lambda_V} B \to X$ scattering amplitude, respectively, one obtains the pair of MEs:

$$\mathcal{M}(f_{\lambda_A} \to f'_{\lambda_1} V_{\lambda_V}) = (-i\tilde{g}) \left[\overline{u}(p_1, \lambda_1) \, \not{\varepsilon}^*(q, \lambda_V) \left(g_L^f P_L + g_R^f P_R \right) u(p_A, \lambda_A) \right], \tag{A.35}$$

$$\mathcal{M}(V_{\lambda_V} B \to X) = \varepsilon_\nu(q, \lambda_V) \cdot \mathcal{M}^\nu(V_{\lambda_V} B \to X). \tag{A.36}$$

For fixed polarizations of *external* particles f, f', and V, the ME for the process in Eq. (A.25) can be factorized into two spin-correlated sub-amplitudes:

$$\mathcal{M}_{\text{EW--DIS}} \Big|_{q^2 \to M_V^2}^{\lambda_A, \lambda_1, \lambda_V} \approx \frac{i}{(q^2 - M_V^2)} \mathcal{M}(f_{\lambda_A} \to f'_{\lambda_1} V_{\lambda_V}) \, \mathcal{M}(V_{\lambda_V} B \to X). \tag{A.37}$$

Immediately, one can write at the squared ME level:

$$\sum_X |\mathcal{M}_{\text{EW--DIS}}|^2 \Big|_{q^2 \to M_V^2}^{\lambda_A, \lambda_1, \lambda_V} \approx \frac{1}{(q^2 - M_V^2)^2} |\mathcal{M}(f_{\lambda_A} \to f'_{\lambda_1} V_{\lambda_V})|^2 |\mathcal{M}(V_{\lambda_V} B \to X)|^2. \tag{A.38}$$

This indicates that if V goes on-shell and its mass is small compared to the scattering scale, then the probability density for $f_{\lambda_A} B \to f'_{\lambda_1} X$, when mediated by the space-like exchange of V_{λ_A}, can be approximated as the spin-correlated product of the $f_{\lambda_A} \to f'_{\lambda_1} V_{\lambda_V}$ and $V_{\lambda_V} B \to X$ probability densities.

Helicity-dependent Collinear Splitting Amplitudes

To enact the on-shell condition such that Eqs. (A.37) and (A.38) are valid, we work in the kinematic configuration where V and f' are emitted at shallow angles in $f \to f'V$ splitting, i.e., the collinear limit. Formally, this involves working to leading order in the parameter $\lambda \equiv p_T/E_A \ll 1$, where $\vec{p}_T$ is the transverse momentum 2-vector of $f'(p_1)$ and E_A is the energy of $f(p_A)$. Defining $z = E_V/E_A$ as the energy fraction carried by $V(q)$ in the hard

scattering frame, we can parameterize the momenta of the process in Eq. (A.25) by

$$p_A^\mu = E_A(1,0,0,+1), \qquad p_B^\mu = E_A(1,0,0,-1), \tag{A.39a}$$

$$p_1^\mu = \left((1-z)E_A, \ \vec{p}_T, \ (1-z)E_A - \frac{p_T^2}{2(1-z)E_A} \right), \tag{A.39b}$$

$$\equiv \left((1-z)E_A, \ |\vec{p}_1|\sin\theta_1\cos\phi_1, \ |\vec{p}_1|\sin\theta_1\sin\phi_1, \ (1-z)E_A - \frac{p_T^2}{2(1-z)E_A} \right), \tag{A.39c}$$

$$q^\mu = p_A^\mu - p_1^\mu = \left(zE_A, \ -\vec{p}_T, \ zE_A + \frac{p_T^2}{2(1-z)E_A} \right) \tag{A.39d}$$

$$\equiv \left(zE_A, \ |\vec{q}|\sin\theta_V\cos\phi_V, \ |\vec{q}|\sin\theta_V\sin\phi_V, \ |\vec{q}|\cos\theta_V \right). \tag{A.39e}$$

For the momenta above, $\sqrt{s_{AB}} = 2E_A$ is the scale at which the $f + B \to f' + X$ process occurs. While explicit computation of individual invariant masses leads to

$$p_A^2 = 0, \quad p_1^2 = -\frac{p_T^4}{4(1-z)^2 E_A^2}, \quad q^2 = -\frac{p_T^2}{(1-z)} - \frac{p_T^4}{4(1-z)^2 E_A^2}, \tag{A.40}$$

truncating wide-angle contributions at $\mathcal{O}(\lambda^2)$ results in the following approximations:

$$p_1^2 \approx 0, \quad q^2 \approx -\frac{p_T^2}{(1-z)}, \quad |\vec{p}_1|^2 \approx (1-z)^2 E_A^2, \quad \frac{\sin^2\theta_V}{\sin^2\theta_1} \approx \frac{(1-z)^2}{z^2}. \tag{A.41}$$

Intuitively, this indicates that external particles are massless or approximately massless (to $\mathcal{O}(\lambda^2)$). The internal V, on the other hand, carries a virtuality $\sqrt{-q^2} \sim p_T$ much smaller than the incoming energy E_A. As V is also nearly on-shell, the scaling relationship $M_V \sim \sqrt{-q^2} \ll E_A$ must consistently hold. Implicitly, we also work in the domain where the energy fraction z is far from its boundaries at $z = 0$ (the high-energy regime) and $z = 1$ (the threshold regime), which would otherwise necessitate resummation.

As f, f' are massless, the only non-zero $f_{\lambda_A}(p_A) \to f'_{\lambda_1}(p_1)$ currents (as defined in Eq. (A.27)) involving a vector emission are those that conserve helicity, namely

$$J^\mu(\lambda_A = L, \lambda_1 = L) = -i2\tilde{g}g_L^f\sqrt{E_A E_1}\left(\cos\frac{\theta_1}{2}, e^{i\phi_1}\sin\frac{\theta_1}{2}, -ie^{i\phi_1}\sin\frac{\theta_1}{2}, \cos\frac{\theta_1}{2} \right), \tag{A.42}$$

$$J^\mu(\lambda_A = R, \lambda_1 = R) = -i2\tilde{g}g_R^f\sqrt{E_A E_1}\left(\cos\frac{\theta_1}{2}, e^{-i\phi_1}\sin\frac{\theta_1}{2}, ie^{-i\phi_1}\sin\frac{\theta_1}{2}, \cos\frac{\theta_1}{2} \right). \tag{A.43}$$

Employing the transverse polarization vector in Eq. (A.17) for $V_{\lambda_V = \pm}$, we obtain as the helicity amplitude ($\mathcal{M}$) for the $f_L \to f'_L V_+$ splitting process

$$\mathcal{M}(f_L \to f'_L V_+) = J^\mu(\lambda_A = L, \lambda_1 = L) \cdot \varepsilon_\mu^*(\lambda_V = +) \tag{A.44}$$

$$= i2\sqrt{2}\tilde{g}g_L^f E_A\sqrt{1-z}\cos\left(\frac{\theta_1 + \theta_V}{2}\right)\sin\left(\frac{\theta_V}{2}\right) \tag{A.45}$$

$$= i\sqrt{2}\tilde{g}g_L^f E_A\sqrt{1-z}\,\theta_V + \mathcal{O}\left(\theta_1^2, \theta_V^2\right) \tag{A.46}$$

$$\approx i\sqrt{2}\tilde{g}g_L^f\frac{p_T\sqrt{1-z}}{z}. \tag{A.47}$$

Helicity Configuration	$\lvert\mathcal{M}(f_{\lambda_A} \to f'_{\lambda_1} V_{\lambda_V})\rvert^2$	Helicity Configuration	$\lvert\mathcal{M}(f_{\lambda_A} \to f'_{\lambda_1} V_{\lambda_V})\rvert^2$
$f_L \to f'_L V_+$	$2\left(\tilde{g}g_L^f\right)^2 \frac{p_T^2(1-z)}{z^2}$	$f_R \to f'_R V_+$	$\left(\frac{g_R^f}{g_L^f}\right)^2 \lvert\mathcal{M}(f_L \to f'_L V_-)\rvert^2$
$f_L \to f'_L V_-$	$2\left(\tilde{g}g_L^f\right)^2 \frac{p_T^2}{z^2(1-z)}$	$f_R \to f'_R V_-$	$\left(\frac{g_R^f}{g_L^f}\right)^2 \lvert\mathcal{M}(f_L \to f'_L V_+)\rvert^2$
$f_L \to f'_L V_0$	$4\left(\tilde{g}g_L^f\right)^2 \frac{M_V^2(1-z)}{z^2}$	$f_R \to f'_R V_0$	$\left(\frac{g_R^f}{g_L^f}\right)^2 \lvert\mathcal{M}(f_L \to f'_L V_0)\rvert^2$

Table 8. The squared helicity amplitude for the $f_{\lambda_A} \to f'_{\lambda_1} V_{\lambda_V}$ process in the collinear limit for each non-vanishing helicity permutation, and assuming the coupling normalization of table 1.

In the second line of the above, we evaluated the ME exactly. In the third, we expanded the angular dependence to lowest order in the opening angles, and in the final line substituted θ_V for p_T. Repeating the same steps for the $f_L \to f'_L V_-$ splitting process, we obtain

$$\mathcal{M}(f_L \to f'_L V_-) = J^\mu(\lambda_A = L, \lambda_1 = L) \cdot \varepsilon_\mu^*(\lambda_V = -) \tag{A.48}$$

$$= -i2\sqrt{2}\tilde{g}g_L^f E_A\sqrt{1-z}\sin\left(\frac{\theta_1 + \theta_V}{2}\right)\cos\left(\frac{\theta_V}{2}\right) \tag{A.49}$$

$$= -i\sqrt{2}\tilde{g}g_L^f E_A\sqrt{1-z}\,(\theta_1 + \theta_V) + \mathcal{O}\left(\theta_1^2,\ \theta_V^2\right) \tag{A.50}$$

$$\approx -i\sqrt{2}\tilde{g}g_L^f \frac{p_T}{z\sqrt{1-z}}. \tag{A.51}$$

Note that the Dirac equation for massless particles implies the following orthogonality:

$$J^\mu(p_A, p_1) \cdot (p_A - p_1)_\mu = (-i\tilde{g})\left[\overline{u}(p_1, \lambda_1)(\slashed{p}_A - \slashed{p}_1)\left(g_L^f P_L + g_R^f P_R\right)u(p_A, \lambda_A)\right] = 0. \tag{A.52}$$

Employing this and the longitudinal polarization vector in Eq. (A.20) for $V_{\lambda_V=0}$, then the helicity amplitude for the $f_L \to f'_L V_0$ splitting process is

$$\mathcal{M}(f_L \to f'_L V_0) = J^\mu(\lambda_A = L, \lambda_1 = L) \cdot \varepsilon_\mu^*(\lambda_V = 0) \tag{A.53}$$

$$= J^\mu(\lambda_A = L, \lambda_1 = L) \cdot \tilde{\varepsilon}_\mu^* \tag{A.54}$$

$$= i4\tilde{g}g_L^f \frac{M_V E_A\sqrt{1-z}}{zE_A + \sqrt{z^2 E_A^2 - M_W^2}}\cos\left(\frac{\theta_V}{2}\right)\cos\left(\frac{\theta_1 + \theta_V}{2}\right) \tag{A.55}$$

$$= i2\tilde{g}g_L^f \frac{M_V\sqrt{1-z}}{z} + \mathcal{O}\left(\theta_1^2,\ \theta_V^2,\ \theta_1\theta_V,\ \frac{M_V^2}{E_V^2}\right). \tag{A.56}$$

Importantly, the amplitudes for a transversely polarized V exhibit a dependence on p_T, whereas the dependence is on M_V for a longitudinally polarized V. As is well-documented throughout the literature, this distinction leads to qualitative differences in scale evolution for $\lambda_V = \pm$ and $\lambda_V = 0$ states. Moreover, as $\mathcal{M}(f_L \to f'_L V_0)$ vanishes as $(M_V/E_V) \to 0$, one can interpret the forward emission of V_0 bosons as a "beyond-twist-2" phenomenon.

By parity inversion, the helicity amplitudes for the RH $f_R \to f'_R$ currents are:

$$\mathcal{M}(f_R \to f'_R V_+) = J^\mu(\lambda_A = R, \lambda_1 = R) \cdot \varepsilon^*_\mu(\lambda_V = +) \tag{A.57}$$

$$= -\left(\frac{g^f_R}{g^f_L}\right) \mathcal{M}(f_L \to f'_L V_-), \tag{A.58}$$

$$\mathcal{M}(f_R \to f'_R V_-) = J^\mu(\lambda_A = R, \lambda_1 = R) \cdot \varepsilon^*_\mu(\lambda_V = -) \tag{A.59}$$

$$= -\left(\frac{g^f_R}{g^f_L}\right) \mathcal{M}(f_L \to f'_L V_+), \tag{A.60}$$

$$\mathcal{M}(f_R \to f'_R V_0) = J^\mu(\lambda_A = R, \lambda_1 = R) \cdot \varepsilon^*_\mu(\lambda_V = 0) \tag{A.61}$$

$$= \left(\frac{g^f_R}{g^f_L}\right) \mathcal{M}(f_L \to f'_L V_0). \tag{A.62}$$

Explicit computation reveals that the relative minus sign in the transverse polarization cases can be traced to the relative phase difference that defines the $\lambda_V = \pm$ polarization vectors. (This is also evident by the relative positive sign in the longitudinal case.) At the level of squared MEs ($|\mathcal{M}|^2$), the above splitting helicity amplitudes are summarized in Table 8. As discussed under Eq. (A.27), the helicity amplitudes here neglect the complication of f, f' carrying color. We now account for this by nothing that at the squared-ME level, the δ_{IJ} in Eq. (A.28) is squared and for quarks (leptons) sums to

$$\text{SU}(2)_L \to \text{SU}(3)_c \otimes \text{SU}(2)_L \quad : \quad \tilde{g}^2 \to \tilde{g}^2 \times \delta_{IJ}\delta_{IJ} = \tilde{g}^2 \times \delta_{II} = \tilde{g}^2 \times N_c \, (1). \tag{A.63}$$

A.3 Phase Space Decomposition

For the $f(p_A) + B(p_B) \to f'(p_1) + X(p_X)$ process, where X is some n_X-body final-state system, the phase space volume of the $(n_X + 1)$-body system can be organized to isolate the one-body phase space for f'. In doing so, we can factorize its contribution from the phase space for the hard $B + V \to X$ sub-process and remain inclusive with respect to the kinematics of f'. Noting the definition of V's momentum $q = p_A - p_1$, decomposing the momentum of X over its n_X constituents, and expressing the phase space volume for the $(p_A + p_B)$-system in terms of the $(q + p_B)$-system, we obtain

$$dPS_{n_X+1}(p_A + p_B; p_1, \{p_k\}) = (2\pi)^4 \delta\left(p_A + p_B - p_1 - \sum_{k=2}^{n_X+1} p_k\right) \prod_{k=1}^{n_X+1} \frac{d^3 p_k}{(2\pi)^3 2E_k} \tag{A.64}$$

$$= (2\pi)^4 \delta\left(q + p_B - \sum_{k=2}^{n_X+1} p_k\right) \frac{d^3 p_1}{(2\pi)^3 2E_1} \prod_{k=2}^{n_X+1} \frac{d^3 p_k}{(2\pi)^3 2E_k} \tag{A.65}$$

$$= dPS_{n_X}(q + p_B; \{p_k\}) \times \frac{d\phi_{f'} \, dz \, dq^2}{4(2\pi)^3}. \tag{A.66}$$

In the last line, we exploited the limits of Eq. (A.40), which allows the one-body phase space for f' to be written in terms of either evolution variable p_T^2 or q^2. Explicitly, this is

$$\frac{d^3 p_1}{(2\pi)^3 2E_1} = (-1)\frac{d\phi_{f'} \, dz \, dp_T^2}{4(2\pi)^3(1-z)} = \frac{d\phi_{f'} \, dz \, dq^2}{4(2\pi)^3}. \tag{A.67}$$

A.4 Transverse Momentum-Dependent Distribution Functions for EW Bosons

To build a set of splitting functions that can be used with both spin-averaged and helicity-polarized MEs, we follow the formalism of Ref. [70] and consider the $f + B \to f' + X$ scattering process when the external states f and f' are in definite helicity states λ_A and λ_1 but all other external states are unpolarized. (This implies that helicities are averaged and summed for B and X.) We work in the rest frame of X, which one can eventually identify as the hard-scattering frame. In the collinear approximation, this frame is related to the beam c.m. frame by a boost along the z axis. For massless objects, which travel on the light cone, such longitudinal boosts cannot change the helicity; for massive objects, e.g., EW bosons V, helicity inversions are suppressed by factors of (M_V/E_V), or some power thereof, and are strongly suppressed in our kinematic limit. Using the results of App. A.3, the semi-polarized, $2 \to n_X + 1$ cross section is subsequently given by

$$\sigma\left(f_{\lambda_A} + B \to f'_{\lambda_1} + X\right) = \int dPS_{n_X+1}(p_A + p_B; p_1, \{p_k\}) \left.\frac{d\sigma_{fB}}{dPS_{n_X+1}}\right|^{\{\lambda\}} \tag{A.68}$$

$$= \int \frac{d\phi_{f'}\, dz\, dq^2}{4(2\pi)^3} \times \int dPS_{n_X}(q + p_B; \{p_k\}) \left.\frac{d\sigma_{fB}}{dPS_{n_X+1}}\right|^{\{\lambda\}}, \tag{A.69}$$

where the color-averaged but helicity-dependent, totally differential cross section is

$$\left.\frac{d\sigma_{fB}}{dPS_{n_X+1}}\right|^{\{\lambda\}} = \frac{1}{2s_{AB}N_c^f N_c^B} \sum_{\text{dof}} \left|\mathcal{M}_{\text{EW}-\text{DIS}}\right|^2{}^{\{\lambda\}}. \tag{A.70}$$

In this expression, the summation runs over all extraneous dof, including color and possible multiplicities of X. N_c^f and N_c^B are the color factors for f and B. Working now in the collinear limit, fixing the polarization of V to be λ_V, and using the factorized squared ME of Eq. (A.38), we rewrite the helicity-dependent, differential cross section as

$$\left.\frac{d\sigma_{fB}}{dPS_{n_X+1}}\right|^{\{\lambda\}} = \frac{1}{2s_{AB}N_c^f N_c^B} \frac{1}{(q^2 - M_V^2)^2}$$

$$\times \sum_{\text{dof}} \left|\mathcal{M}(f_{\lambda_A} \to f'_{\lambda_1} V_{\lambda_V})\right|^2 \left|\mathcal{M}(V_{\lambda_V} B_{\lambda_B} \to X_{\{\lambda_X\}})\right|^2 \tag{A.71}$$

$$= \frac{z}{(q^2 - M_V^2)^2} \left|\mathcal{M}(f_{\lambda_A} \to f'_{\lambda_1} V_{\lambda_V})\right|^2$$

$$\times \frac{1}{2\lambda^{1/2}(Q^2, M_V^2, 0)N_c^V N_c^B} \sum_{\text{dof}} \left|\mathcal{M}(V_{\lambda_V} B_{\lambda_B} \to X_{\{\lambda_X\}})\right|^2 \tag{A.72}$$

In reaching the second line we exploited several observations. First is that in the kinematic limit in which we are working, the invariant masses of the (VB)-system (Q) and (fB)-system are related by $Q^2(1 - M_V^2/Q^2) = \lambda^{1/2}(Q^2, M_V^2, 0) \approx z s_{AB}$. Here, $\lambda(x, y, z)$ is the Källen function defined just below Eq. (2.5). Second is that $f \to f'V$ splitting is a color-singlet process and that we are free to introduce color-averaging factors of $1/N_c^V = 1$

for the $V + B \to X$ sub-process. This also implies that the squared amplitude for $f \to f'V$ passes through the summation after color indices have been counted (see Eq. (A.63)), i.e.,

$$\sum_{\text{color}} \left| \mathcal{M}(f_{\lambda_A} \to f'_{\lambda_1} V_{\lambda_V}) \right|^2 = N_c^f \left| \mathcal{M}(f_{\lambda_A} \to f'_{\lambda_1} V_{\lambda_V}) \right|^2. \tag{A.73}$$

Consequentially, we can consistently define the color-averaged but spin-dependent, total and differential cross sections for the (partonic) $V + B \to X$ sub-process at Q^2 to be

$$\hat{\sigma}\left(V_{\lambda_V} + B \to f'_{\lambda_1} + X\right) = \int dPS_{n_X}(q + p_B; \{p_k\}) \left. \frac{d\hat{\sigma}_{VB}}{dPS_{n_X}} \right|^{\{\lambda\}}, \quad \text{and} \tag{A.74}$$

$$\left. \frac{d\hat{\sigma}_{VB}}{dPS_{n_X}} \right|^{\{\lambda\}} = \frac{1}{2Q^2 N_c^V N_c^B} \sum_{\text{dof}} \left| \mathcal{M}(V_{\lambda_V} B \to X) \right|^2. \tag{A.75}$$

Immediately, this allows us to express the total cross section for the full $f + B \to f' + X$, i.e., Eq. (A.69), when mediated in the collinear limit by a sufficiently long-lived V_λ as

$$\sigma\left(f_{\lambda_A} + B \xrightarrow{V_{\lambda_V}} f'_{\lambda_1} + X\right) = \sum_{\lambda_V} \int \frac{d\phi_{f'} \, dz \, dq^2}{4(2\pi)^3} \frac{z}{(q^2 - M_V^2)^2} \left| \mathcal{M}(f_{\lambda_A} \to f'_{\lambda_1} V_{\lambda_V}) \right|^2$$
$$\times \hat{\sigma}\left(V_{\lambda_V} + B \to f'_{\lambda_1} + X\right) \tag{A.76}$$

$$\equiv \sum_{\lambda_V} \int_{z_0}^1 dz \int_{-\mu_f^2}^0 dq^2 \, \mathcal{F}_{V_{\lambda_V}/f_{\lambda_A}}(z, q^2) \times \hat{\sigma}\left(V_{\lambda_V} + B \to f'_{\lambda_1} + X\right), \tag{A.77}$$

$$\equiv \sum_{\lambda_V} \int_{z_0}^1 dz \int_0^{\mu_f^2} dp_T^2 \, \mathcal{H}_{V_{\lambda_V}/f_{\lambda_A}}(z, p_T^2) \times \hat{\sigma}\left(V_{\lambda_V} + B \to f'_{\lambda_1} + X\right). \tag{A.78}$$

In Eqs. (A.77) and (A.78) we extracted all ME factors associated with the polarized $f_{\lambda_A} \to f'_{\lambda_1} V_{\lambda_V}$ splitting process and any dependence on the azimuth angle to define the polarized, virtuality-dependent parton density function (VD PDF)

$$\mathcal{F}_{V_{\lambda_V}/f_{\lambda_A}}(z, q^2) \equiv \int \frac{d\phi_{f'}}{4(2\pi)^3} \frac{z}{(q^2 - M_V^2)^2} \left| \mathcal{M}(f_{\lambda_A} \to f'_{\lambda_1} V_{\lambda_V}) \right|^2, \tag{A.79}$$

and analogously the polarized, transverse momentum-dependent PDF (TMD PDF)

$$\mathcal{H}_{V_{\lambda_V}/f_{\lambda_A}}(z, p_T^2) \equiv \int \frac{d\phi_{f'}}{4(2\pi)^3} \frac{z(1-z)}{(p_T^2 + (1-z)M_V^2)^2} \left| \mathcal{M}(f_{\lambda_A} \to f'_{\lambda_1} V_{\lambda_V}) \right|^2. \tag{A.80}$$

Noting that V must carry a minimum amount of energy $V + B \to X$ sub-process to kinematically proceed, the lower boundary of the energy fraction integral is simply

$$z_0 = \min(z) = \min\left(Q^2\right)/s_{AB} = \left(\sum_{k=2}^{n_X+1} m_k\right)^2 / s_{AB} > \frac{M_V^2}{s_{AB}}. \tag{A.81}$$

Importantly, in Eqs. (A.77) and (A.78), the positive-definite cutoff scale $\mu_f > M_V$ was introduced by hand to regulate the ultraviolet limit of the virtuality and transverse momentum integrals. Intuitively, $\mu_f^2 \ll Q^2$ denotes the phase space boundary (cutoff) for

which $|q^2|, p_T^2 < \mu_f^2$ correspond to kinematics that justify a collinear expansion of ME; in the same way, $|q^2| \sim p_T^2 > \mu_f^2$ correspond to wide-angle kinematics. As discussed in Sec. 6, stipulating that $\mu_f \ll Q^2$ appears naïvely at odds with common use of quark and gluon PDFs in pQCD. However, it must be stressed that in pQCD, PDFs are typically RG-evolved with the DGLAP evolution equations. This impacts the interpretation and scaling of μ_f.

A.5 Collinear Distribution Functions for EW Bosons

Taking the squared MEs for $f_{\lambda_A} \to f'_{\lambda_1} V_{\lambda_V}$ splitting in Table 8 and evaluating the azimuth integral, we report in Eqs. (2.6) and (2.7) respectively, the full expressions for the q^2 PDFs (f) and the p_T^2 PDFs (h) of polarized weak bosons from high-energy charged leptons in the collinear limit. These expressions allow us to express the total cross section for the full $f + B \to f' + X$, i.e., Eq. (A.69), when mediated in the collinear limit as

$$
\sigma \left(f_{\lambda_A} + B \to f'_{\lambda_1} + X \right)
$$
$$
= \sum_{\lambda_V} \int_{z_0}^1 dz \; f_{V_{\lambda_V}/f_{\lambda_A}}(z, \mu_f^2) \times \sigma \left(V_{\lambda_V} + B \to f'_{\lambda_1} + X \right)
$$
$$
\underbrace{+ \mathcal{O}\left(\frac{p_T^2}{Q^4} \right) + \mathcal{O}\left(\frac{M_V^2}{Q^4} \right) + \mathcal{O}\left(\frac{\alpha_W}{Q^2} \log \frac{\mu_f^2}{M_V^2} \right)}_{\text{Power and Logarithmic Corrections}}, \quad \text{(A.82)}
$$
$$
= \sum_{\lambda_V} \int_{z_0}^1 dz \; h_{V_{\lambda_V}/f_{\lambda_A}}(z, \mu_f^2) \times \sigma \left(V_{\lambda_V} + B \to f'_{\lambda_1} + X \right)
$$
$$
+ \mathcal{O}\left(\frac{p_T^2}{Q^4} \right) + \mathcal{O}\left(\frac{M_V^2}{Q^4} \right) + \mathcal{O}\left(\frac{\alpha_W}{Q^2} \log \frac{\mu_f^2}{M_V^2} \right). \quad \text{(A.83)}
$$

In these expressions, we have made explicit the power and logarithmic corrections that parameterize the uncertainty of collinear factorization of weak bosons in scattering computations. The first correction is associated with how collinear V_{λ_V} and f'_{λ_1} are to the beam axis (or f_{λ_A}) and originate from expanding the $f_{\lambda_A} \to V_{\lambda_V} f'_{\lambda_1}$ splitting amplitudes as seen in Eqs. (A.47), (A.51), and (A.56). The second correction is associated with the accuracy of the Goldstone Equivalent Theorem and originate from expanding the $f_{\lambda_A} \to V_0 f'_{\lambda_1}$ amplitude as seen exclusively in Eq. (A.56). The third correction is associated with the μ_f dependence introduced to regulate the evolution integrals in Eqs. (A.77) and (A.78).

For the high-energy process $\mu^+ \mu^- \to \mathcal{F} + X$, where the production of $\mathcal{F}$ is mediated by high-energy $V_{\lambda_A} V_{\lambda_B}$ scattering, and X is some arbitrary, inclusive final state, we are able

to extend the above results and write the factorization theorem

$$\sigma(\mu^+\mu^- \to \mathcal{F} + X) = f \otimes f \otimes \hat{\sigma} + \text{Power and Logarithmic Corrections} \tag{A.84}$$

$$
\begin{aligned}
= & \sum_{V_{\lambda_A}, V'_{\lambda_B}} \int_{\tau_0}^1 d\xi_1 \int_{\tau_0/\xi_1}^1 d\xi_2 \int dPS_n \\
\times & \ f_{V_{\lambda_A}/\mu^+}(\xi_1, \mu_f) f_{V'_{\lambda_B}/\mu^-}(\xi_2, \mu_f) \\
\times & \ \frac{d\hat{\sigma}(V_{\lambda_A} V'_{\lambda_B} \to \mathcal{F})}{dPS_n} \\
+ & \ \mathcal{O}\left(\frac{p_{T,l_k}^2}{M_{VV'}^4}\right) + \mathcal{O}\left(\frac{M_{V_k}^2}{M_{VV'}^4}\right) + \mathcal{O}\left(\frac{\alpha_W}{M_{VV'}^2} \log \frac{\mu_f^2}{M_{V_k}^2}\right). \tag{A.85}
\end{aligned}
$$

B How to use EVA in MadGraph5_aMC@NLO

The simulation of polarized and unpolarized EW PDFs in high-energy charged lepton collisions, i.e., EVA, is possible using a series of commands inside the `mg5amc` interface. Instruction on how to run/setup `MadGraph5_aMC@NLO` for various configurations involving unpolarized matrix elements can be found in Ref. [90]; for the setup of polarized matrix elements, see Ref. [70]. In this appendix, we describe how to setup a EVA computation in `mg5amc` and particularly focus the new options and syntax introduced for this mode.

As a concrete example, we consider the hard scattering process $W^+W^- \to hh$ in $\mu^+\mu^-$ collisions. A typical set of `mg5amc` commands to simulate a process like this is

```
set group_subprocesses False
generate w+ w- > h h
output DIRECTORY_OUTPUT
launch DIRECTORY_OUTPUT
```

The command "`set group_subprocesses False`" is currently mandatory and deactivates some internal optimization mechanisms that are not (yet) compatible with EW boson PDFs as implemented into `mg5amc`. The second command corresponds to the hard process, and operates at the level of initial-state weak bosons. (In this sense, EW bosons are treated as partons of $e^\pm$ and $\mu^\pm$.) Note that EVA is only implemented here at LO in perturbation theory, without Z_T/γ_T mixing, and without EW-DGLAP evolution. Such corrections have a nontrivial impact on numerical results [4, 25, 50, 75–78]. The "`output`" command defines the directory where the code containing MEs and phase space integration routines, i.e., `MadEvent` [92], are physically written on disk. The "`launch`" command activates an interface to configure, compile, and execute this code. As `mg5amc` works by numerically evaluating helicity amplitudes, the command above syntax is equivalent [70] to the syntax

```
set group_subprocesses False
generate     w+{+} w-{+} > h h
add process w+{+} w-{-} > h h
add process w+{+} w-{0} > h h
```

	run_card variable	Newly allowed values	Comments
PDF config. for beams 1 & 2	`pdlabel`	none	Deactivates PDF for beams 1 & 2
		eva	Activates EVA for beams 1 & 2
		iww	Activates Improved Weizsäcker-Williams γ PDF [106]
		mixed	Allows beams 1 & 2 to be configured differently
PDF config. for beam 1	`pdlabel1`	none	Deactivates PDF for beam 1
		eva	Activates EVA for beam 1
		iww	Activates IWW γ PDF for beam 1
PDF config. for beam 2	`pdlabel2`	same as `pdlabel1`	Analogous to `pdlabel1`
Fixed factorization scale for beam 1	`fixed_fac_scale1`	True	Set μ_f for beam 1 to be static
		False	Sets μ_f for beam 1 to be dynamic
			This option overrides global variable `fixed_fac_scale`
Fixed fact. scale for beam 2	`fixed_fac_scale2`	same as `fixed_fac_scale1`	Analogous to `fixed_fac_scale1`
PDF evolution variable	`ievo_eva`	0 (default)	Sets EVA PDF evolution variable to q^2 (**only for EVA**)
		1	Sets EVA PDF evolution variable to p_T^2 (**only for EVA**)
Treatment of external helicities	`nhel`	0	Summation over all helicities
		1	Importance sampling over helicities (**req. for EVA**)
New cut	dsqrt_shat	default:0	Min. invariant mass cut on the scattering process (in GeV)

Table 9. The list of the important and/or new parameters introduce into `mg5amc` to support PDFs for polarized EW gauge bosons (EVA) from high-energy leptons. See text for further details.

```
add process w+{-} w-{+} > h h
add process w+{-} w-{-} > h h
add process w+{-} w-{0} > h h
add process w+{0} w-{+} > h h
add process w+{0} w-{-} > h h
add process w+{0} w-{0} > h h
output DIRECTORY_OUTPUT
```

In both cases, the particle species $W_\lambda^\pm$ is paired with the polarized PDF $f_{W_\lambda^\pm/\mu^\pm}(\xi, \mu_f)$.

When the user interface is initiated, i.e., just after the "`launch`" command, the user is prompted with the ability to edit multiple configuration files. To run in EVA mode, a user will need to edit the file `DIRECTORY_OUTPUT/Cards/run_card.dat`. This file contains all configuration details related to the beam, factorization scales, phase space restrictions (cuts), etc. The list of the important and new parameters are summarized in Table 9, and are described below. It is important to stress that in our implementation of EVA, initial- and final-state W and Z bosons retain their masses in all helicity amplitudes; nowhere do we set $M_W, M_Z = 0$ GeV. As a consequence, other `mg5amc` modules, such as `MadSpin` [107, 108], can be employed in conjunction with EVA computations. This allows one to study, for example, the full process, $W_T^+ W_T^- \to h(\to c\bar{c})h(\to b\bar{b})$.

Investigating new physics remains possible through the interface [91] to *Universal FeynRules Object* (UFO) libraries [109]. We caution, however, that EW boson PDFs are hard-coded into files `ElectroweakFlux.f` and `ElectroweakFluxDriver.f` in the directory `LO/Source/PDF/`. This means that modifications to the $\ell - \ell - \gamma/Z$ and $\ell - \nu - W$ vertices introduced by a UFO will not propagate into the PDFs. We have designed and organized the calling of EW boson PDFs in `mg5amc` such that the W and Z boson masses as well as the EW couplings are automatically set to those values listed in the configuration file `DIRECTORY_OUTPUT/Cards/param_card.dat`. The values of the electron and muon masses

are not read from the `param_card.dat`. Instead, the values listed in Eq. (3.3) are hard-coded into the file `DIRECTORY_OUTPUT/Source/PDF/ElectroweakFlux.inc`.

In order to initiate a computation with the EVA, the most important parameter that must be set in the file `run_card.dat` is the PDF set. Choosing EW boson PDFs for both beams can be done via the "`pdlabel`" parameter, which now accepts three additional modes: "`eva`" for the EW boson PDFs described in Sec. 2; "`iww`" for the so-called Improved Weizsäcker-Williams (IWW) γ PDF of Ref. [106]; and "`mixed`" for enabling different PDF configurations for beams 1 and 2. A fourth option "`none`" deactivates PDFs for both beams. The γ PDF described in Sec. 2 is known historically as the Weizsäcker-Williams approximation [16, 17, 74], and is analogous to the gluon PDF in QCD at LO. Setting "`pdlabel=iww`" calls the γ PDF derived using the IWW approximation [106]; this PDF is sometimes mislabeled in the literature. Simply put, the IWW γ PDF augments the original Weizsäcker-Williams γ PDF by terms that correspond to operators in the operator product expansion with a twist larger than 2, i.e., are relatively suppressed by powers of (m_ℓ^2/Q^2). Just like for partons in hadron PDFs, the appropriate PDF and ME are paired automatically by the routines of `pdg2pdf.f` and `pdg2pdf_lhapdf6.f` in the directory `LO/Source/PDF/`. To make these options clearer, we have updated instructions within `run_card.dat` to read:

```
#**************************************************************************
# PDF CHOICE: this automatically fixes alpha_s and its evol.      *
# pdlabel: lhapdf=LHAPDF (installation needed) [1412.7420]        *
#          iww=Improved Weizsaecker-Williams Approx.[hep-ph/9310350] *
#          eva=Effective W/Z/A Approx.        [21yy.zzzzz]        *
#          none=No PDF, same as lhapdf with lppx=0               *
#**************************************************************************
```

As described in Sec. 2, it is possible to derive EW boson PDFs that are functions of either the virtuality carried by the incoming EW boson or the transverse momentum carried away by the outgoing lepton in $\ell \to V\ell'$ splittings. The two are related but can lead to numerical differences (see Sec. 4.4). In `mg5amc`, both have been implemented and can be selected using the `run_card.dat` parameter "`ievo_eva`." If this parameter is set to "`0`" (default), q^2-based PDFs will be called, otherwise p_T^2-based PDFs will be called.

For asymmetric process, it is also possible, for the first time in `mg5amc`, to employ a different PDF configuration for each beam. This development makes it possible to call both EW boson PDFs and QCD parton PDFs for processes such as $W^-\bar{b} \to \bar{t}$ in e^-p or μ^-p collisions. To enable this, a user must set "`pdlabel=mixed`" and configure two new `run_card.dat` parameters "`pdlabel1`" and "`pdlabel2`." These two parameters operate in the same manner as "`pdlabel`" but are limited to only one beam. We stress that it is up to the user to ensure that "`pdlabel1`" and "`pdlabel2`" align with the parameters "`lpp1`" and "`lpp2`," as well as align with the `1 2 > 3 4 ...` ordering of "`generate`" command above.

Presently, the EVA is only enabled for $e^\pm$ and $\mu^\pm$ beams; other capabilities are under development. Therefore, for the EVA to work in `mg5amc`, one must stipulate which types of beams are colliding. In `run_card.dat`, this is specified via the parameters "`lpp1`" for beam 1 "`lpp2`" for beam 2. The allowed values of these parameters retain the same

meaning as in previous versions of `mg5amc`. Explicitly, setting "`lppX=0`" corresponds to no PDF for beam `X`, where `X` is 1 or 2. Likewise, "`lppX=+1(-1)`" corresponds to a PDF for a proton (antiproton), and "`lppX=+2(-2)`" calls the Equivalent Photon Approximation[§] γ PDF of Ref. [111], which describes the elastic emission of a photon from a proton (antiproton). Setting "`lppX=+3(-3)`" means employing a PDF for an electron (positron) beam, and "`lppX=+4(-4)`" means a PDF for a muon (antimuon) beam. Presently, setting "`pdlabel=eva`" or "`pdlabelX=eva`" requires setting "`lppX=±3`" or "`lppX=±4`." (The same is true for setting "`pdlabel=iww`" or "`pdlabelX=iww`.") To make these options clearer, we have updated the relevant instructions within `run_card.dat` to now read:

```
#*************************************************************************
# Collider type and energy                                             *
# lpp: 0=No PDF, 1=proton, -1=antiproton, 2=elastic photon of proton,*
#               +/-3=PDF of electron/positron beam                     *
#               +/-4=PDF of muon/antimuon beam                         *
#*************************************************************************
```

It is possible to use the EVA in `mg5amc` with same-sign lepton beams, e.g., "`lpp1=+4`" and "`lpp2=+4`," as well as mixed-flavor lepton beams, e.g., "`lpp1=-3`" and "`lpp2=+4`." At this point, we reminder potential users that due to electric and weak isospin charge assignments, polarized weak boson PDFs are not charge symmetric, e.g., $f_{W_{-1}^-/\mu_L^-}(\xi,\mu) \neq f_{W_{-1}^+/\mu_L^+}(\xi,\mu)$. Likewise, the EW boson PDF implemented here are only LO accurate. This means that the W^+ content of ℓ^- is zero since such splittings first appear first at $\mathcal{O}(\alpha\alpha_W)$.

Presently, it is possible in `mg5amc` to polarize electron and muon beams in lepton-lepton and lepton-hadron collisions in the absence of lepton PDFs, i.e., "`lppX=0`" [90]. We have extended this capability and it is now also possible to polarize electron and muon beams when "`lppX=±3,±4`" and "`pdlabel=eva`" or "`pdlabelX=eva`." This is done via the `run_card.dat` parameters "`polbeam1`" and "`polbeam2`." A value of "`polbeamX=0`" (default) corresponds to an unpolarized beam, while "`-100`" and "`+100`" indicate, respectively, that 100% of beam `X` is polarized in the LH and RH helicity state.[¶] Note that the helicity polarization of an EW boson cannot be changed at run time via `run_card.dat`. It can only be specified when executing the "`generate`" command; see Ref. [70] for details.

To implement beam polarization with the EVA, we have augmented Eq. (2.8), which describes a polarized EW boson V_λ from an unpolarized muon by the expression

$$f_{V_\lambda/\mu^\pm}(\xi,\mu_f) = (\beta_L + \frac{1-\beta_L}{2}) \times f_{V_\lambda/\mu_L^\pm}(\xi,\mu_f) + \frac{(1-\beta_L)}{2} \times f_{V_\lambda/\mu_R^\pm}(\xi,\mu_f). \qquad (B.1)$$

Here, $-1 \leq \beta_L \leq 1$ is a parameter describing the degree of LH polarization of the parent beam. For $\beta_L = 0$, which corresponds to setting "`polbeamX=0`," one recovers Eq. (2.8).

[§]We report the correction of a long-standing labeling ambiguity of this PDF in the file `LO/Source/PDF/PhotonFlux.f`, which contains the implementation of this PDF. We also reiterate that this PDF describes a photon from a proton in the elastic limit [110] and therefore does not include DGLAP evolution. For inelastic emissions of photons from protons, set "`lppX=+1(-1)`" and use a proton PDF set with QED evolution.

[¶]We note for clarity that setting "`polbeamX=-70`" indicates that 70% of beam `X` is polarized in the LH state while the remaining 30% is unpolarized. This implies that 85% (15%) of beam `X` consists of leptons in their LH (RH) helicity state.

Likewise, setting $\beta_L = -1$ (1), and implies that the muon beam itself is purely in the LH (RH) helicity state corresponds to setting "`polbeamX=-100 (100)`."

The collinear factorization scale μ_f that enters into EW boson PDFs in the EVA can be either dynamical, i.e., determined on an event-by-event basis, or fixed. This is chosen in `run_card.dat` via the Boolean parameter "`fixed_fac_scale`." Setting this parameter to "`true (false)`" activates a fixed (dynamical) μ_f. Like "`pdlabel`," the dynamical/static scale scheme can be set separately for each beam using the two Boolean parameters "`fixed_fac_scale1`" and "`fixed_fac_scale2`." If a static μ_f is selected, then its value is set in units of GeV by the parameters "`dsqrt_q2fact1`" and "`dsqrt_q2fact2`." For dynamical choices of μ_f, a user can choose from predefined or user-defined scale schemes using the parameter "`dynamical_scale_choice`." For details on this, see Ref. [90]. It is possible to rescale μ_f by the scale factor "`scalefact`".[‖] Importantly, automated scale variation of EW boson PDFs is possible using the "`systematics`" feature and setting "`use_syst=True`." Users are reminded that W/Z boson PDFs are not defined for values of $\mu_f < M_{W/Z}$.

B.1 Example usage of EVA in `MadGraph5_aMC@NLO`

To reproduce the cross sections for the process $V_{\lambda_A} V_{\lambda_B} \to HH$ in Table 4, we use the following syntax to generate our (polarized) matrix elements and work environments:

```
set group_subprocesses false
set gauge Feynman
define vap = w+ z a
define vam = w- z a
define vxp = w+ z
define vxm = w- z

generate vap vam > h h
output  vxvx_hh

generate vap{T} vam{T} > h h
output  vtvt_hh

generate    vap{T} vxm{0} > h h
add process vxp{0} vam{T} > h h
output  vtv0_hh

generate vxp{0} vxm{0} > h h
output  v0v0_hh
```

Fiducial cross sections, scale uncertainties, and events at $\sqrt{s} = 3$ TeV can then be obtained in accordance to the setup in Sec. 5 through the following run time commands

---

[‖]This new release of `mg5amc` is the first to allow both "`scalefact`" to be set different from unity and simultaneously allow "`use_syst=True`." However, one should note that the deprecated implementation of scale computation (SysCalc [112]) is not compatible with either the EVA or the new "`scalefact`" capability.

Channel	$\sqrt{s}=10$ TeV			$\sqrt{s}=14$ TeV			$\sqrt{s}=30$ TeV		
	$\sigma^{\text{Ref.}}$ [fb]	σ^{EVA} [fb]	$\frac{\Delta\sigma}{\delta\sigma_{\text{Stat.}}}$	$\sigma^{\text{Ref.}}$ [fb]	σ^{EVA} [fb]	$\frac{\Delta\sigma}{\delta\sigma_{\text{Stat.}}}$	$\sigma^{\text{Ref.}}$ [fb]	σ^{EVA} [fb]	$\frac{\Delta\sigma}{\delta\sigma_{\text{Stat.}}}$
Unpolarized	17.23	17.21	-0.8	21.17	21.15	-0.6	30.71	30.68	-0.7
$W_0^+ W_0^-$	7.702	7.694	-0.6	9.244	9.235	-0.6	12.85	12.84	-0.7
$W_0^\pm W_T^\mp$	7.713	7.704	-0.7	9.595	9.582	-0.8	14.18	14.17	-0.6
$W_T^+ W_T^-$	1.811	1.810	-0.3	2.329	2.327	-0.6	3.682	3.682	-0.1

Table 10. For the process $W_{\lambda_A}^+ W_{\lambda_B}^- \to t\bar{t}$ in multi-TeV $\mu^+\mu^-$ collisions, EWA-level cross sections [fb] as reported by Ref. [25] ($\sigma^{\text{Ref.}}$), the cross section computed with `mg5amc` (σ^{EVA}), and the statistical pull ($\Delta\sigma/\delta\sigma_{\text{Stat.}}$), for (top row) unpolarized W^+W^-, (second row) $W_0^+W_0^-$, (third row) $W_0^\pm W_T^\mp$, and (bottom row) $W_T^+W_T^-$ scattering, at $\sqrt{s}=10$ TeV (left), 14 TeV (center), and 30 TeV (right). The `mg5amc` statistical uncertainty corresponds to 400k events, or $\delta\sigma_{\text{Stat.}} \approx \pm 0.16\%$.

```
launch vxvx_hh
set width all 0
set lpp1 -4
set lpp2  4
set pdlabel eva
set fixed_fac_scale false
set dynamical_scale_choice 4 # muf = scalefact * dsqrt(shat)
set scalefact 0.5
set ievo_eva 0 # (0=q^2 or 1=pT^2)
set ebeam 1500
set no_parton_cut
set nevents 1k
set dsqrt_shat 1000
set pt_min_pdg  {25:50}
set eta_max_pdg {25:3}
set use_syst true
set nhel 1
```

The new and important commands for using the EVA in `mg5amc` are documented in App. B and summarized in Table 9.

B.2   Validation of EVA in `MadGraph5_aMC@NLO`

As one high-level check (of several) of our implementation of the EVA, we consider the process $W_{\lambda_A}^+ W_{\lambda_B}^- \to t\bar{t}$ in multi-TeV $\mu^+\mu^-$ collisions as studied in Ref. [25]. To simulate this process for various polarization configurations, we use the `mg5amc` syntax

```
set group_subprocesses false
set gauge Feynman

generate w+ w- > t t~ QED=2 QCD=0
output wxwx_tt_XLO
```

```
generate w+{0} w-{0} > t t~ QED=2 QCD=0
output w0w0_tt_XLO


generate w+{0} w-{T} > t t~ QED=2 QCD=0
add process w+{T} w-{0} > t t~ QED=2 QCD=0
output w0wT_tt_XLO


generate w+{T} w-{T} > t t~ QED=2 QCD=0
output wTwT_tt_XLO
```

The commands above correspond to (i) unpolarized W^+W^- scattering, (ii) $W_0^+W_0^-$ scattering, (iii) $W_0^\pm W_T^\mp$ scattering for $T = \pm 1$, and (iv) $W_T^+W_T^-$ scattering.

To avoid potential instabilities, the authors of Ref. [25] require final-state top quarks to have a nonzero polar angle in the hard-scattering frame. Specifically, they require

$$\cos\theta_{t\ (\bar{t})} = \frac{p_z^{t\ (\bar{t})}}{|\vec{p}\ ^{t\ (\bar{t})}|}| < \frac{m_t^2}{m_{t\bar{t}}^2}. \tag{B.2}$$

Here $p_z^{t(\bar{t})}$ is the z momentum of the (anti)top quark in the hard frame, $\vec{p}$ is its three-momentum in the same frame, and $m_{t\bar{t}}$ is the invariant mass of the $(t\bar{t})$-system. We implement this cut by adding the following lines in their appropriate locations to the `dummy_cuts` function in the auxiliary file `DIRECTORY_OUTPUT/SubProcesses/dummy_fct.f`:

```
integer ff
double precision mtop2,sHat,rat,cosTh
double precision SumDot
external SumDot


mtop2 = (173.0d0)**2
sHat = SumDot(p(0,1), p(0,2), 1d0)
rat = 1.d0 - mtop2 / sHat


do ff=nincoming+1,nexternal
c          =       pz / dsqrt(px2 + py2 + pz2)
    cosTh = p(3,ff) / dsqrt(p(1,ff)**2 + p(2,ff)**2 + p(3,ff)**2)
    if(cosTh.gt.rat) then
        dummy_cuts=.false.
        return
    endif
enddo
```

To steer phase space integration, we use the following commands at $\sqrt{s} = 10$ TeV:

```
launch wxwx_tt_XLO
```

```
set no_parton_cut
set ebeam 5000
set nevents 40k
set lpp1  -4 # setup beam1 as anti-muon
set lpp2   4 # setup beam2 as muon
set pdlabel eva
set fixed_fac_scale1 false
set fixed_fac_scale2 false
set dynamical_scale_choice 4 # muf = scalefact * dsqrt(shat)
set scalefact 0.5
set ievo_eva 0 # (0=q^2 or 1=pT^2)
set use_syst true
done
```

We make the necessary modification to this script for $\sqrt{s} = 14$ and 30 TeV.

  We report in Table 10 the EVA-level cross section [fb] as reported by Ref. [25], denoted by $\sigma^{\mathrm{Ref.}}$, the cross section computed with mg5amc, denoted by σ^{EVA}, and the statistical pull, defined by $\Delta\sigma/\delta\sigma_{Stat.} \equiv (\sigma^{\mathrm{EVA}} - \sigma^{\mathrm{Ref.}})/\delta\sigma_{Stat.}$, for $\sqrt{s} = 10, 14$, and 30 TeV, for (top row) unpolarized W^+W^- scattering, (second row) $W_0^+W_0^-$ scattering, (third row) $W_0^\pm W_T^\mp$ scattering for $T = \pm$, and (bottom row) $W_T^+W_T^-$ scattering. Due to MadEvent's multi-channel integration routines, a precise determination of our MC statistical uncertainty is complicated. Therefore, as a conservative estimate of our statistical uncertainty for 400k events, we take $\delta\sigma_{Stat.} = 1/\sqrt{4 \cdot 10^5} \approx 0.16\%$. While we find that differences are all negative, meaning σ^{EVA} is always larger, we report that differences only span $\Delta\sigma \approx -0.13\%$ to -0.01%. This translates to a statistical pull ranging from $\Delta\sigma/\delta\sigma_{\mathrm{Stat.}} \approx -0.1$ to -0.8.

References

[1] Z. Nagy and D. E. Soper, *Parton showers with quantum interference*, *JHEP* **09** (2007) 114, [0706.0017].

[2] F. Krauss, P. Petrov, M. Schoenherr and M. Spannowsky, *Measuring collinear W emissions inside jets*, *Phys. Rev. D* **89** (2014) 114006, [1403.4788].

[3] A. Hook and A. Katz, *Unbroken SU(2) at a 100 TeV collider*, *JHEP* **09** (2014) 175, [1407.2607].

[4] J. Chen, T. Han and B. Tweedie, *Electroweak Splitting Functions and High Energy Showering*, *JHEP* **11** (2017) 093, [1611.00788].

[5] S. Dawson, *The Effective W Approximation*, *Nucl. Phys. B* **249** (1985) 42–60.

[6] G. L. Kane, W. W. Repko and W. B. Rolnick, *The Effective W+-, Z0 Approximation for High-Energy Collisions*, *Phys. Lett. B* **148** (1984) 367–372.

[7] Z. Kunszt and D. E. Soper, *On the Validity of the Effective W Approximation*, *Nucl. Phys. B* **296** (1988) 253–289.

[8] E. Witten, *Heavy Quark Contributions to Deep Inelastic Scattering*, *Nucl. Phys. B* **104** (1976) 445–476.

[9] R. M. Barnett, H. E. Haber and D. E. Soper, *Ultraheavy Particle Production from Heavy Partons at Hadron Colliders*, *Nucl. Phys. B* **306** (1988) 697–745.

[10] F. I. Olness and W.-K. Tung, *When Is a Heavy Quark Not a Parton? Charged Higgs Production and Heavy Quark Mass Effects in the QCD Based Parton Model*, *Nucl. Phys. B* **308** (1988) 813.

[11] J. C. Collins, *Hard scattering factorization with heavy quarks: A General treatment*, *Phys. Rev. D* **58** (1998) 094002, [`hep-ph/9806259`].

[12] M. A. G. Aivazis, F. I. Olness and W.-K. Tung, *Leptoproduction of heavy quarks. 1. General formalism and kinematics of charged current and neutral current production processes*, *Phys. Rev. D* **50** (1994) 3085–3101, [`hep-ph/9312318`].

[13] M. A. G. Aivazis, J. C. Collins, F. I. Olness and W.-K. Tung, *Leptoproduction of heavy quarks. 2. A Unified QCD formulation of charged and neutral current processes from fixed target to collider energies*, *Phys. Rev. D* **50** (1994) 3102–3118, [`hep-ph/9312319`].

[14] S. Dawson, A. Ismail and I. Low, *Redux on "When is the top quark a parton?"*, *Phys. Rev. D* **90** (2014) 014005, [`1405.6211`].

[15] T. Han, J. Sayre and S. Westhoff, *Top-Quark Initiated Processes at High-Energy Hadron Colliders*, *JHEP* **04** (2015) 145, [`1411.2588`].

[16] C. F. von Weizsacker, *Radiation emitted in collisions of very fast electrons*, *Z. Phys.* **88** (1934) 612–625.

[17] E. J. Williams, *Nature of the high-energy particles of penetrating radiation and status of ionization and radiation formulae*, *Phys. Rev.* **45** (1934) 729–730.

[18] M. J. Duncan, G. L. Kane and W. W. Repko, *W W Physics at Future Colliders*, *Nucl. Phys. B* **272** (1986) 517–559.

[19] D. A. Dicus, K. J. Kallianpur and S. S. D. Willenbrock, *Higgs Boson Pair Production in the Effective W Approximation*, *Phys. Lett. B* **200** (1988) 187–192.

[20] G. Altarelli, B. Mele and F. Pitolli, *Heavy Higgs Production at Future Colliders*, *Nucl. Phys. B* **287** (1987) 205–224.

[21] J. Brehmer, J. Jaeckel and T. Plehn, *Polarized WW Scattering on the Higgs Pole*, *Phys. Rev. D* **90** (2014) 054023, [`1404.5951`].

[22] S. S. D. Willenbrock and D. A. Dicus, *Production of Heavy Quarks from W Gluon Fusion*, *Phys. Rev. D* **34** (1986) 155.

[23] S. Dawson and S. S. D. Willenbrock, *Heavy Fermion Production in the Effective W Approximation*, *Nucl. Phys. B* **284** (1987) 449.

[24] P. Ciafaloni and D. Comelli, *Electroweak evolution equations*, *JHEP* **11** (2005) 022, [`hep-ph/0505047`].

[25] T. Han, Y. Ma and K. Xie, *High energy leptonic collisions and electroweak parton distribution functions*, *Phys. Rev. D* **103** (2021) L031301, [`2007.14300`].

[26] S. Catani, F. Krauss, R. Kuhn and B. R. Webber, *QCD matrix elements + parton showers*, *JHEP* **11** (2001) 063, [`hep-ph/0109231`].

[27] F. Krauss, *Matrix elements and parton showers in hadronic interactions*, *JHEP* **08** (2002) 015, [`hep-ph/0205283`].

[28] M. L. Mangano, M. Moretti, F. Piccinini and M. Treccani, *Matching matrix elements and shower evolution for top-quark production in hadronic collisions*, *JHEP* **01** (2007) 013, [hep-ph/0611129].

[29] N. Lavesson and L. Lonnblad, *Extending CKKW-merging to One-Loop Matrix Elements*, *JHEP* **12** (2008) 070, [0811.2912].

[30] ATLAS collaboration, M. Aaboud et al., *Fiducial, total and differential cross-section measurements of t-channel single top-quark production in pp collisions at 8 TeV using data collected by the ATLAS detector*, *Eur. Phys. J. C* **77** (2017) 531, [1702.02859].

[31] CMS collaboration, A. M. Sirunyan et al., *Search for anomalous electroweak production of vector boson pairs in association with two jets in proton-proton collisions at 13 TeV*, *Phys. Lett. B* **798** (2019) 134985, [1905.07445].

[32] ATLAS collaboration, M. Aaboud et al., *Observation of electroweak production of a same-sign W boson pair in association with two jets in pp collisions at $\sqrt{s} = 13$ TeV with the ATLAS detector*, *Phys. Rev. Lett.* **123** (2019) 161801, [1906.03203].

[33] CMS collaboration, A. M. Sirunyan et al., *Measurement of differential cross sections and charge ratios for t-channel single top quark production in proton–proton collisions at $\sqrt{s} = 13$ TeV*, *Eur. Phys. J. C* **80** (2020) 370, [1907.08330].

[34] N. Arkani-Hamed, T. Han, M. Mangano and L.-T. Wang, *Physics opportunities of a 100 TeV proton–proton collider*, *Phys. Rept.* **652** (2016) 1–49, [1511.06495].

[35] M. Ahmad et al., *CEPC-SPPC Preliminary Conceptual Design Report. 1. Physics and Detector*, .

[36] FCC collaboration, A. Abada et al., *FCC Physics Opportunities: Future Circular Collider Conceptual Design Report Volume 1*, *Eur. Phys. J. C* **79** (2019) 474.

[37] FCC collaboration, A. Abada et al., *FCC-hh: The Hadron Collider: Future Circular Collider Conceptual Design Report Volume 3*, *Eur. Phys. J. ST* **228** (2019) 755–1107.

[38] FCC collaboration, A. Abada et al., *HE-LHC: The High-Energy Large Hadron Collider: Future Circular Collider Conceptual Design Report Volume 4*, *Eur. Phys. J. ST* **228** (2019) 1109–1382.

[39] R. K. Ellis et al., *Physics Briefing Book: Input for the European Strategy for Particle Physics Update 2020*, 1910.11775.

[40] EUROPEAN STRATEGY GROUP collaboration, *2020 Update of the European Strategy for Particle Physics*. CERN Council, Geneva, 2020, 10.17181/ESU2020.

[41] A. Costantini, F. De Lillo, F. Maltoni, L. Mantani, O. Mattelaer, R. Ruiz et al., *Vector boson fusion at multi-TeV muon colliders*, *JHEP* **09** (2020) 080, [2005.10289].

[42] M. Chiesa, F. Maltoni, L. Mantani, B. Mele, F. Piccinini and X. Zhao, *Measuring the quartic Higgs self-coupling at a multi-TeV muon collider*, *JHEP* **09** (2020) 098, [2003.13628].

[43] R. Capdevilla, D. Curtin, Y. Kahn and G. Krnjaic, *Discovering the physics of $(g - 2)_\mu$ at future muon colliders*, *Phys. Rev. D* **103** (2021) 075028, [2006.16277].

[44] K. Long, D. Lucchesi, M. Palmer, N. Pastrone, D. Schulte and V. Shiltsev, *Muon colliders to expand frontiers of particle physics*, *Nature Phys.* **17** (2021) 289–292, [2007.15684].

[45] T. Han, D. Liu, I. Low and X. Wang, *Electroweak couplings of the Higgs boson at a multi-TeV muon collider*, *Phys. Rev. D* **103** (2021) 013002, [2008.12204].

[46] T. Han, Z. Liu, L.-T. Wang and X. Wang, *WIMPs at High Energy Muon Colliders*, *Phys. Rev. D* **103** (2021) 075004, [2009.11287].

[47] D. Buttazzo, R. Franceschini and A. Wulzer, *Two Paths Towards Precision at a Very High Energy Lepton Collider*, *JHEP* **05** (2021) 219, [2012.11555].

[48] R. Capdevilla, D. Curtin, Y. Kahn and G. Krnjaic, *A No-Lose Theorem for Discovering the New Physics of $(g-2)_\mu$ at Muon Colliders*, 2101.10334.

[49] T. Han, S. Li, S. Su, W. Su and Y. Wu, *Heavy Higgs bosons in 2HDM at a muon collider*, *Phys. Rev. D* **104** (2021) 055029, [2102.08386].

[50] T. Han, Y. Ma and K. Xie, *Quark and Gluon Contents of a Lepton at High Energies*, 2103.09844.

[51] H. Al Ali et al., *The Muon Smasher's Guide*, 2103.14043.

[52] R. Franceschini and M. Greco, *Higgs and BSM Physics at the Future Muon Collider*, *Symmetry* **13** (2021) 851, [2104.05770].

[53] D. Buarque et al., *Vector Boson Scattering Processes: Status and Prospects*, 2106.01393.

[54] T. Yang, S. Qian, Z. Guan, C. Li, F. Meng, J. Xiao et al., *Longitudinally polarized ZZ scattering at the Muon Collider*, 2107.13581.

[55] T. Han, W. Kilian, N. Kreher, Y. Ma, J. Reuter, T. Striegl et al., *Precision Test of the Muon-Higgs Coupling at a High-energy Muon Collider*, 2108.05362.

[56] V. V. Sudakov, *Vertex parts at very high-energies in quantum electrodynamics*, Sov. Phys. JETP **3** (1956) 65–71.

[57] D. R. Yennie, S. C. Frautschi and H. Suura, *The infrared divergence phenomena and high-energy processes*, *Annals Phys.* **13** (1961) 379–452.

[58] J. C. Collins, D. E. Soper and G. F. Sterman, *Transverse Momentum Distribution in Drell-Yan Pair and W and Z Boson Production*, *Nucl. Phys. B* **250** (1985) 199–224.

[59] G. F. Sterman, *Summation of Large Corrections to Short Distance Hadronic Cross-Sections*, *Nucl. Phys. B* **281** (1987) 310–364.

[60] S. Catani and L. Trentadue, *Resummation of the QCD Perturbative Series for Hard Processes*, *Nucl. Phys. B* **327** (1989) 323–352.

[61] J. C. Collins, D. E. Soper and G. F. Sterman, *Factorization of Hard Processes in QCD*, *Adv. Ser. Direct. High Energy Phys.* **5** (1989) 1–91, [hep-ph/0409313].

[62] H. Contopanagos, E. Laenen and G. F. Sterman, *Sudakov factorization and resummation*, *Nucl. Phys. B* **484** (1997) 303–330, [hep-ph/9604313].

[63] J. Collins, *Foundations of perturbative QCD*, vol. 32. Cambridge University Press, 11, 2013.

[64] M. Ciafaloni, P. Ciafaloni and D. Comelli, *Electroweak Bloch-Nordsieck violation at the TeV scale: 'Strong' weak interactions?*, *Nucl. Phys. B* **589** (2000) 359–380, [hep-ph/0004071].

[65] G. Bell, J. H. Kuhn and J. Rittinger, *Electroweak Sudakov Logarithms and Real Gauge-Boson Radiation in the TeV Region*, *Eur. Phys. J. C* **70** (2010) 659–671, [1004.4117].

[66] A. Manohar, B. Shotwell, C. Bauer and S. Turczyk, *Non-cancellation of electroweak logarithms in high-energy scattering*, *Phys. Lett. B* **740** (2015) 179–187, [1409.1918].

[67] P. Borel, R. Franceschini, R. Rattazzi and A. Wulzer, *Probing the Scattering of Equivalent Electroweak Bosons*, *JHEP* **06** (2012) 122, [1202.1904].

[68] B. W. Lee, C. Quigg and H. B. Thacker, *The Strength of Weak Interactions at Very High-Energies and the Higgs Boson Mass*, *Phys. Rev. Lett.* **38** (1977) 883–885.

[69] B. W. Lee, C. Quigg and H. B. Thacker, *Weak Interactions at Very High-Energies: The Role of the Higgs Boson Mass*, *Phys. Rev. D* **16** (1977) 1519.

[70] D. Buarque Franzosi, O. Mattelaer, R. Ruiz and S. Shil, *Automated predictions from polarized matrix elements*, *JHEP* **04** (2020) 082, [1912.01725].

[71] J. Chen, *Electroweak Splitting Functions and High Energy Showering*, Ph.D. thesis, U. Pittsburgh (main), 2017.

[72] J. Chen, *On the Feynman Rules of Massive Gauge Theory in Physical Gauges*, 1902.06738.

[73] G. Cuomo, L. Vecchi and A. Wulzer, *Goldstone Equivalence and High Energy Electroweak Physics*, *SciPost Phys.* **8** (2020) 078, [1911.12366].

[74] M. E. Peskin and D. V. Schroeder, *An Introduction to quantum field theory*. Addison-Wesley, Reading, USA, 1995.

[75] C. W. Bauer, N. Ferland and B. R. Webber, *Standard Model Parton Distributions at Very High Energies*, *JHEP* **08** (2017) 036, [1703.08562].

[76] B. Fornal, A. V. Manohar and W. J. Waalewijn, *Electroweak Gauge Boson Parton Distribution Functions*, *JHEP* **05** (2018) 106, [1803.06347].

[77] C. W. Bauer, D. Provasoli and B. R. Webber, *Standard Model Fragmentation Functions at Very High Energies*, *JHEP* **11** (2018) 030, [1806.10157].

[78] C. W. Bauer and B. R. Webber, *Polarization Effects in Standard Model Parton Distributions at Very High Energies*, *JHEP* **03** (2019) 013, [1808.08831].

[79] V. D. Barger and R. J. N. Phillips, *COLLIDER PHYSICS*. 1987.

[80] I. Kuss, *Improved effective vector boson approximation for hadron hadron collisions*, *Phys. Rev. D* **55** (1997) 7165–7182, [hep-ph/9608453].

[81] W. Bernreuther and L. Chen, *Improved effective vector boson approximation revisited*, *Phys. Rev. D* **93** (2016) 053018, [1511.07706].

[82] I. Kuss and H. Spiesberger, *Luminosities for vector boson - vector boson scattering at high-energy colliders*, *Phys. Rev. D* **53** (1996) 6078–6093, [hep-ph/9507204].

[83] T. Becher, M. Neubert and G. Xu, *Dynamical Threshold Enhancement and Resummation in Drell-Yan Production*, *JHEP* **07** (2008) 030, [0710.0680].

[84] T. Becher, A. Broggio and A. Ferroglia, *Introduction to Soft-Collinear Effective Theory*, vol. 896. Springer, 2015, 10.1007/978-3-319-14848-9.

[85] M. Greco, T. Han and Z. Liu, *ISR effects for resonant Higgs production at future lepton colliders*, *Phys. Lett. B* **763** (2016) 409–415, [1607.03210].

[86] V. Bertone, M. Cacciari, S. Frixione and G. Stagnitto, *The partonic structure of the electron at the next-to-leading logarithmic accuracy in QED*, *JHEP* **03** (2020) 135, [1911.12040].

[87] S. Frixione, *Initial conditions for electron and photon structure and fragmentation functions*, *JHEP* **11** (2019) 158, [1909.03886].

[88] S. Frixione, O. Mattelaer, M. Zaro and X. Zhao, *Lepton collisions in MadGraph5_ aMC@NLO*, 2108.10261.

[89] T. Stelzer and W. F. Long, *Automatic generation of tree level helicity amplitudes*, *Comput. Phys. Commun.* **81** (1994) 357–371, [hep-ph/9401258].

[90] J. Alwall, R. Frederix, S. Frixione, V. Hirschi, F. Maltoni, O. Mattelaer et al., *The automated computation of tree-level and next-to-leading order differential cross sections, and their matching to parton shower simulations*, *JHEP* **07** (2014) 079, [1405.0301].

[91] P. de Aquino, W. Link, F. Maltoni, O. Mattelaer and T. Stelzer, *ALOHA: Automatic Libraries Of Helicity Amplitudes for Feynman Diagram Computations*, *Comput. Phys. Commun.* **183** (2012) 2254–2263, [1108.2041].

[92] F. Maltoni and T. Stelzer, *MadEvent: Automatic event generation with MadGraph*, *JHEP* **02** (2003) 027, [hep-ph/0208156].

[93] H. Murayama, I. Watanabe and K. Hagiwara, *HELAS: HELicity amplitude subroutines for Feynman diagram evaluations*, .

[94] F. Maltoni, K. Paul, T. Stelzer and S. Willenbrock, *Color Flow Decomposition of QCD Amplitudes*, *Phys. Rev. D* **67** (2003) 014026, [hep-ph/0209271].

[95] E. Conte, B. Fuks and G. Serret, *MadAnalysis 5, A User-Friendly Framework for Collider Phenomenology*, *Comput. Phys. Commun.* **184** (2013) 222–256, [1206.1599].

[96] E. Conte and B. Fuks, *Confronting new physics theories to LHC data with MADANALYSIS 5*, *Int. J. Mod. Phys. A* **33** (2018) 1830027, [1808.00480].

[97] PARTICLE DATA GROUP collaboration, P. A. Zyla et al., *Review of Particle Physics*, *PTEP* **2020** (2020) 083C01.

[98] C. W. Bauer and N. Ferland, *Resummation of electroweak Sudakov logarithms for real radiation*, *JHEP* **09** (2016) 025, [1601.07190].

[99] C. W. Bauer, N. Ferland and B. R. Webber, *Combining initial-state resummation with fixed-order calculations of electroweak corrections*, *JHEP* **04** (2018) 125, [1712.07147].

[100] A. V. Manohar and W. J. Waalewijn, *Electroweak Logarithms in Inclusive Cross Sections*, *JHEP* **08** (2018) 137, [1802.08687].

[101] H. Georgi and H. D. Politzer, *Freedom at Moderate Energies: Masses in Color Dynamics*, *Phys. Rev. D* **14** (1976) 1829.

[102] H. Georgi and H. D. Politzer, *Precocious Scaling, Rescaling and xi Scaling*, *Phys. Rev. Lett.* **36** (1976) 1281. [Erratum: Phys.Rev.Lett. 37, 68 (1976)].

[103] A. De Rujula, H. Georgi and H. D. Politzer, *Demythification of Electroproduction, Local Duality and Precocious Scaling*, *Annals Phys.* **103** (1977) 315.

[104] S. B. Libby and G. F. Sterman, *Jet and Lepton Pair Production in High-Energy Lepton-Hadron and Hadron-Hadron Scattering*, *Phys. Rev. D* **18** (1978) 3252.

[105] S. B. Libby and G. F. Sterman, *Mass Divergences in Two Particle Inelastic Scattering*, *Phys. Rev. D* **18** (1978) 4737.

[106] S. Frixione, M. L. Mangano, P. Nason and G. Ridolfi, *Improving the Weizsacker-Williams approximation in electron - proton collisions*, *Phys. Lett. B* **319** (1993) 339–345, [`hep-ph/9310350`].

[107] P. Artoisenet, R. Frederix, O. Mattelaer and R. Rietkerk, *Automatic spin-entangled decays of heavy resonances in Monte Carlo simulations*, *JHEP* **03** (2013) 015, [`1212.3460`].

[108] J. Alwall, C. Duhr, B. Fuks, O. Mattelaer, D. G. Öztürk and C.-H. Shen, *Computing decay rates for new physics theories with FeynRules and MadGraph 5_ aMC@NLO*, *Comput. Phys. Commun.* **197** (2015) 312–323, [`1402.1178`].

[109] C. Degrande, C. Duhr, B. Fuks, D. Grellscheid, O. Mattelaer and T. Reiter, *UFO - The Universal FeynRules Output*, *Comput. Phys. Commun.* **183** (2012) 1201–1214, [`1108.2040`].

[110] D. Alva, T. Han and R. Ruiz, *Heavy Majorana neutrinos from $W\gamma$ fusion at hadron colliders*, *JHEP* **02** (2015) 072, [`1411.7305`].

[111] V. M. Budnev, I. F. Ginzburg, G. V. Meledin and V. G. Serbo, *The Two photon particle production mechanism. Physical problems. Applications. Equivalent photon approximation*, *Phys. Rept.* **15** (1975) 181–281.

[112] A. Kalogeropoulos and J. Alwall, *The SysCalc code: A tool to derive theoretical systematic uncertainties*, `1801.08401`.